

# UC San Diego

## UC San Diego Electronic Theses and Dissertations

**Title**

Development and Analysis of Sub-Millimeter Electrocardiography

**Permalink**

<https://escholarship.org/uc/item/7qd7f525>

**Author**

Rogers, Nicholas Gregory

**Publication Date**

2019

Peer reviewed|Thesis/dissertation

UNIVERSITY OF CALIFORNIA SAN DIEGO

Development and Analysis of Sub-Millimeter Electrocorticography

A dissertation submitted in partial satisfaction of the  
requirements for the degree Doctor of Philosophy

in

Physics

by

Nicholas Rogers

Committee in charge:

Professor Vikash Gilja, Chair  
Professor Henry Abarbanel, Co-Chair  
Professor Shadi A. Dayeh  
Professor Anna Devor  
Professor Michael Fogler  
Professor Tatyana Sharpee

2019

Copyright  
Nicholas Rogers, 2019  
All rights reserved.

The Dissertation of Nicholas Rogers is approved and is acceptable in  
quality and form for publication on microfilm and electronically:

---

---

---

---

---

Co-Chair

---

Chair

University of California San Diego

2019



## TABLE OF CONTENTS

Signature Page .....	iii
Table of Contents .....	iv
List of Figures .....	vi
List of Tables .....	viii
Acknowledgements .....	ix
Vita .....	xi
Abstract of the Dissertation .....	xii
Chapter 1 Introduction .....	1
1.1 Background .....	1
1.2 Electrophysiology .....	2
1.3 Electrocorticography .....	5
1.4 PEDOT Microelectrode Arrays .....	6
Chapter 2 Recording System and Initial Testing .....	9
2.1 Introduction .....	9
2.2 System Design .....	11
2.2.1 Hardware .....	11
2.2.2 Software .....	12
2.2.3 Device Fabrication .....	13
2.3 Experiment .....	13
2.3.1 Pre-Operative Methods .....	13
2.3.2 Intra-Operative Methods .....	14
2.3.3 Electrophysiology .....	14
2.3.4 Analysis and Statistical Methods .....	16
2.4 Results .....	18
2.4.1 Initial Testing Results .....	18
2.4.2 Human Electrocorticography .....	19
2.5 Discussion .....	22
Chapter 3 Spatial Characterization of Surface Potentials at the Sub-Millimeter Scale .....	34
3.1 Introduction .....	34
3.2 Methods .....	38
3.2.1 Human Intra-Operative Recording .....	38
3.2.2 Mouse Acute Recording .....	39

3.2.3	Recording and Pre-processing .....	39
3.2.4	Distance-Averaged Correlation .....	40
3.2.5	Component Analysis and Modeling .....	40
3.2.6	Independent Component Analysis .....	44
3.2.7	Common Average Reference .....	47
3.3	Results .....	48
3.3.1	Distance-Averaged Correlation .....	48
3.3.2	Component Modeling .....	50
3.3.3	ICA Decomposition of the Recordings .....	51
3.3.4	Localized Response Modeling .....	57
3.4	Discussion .....	58
Chapter 4	Volume Conduction in Electrophysiology .....	64
4.1	The Brain as a Volume Conductor .....	64
4.1.1	Static Conductivity and Permittivity .....	64
4.1.2	Time/Frequency Dependence .....	65
4.2	Current Sources and their Potentials .....	68
4.2.1	New .....	68
4.2.2	Solutions near the Cortical Surface - ECoG Model .....	70
Chapter 5	Implications of Boundary Effects for ECoG Array Design .....	75
5.1	Introduction .....	75
5.2	Methods .....	77
5.2.1	Three-Layer Model .....	77
5.2.2	Experimental Procedure .....	79
5.2.3	Signal processing and Trial Selection .....	80
5.2.4	Model Predictions .....	82
5.3	Results .....	84
5.3.1	Model Predictions .....	84
5.3.2	Experimental Results .....	85
5.3.3	Implications for Electrocorticography .....	87
5.4	Discussion .....	91
5.4.1	Laminar Electrode Effects .....	91
5.4.2	ECoG Model .....	93
Chapter 6	Concluding Remarks .....	97
	Bibliography .....	99

## LIST OF FIGURES

Figure 2.1.	Component breakdown of system .....	24
Figure 2.2.	Ephys system connected and running using a modified version of the Intans compiled software .....	25
Figure 2.3.	Structural and morphological characterization of PEDOT:PSS electrophysiology device .....	26
Figure 2.4.	Illustration of operating room setup .....	27
Figure 2.5.	Intra-operative recording .....	28
Figure 2.6.	Anesthesia dependent power spectral density .....	29
Figure 2.7.	Beta and gamma responses .....	30
Figure 2.8.	Awake versus unconscious ECoG differences in clinical, PEDOT macro, and micro electrodes .....	31
Figure 2.9.	Methohexital (Brevital) induced differences in clinical, PEDOT macro, and micro electrodes .....	32
Figure 2.10.	Neural activity varies across distances as small as 400 $\mu\text{m}$ .....	33
Figure 3.1.	Correlation averaged equidistant electrode pairs (DAC) .....	49
Figure 3.2.	The effects of parameters of the Gaussian component modeling on the DAC curves .....	52
Figure 3.3.	ICA components and their associated weights mapped to the grid geometry .....	53
Figure 3.4.	Example ICA components plotted on the electrode grid .....	54
Figure 3.5.	Histograms of the R2 values of fitting ICA components to a circular Gaussian function .....	55
Figure 3.6.	Contributions to the drop in the DAC as a function of goodness-of-fit	56
Figure 3.7.	Multivariate normal (MVN) model parametrized by decaying exponentials .....	57
Figure 3.8.	Numerical comparison of Mahalanobis distance between grids ...	59

Figure 4.1.	Conductivity and permittivity of excised gray matter. Parameters from from Gabriel et al. (1996). . . . .	68
Figure 4.2.	Bode plot of the transfer function of the complex conductivity of gray matter. Parameters from from Gabriel et al. (1996). . . . .	70
Figure 5.1.	Experimental schematic and evoked responses . . . . .	81
Figure 5.2.	Model predictions of boundary on laminar electrode recordings . .	86
Figure 5.3.	Measured ratio of evoked responses between conditions . . . . .	87
Figure 5.4.	Sensitivity profiles of inserted electrode at depth 0.5 mm . . . . .	88
Figure 5.5.	Comparison of sensitivity profiles of an electrode at the surface . .	89
Figure 5.6.	Effects of separation of the electrode above the surface . . . . .	91
Figure 5.7.	Comparison of sensitivity of two array designs for chronic implan- tation . . . . .	94

## LIST OF TABLES

Table 2.1.	List of variously used common ephys systems, (Siegle et al., 2015; Newman et al., 2013; Kinney et al., 2015) .....	12
Table 4.1.	Cole-Cole fit parameters from Gabriel et al. (1996) .....	67

## ACKNOWLEDGEMENTS

Chapter 2, in part, is a reprint of the material as it appears in A Clinic Compatible, Open Source Electrophysiology System in Engineering in Medicine and Biology Society (EMBC), 2016. Hermiz, John; Rogers, Nick; Kaestner, Erik; Ganji, Mehran; Cleary, Dan; Snider, Joseph; Barba, David; Dayeh, Shadi; Halgren, Eric; Gilja, Vikash. The dissertation author was a co-investigator and co-author of this paper.

Chapter 2, in part, is a reprint of the material as it appears in Development and Translation of PEDOT: PSS Microelectrodes for Intraoperative Monitoring in Advanced Functional Materials, 2017. Ganji, Mehran; Kaestner, Erik; Hermiz, John; Rogers, Nicholas; Tanaka, Atsunori; Cleary, Daniel; Lee, Sang Heon; Snider, Joseph; Halgren, Milan; Cosgrove, Garth Rees; Carter, Bob S.; Barba, David; Uguz, Ilke; Malliaras, George G.; Cash, Sydney S.; Gilja, Vikash; Halgren, Eric; Dayeh, Shadi A. The dissertation author was a co-investigator and co-author of this paper.

Chapter 3 is a reprint of the material as it appears in Correlation Structure in Micro-ECoG Recordings is Described by Spatially Coherent Components in PLoS Computational Biology, 2019. Rogers, Nicholas; Hermiz, John; Ganji, Mehran; Kaestner, Erik; Kılıç, Kılıncım ; Hossain, Lorraine; Thunemann, Martin; Cleary, Daniel R; Carter, Bob S; Barba, David; Devor, Anna; Halgren, Eric; Dayeh, Shadi A; Gilja, Vikash. The dissertation author was the primary investigator and author of this material.

Chapter 3, in part, is a reprint of the material as it appears in Sub-Millimeter ECoG Pitch In Human Enables Higher Fidelity Cognitive Neural State Estimation in NeuroImage, 2018. Hermiz, John; Rogers, Nicholas; Kaestner, Erik; Ganji, Mehran; Cleary, Daniel R; Carter, Bob S; Barba, David; Dayeh, Shadi A; Halgren, Eric; Gilja, Vikash. The dissertation author was a co-investigator and co-author of this paper.

Chapter 5, in full, is a reprint of the material as submitted in Theoretical and Experimental Analysis of the Impact of Brain Surface Boundary Conditions and Implica-

tions for Electrocorticography to Frontiers in Neuroscience in 2019. Rogers, Nicholas; Thunemann, Martin; Devor, Anna; Gilja, Vikash. The dissertation author was the primary investigator and author of this material.

## VITA

- 2012        B.S. in Mechanical Engineering, North Carolina State University
- 2012        B.S. in Physics, North Carolina State University
- 2019        Ph.D. in Physics, UC San Diego

## PUBLICATIONS

**Rogers, N.**, Thunemann, M., Devor, A., Gilja V., “Theoretical and experimental analysis of the impact of brain surface boundary conditions and implications for electrocorticography” in preparation.

**Rogers, N.**, Hermiz, J., Ganji, M., Kaestner, E., K., Kivilcim , Hossain, L., Thunemann, M., Cleary, D.R., Carter, B.S., Barba, D. and Devor, A., 2019. Correlation Structure in Micro-ECOG Recordings is Described by Spatially Coherent Components. PLoS computational biology, 15(2), p.e1006769.

Hermiz, J., **Rogers, N.**, Kaestner, E., Ganji, M., Cleary, D.R., Carter, B.S., Barba, D., Dayeh, S.A., Halgren, E. and Gilja, V., 2018. Sub-millimeter ECOG pitch in human enables higher fidelity cognitive neural state estimation. NeuroImage, 176, pp.454-464.

Ganji, M., Kaestner, E., Hermiz, J., **Rogers, N.**, Tanaka, A., Cleary, D., Lee, S.H., Snider, J., Halgren, M., Cosgrove, G.R. and Carter, B.S., 2018. Development and translation of PEDOT: PSS microelectrodes for intraoperative monitoring. Advanced Functional Materials, 28(12), p.1700232.

Lyu, H., Liu, X., **Rogers, N.**, Gilja, V. and Kuzum, D., 2016, August. Graphene neural interfaces for artifact free optogenetics. In 2016 38th Annual International Conference of the IEEE Engineering in Medicine and Biology Society (EMBC) (pp. 4204-4207). IEEE.

Hermiz, J., **Rogers, N.**, Kaestner, E., Ganji, M., Cleary, D., Snider, J., Barba, D., Dayeh, S., Halgren, E. and Gilja, V., 2016, August. A clinic compatible, open source electrophysiology system. In 2016 38th Annual International Conference of the IEEE Engineering in Medicine and Biology Society (EMBC) (pp. 4511-4514). IEEE.



## ABSTRACT OF THE DISSERTATION

Development and Analysis of Sub-Millimeter Electrocorticography

by

Nicholas Rogers

Doctor of Philosophy in Physics

University of California, San Diego, 2019

Professor Vikash Gilja, Chair  
Professor Henry Abarbanel, Co-Chair

The work summarized in this thesis focuses on the recording and analysis of data from micro-ECoG arrays implanted in vivo. The electrode arrays with diameters on the order of tens of microns and grid pitches on the order of hundreds of microns are recording from the surface of the brain at a novel scale. The research summarized in this work is aimed at the successful implantation and recording of these arrays and subsequent analysis of the properties of the electric potentials on the brain surface as measured at this considerably smaller than usual scale.

# Chapter 1

## Introduction

### 1.1 Background

Technologies that enable the recording or stimulation of brain activity have made interfacing with the brain a rapidly growing field of research and application development. Electrical recording has long been a staple of neuroscience, but electrodes and other recording methods have found clinical uses and, more recently, are the main tool in brain-computer interfaces (BCI). Electrical recording and stimulation is a natural choice for brain interfaces because brain activity is principally electrochemical, but other modalities have been developed that make use of the complex structure of the brain and interactions to either directly or indirectly sense or stimulate activity. Magnetic resonance imaging (MRI) uses nuclear magnetic resonance (NMR) to image the body and its variant functional MRI (fMRI) is able to record neural activity through detecting changes in blood flow and oxygenation that correlated with local (on the order of millimeters) changes in neural activity. On the opposite extreme is the use of genetically encoded calcium indicators (GECI), one of many optically based tools, that allow the activity of individual neurons to be detected by causing changes in fluorescence.

Each modality has benefits and drawbacks and the application generally drives the choice of technology. There are four categories that are sometimes used to summarize the

properties of an interfacing technology: spatial resolution, temporal resolution, level of invasiveness, and portability. We would like to always increase resolution and portability and decrease invasiveness, but in practice improving one area is at the cost of other ones. Ideally we could use non-invasive techniques, that don't require any medical procedure, but for the most part a non-invasive recording has much lower spatial and/or temporal resolution than its invasive counterpart or invasive recordings generally. The most common non-invasive recording modalities are electroencephalography (EEG), magnetoencephalography (MEG), and fMRI. Roughly, EEG and MEG have limited spatial resolution but high temporal resolution, and fMRI has limited temporal resolution (as a hemodynamic signal) but potentially high spatial resolution.

Invasive recordings, with their much higher resolution, offer the ability to record individual action potentials. Recordings of action potentials (also called units or spikes) have long been a mainstay of neuroscience research as they are a primary unit of neural computation, and this is where state-of-the-art optical techniques are making high quality simultaneous recording of, and precise stimulation of, many neurons possible. The drawback of most optical techniques, due to the fact the brain does not inherently produce strong optical signals, is that to create light-sensitive or light-emitting neurons substances must be injected into the brain tissue and/or the animal must be genetically modified. This has meant for human research involving invasive procedures electrical recording has remained the most common modality.

## **1.2 Electrophysiology**

Due to the assortment of different electrode types and where they are placed relative to the brain there are many different types of electrophysiological signals. Common types include EEG on the scalp, penetrating electrodes (in human often called stereo EEG or SEEG), or intracranial electrodes outside the brain tissue (electroencephalogra-

phy or ECoG). Essentially there are two "channels" that can be present in the electric potential: unit activity (action potentials) and field potentials (FP). Each type has further subdivisions depending on how they are recorded. For example units that can be individually identified are sometimes called single unit activity (SUA) while aggregate action potentials that are not separated is called multi-unit activity (MUA). Recording of SUA, and to a lesser extent, MUA requires the electrode to be small and located near spiking neurons, and therefore have only been consistently present when recorded with electrodes that penetrate into the brain.

The other portion of the electrophysiological signal, which has been termed the field potential (FP), is always present as evidenced by our ability even to record electrical activity through the scalp and skull (EEG). This is also where one of the common names for these signals comes from: local field potentials (LFP) were the term for the relatively slow fluctuations that are in the background of SUA that was being measured by penetrating microelectrodes. LFP was often ignored in these recordings in favor of SUA which could be used to measure activity of precisely located neurons that could even sometimes be identified by the shape of the units.

In contrast the LFP had, and generally continues to have, no definite physiological basis which is well understood with which to interpret the signal. Mechanism that generate FP are understood, but there are too many unknowns about the underlying activity for a given FP signal to be decomposed and explained. The sources are highly distributed and interconnected, confounding simple explanations of even features of FP let alone FP in general. This is a near constant difficulty in FP recording at all scales, from inside to brain to EEG. This is largely the case due to FP being anything but local, and is why sometimes more general terms like FP or extracellular FP are used for intracranial signals. In fact, it is customary to refer to and differentiate between FP signals based on the modality of electrophysiology used to record them, and the name of the modality

is often interchangeably used with the term for the signals themselves such as EEG or ECoG. The fundamental property that all have in common is that the potentials are the aggregate activity of thousands to millions, or even more, neurons that is all recorded by a single electrode by conduction of the potentials through the conductive tissues of and around the brain.

What differentiates the modalities and defines each one's signal characteristics is how much tissue the potentials must propagate through to reach the electrode. An electrode deep in cortex near several neurons will record those few relatively strongly and may even record units from them. Even more neurons within around 50 microns will have weaker signals and may have detectable MUA. If the electrode is moved just outside of the brain on the surface it may be too far from any individual neurons to selectively record them, and it will record from maybe hundreds or thousands of relatively close neurons that all contribute roughly equally with lesser contributions from deeper or more distant neurons. For an EEG electrode it is more appropriate to think of the signal originating from brain regions made up of millions of neurons rather than individual neurons.

Different types of electrophysiology exhibit the previously mentioned tradeoff; as the placement of the electrodes becomes more invasive the resolution increases. Temporal resolution of electrical recording is extremely high as the potential propagate effectively instantaneously compared to the time scales of neural activity, but the spatial resolution is defined by how large an area an electrode selectively records from. While any electrode can record very distant activity, the spatial specificity comes from the relative contribution of more distant neurons relative to the most strongly recorded neuron. Lack of specificity combined with attenuation of the potential as the distance of the electrode increases causes the degradation of spatial resolution as it takes increasingly larger populations of neurons to generate detectable signals and the precise origin of those signals becomes

more difficult to determine.

The spatial resolution is limited by volume conduction of the potentials to the electrode, but it can be improved by the use of arrays of electrodes. In addition to providing more simultaneous recordings, additional electrodes can improve spatial discrimination in a number of ways. Differences between electrodes can help separate local and nonlocal potentials, neighboring electrodes can localize with more precision, and an entire array can be incorporated using physical or physiological based analyses. Arrays are used in all types of electrophysiology: tetrodes are four closely spaced electrodes used to discriminate spiking activity, EEG is practically always recorded with many channels due to the relative ease of adding electrodes, and clinical ECoG arrays come in grids and strips with to improve localization accuracy and coverage.

Improvements in recording hardware and electrode fabrication technology allow for smaller, better, and more electrodes to be incorporated into arrays. The benefit for EEG can be somewhat improved localization, but volume conduction through the skull limits spatial resolution and even at hundred electrodes is past the point of diminishing returns. Invasive recordings on the other hand, have high enough spatial resolution that makes scaling more beneficial. For example, it would take a seemingly unlimited number of channels to tile the brain with penetrating electrodes, and even with the relatively large spacing of clinical electrodes of 1 cm it would take hundreds of electrodes to cover human cortex (without even taking into account coverage of sulcal folds). Next-generation invasive electrophysiology will likely record from several hundred or thousands of microelectrodes simultaneously and reliably.

## **1.3 Electrocorticography**

In a few ways ECoG is particularly suited to increasing channel counts. In addition to high enough resolution to take advantage of more dense arrays than EEG,

ECoG can provide broad cortical coverage less invasively than penetrating electrode arrays. High channel counts for penetrating arrays allow for high densities of electrodes to be placed vertically on the shank, and this is advantageous because they have such high resolution that even tens of microns may provide independent signals. The functional structure of cortex is arranged in vertical columns. Each column is roughly a functional unit, and function varies laterally. Depth arrays provide high resolution within a column, but to record from broad and functionally distinct arrays requires multiple insertions. ECoG is able to provide broad lateral coverage without increasing invasiveness as it lies on the surface. This will become increasingly useful when channel counts are increased enough to allow for both high electrode density and large coverage.

An crucial question in ECoG research is how useful it is at smaller scales. Traditionally ECoG is not considered capable of recording SUA or MUA, and it is usually farther removed from the sources of interest than penetrating arrays which further reduces the effective resolution. Analogous to the case EEG, this raises the question of how small to make the spacing between electrodes due to the inherent limits of resolution caused by volume conduction. ECoG differs, however, in that shrinking the array with a fixed channel count will diminish coverage. Increasing channel counts in EEG is less of a technical challenge and the coverage area is already effectively the whole head. This makes understanding of the micro-scale spatial features and variation of the potentials recorded by ECoG doubly important; cortical coverage is a strength of ECoG and with limited channel counts any increase in density is directly at the expense of coverage.

## **1.4 PEDOT Microelectrode Arrays**

The tool which we used to investigate sub-millimeter scale ECoG, or micro-ECoG, was electrode microarrays fabricated by the Integrated Electronics and Biointerfaces Laboratory ([iebl.ucsd.edu](http://iebl.ucsd.edu)) headed by Professor Shadi Dayeh at UC San Diego. A princi-

pal difficulty in using smaller electrode contact sizes is that it increases the impedance of the electrode. IEBL develops devices with surfaces tailored to biological recordings including drastic reduction in impedance relative to using untreated metal surfaces. This allows contacts down to even tens of microns in diameter to maintain impedances (at the standard 1 kHz) roughly around 100 k $\Omega$ . The typical contact sizes used in the arrays in this work was 20 or 50 microns.

The arrays were laid out in square grids with the type of microarray used in human having inter-electrode spacing of 0.4 mm and the primary type of array used in rodent having spacing 0.2 mm. The 0.4 mm spacing is the same spacing as between the penetrating shanks that make up the 10x10 Utah array common to many BCI studies. For reference, standard clinical grids have spacing of around 10 mm, the term micro-ECoG has been applied for spacing of 3 mm. Millimeter or sub-millimeter usually is seen only in arrays used for small mammals such as rodents. The electrodes we used are an order of magnitude more closely spaced but this is important for understanding by putting the surface potentials "under the microscope". From a signal processing perspective, the spatial bandwidth of the surface potentials is unknown and therefore the sampling theorem cannot be applied until higher spatial frequencies are recorded. It is already known that spatial variation of potentials along the surface of cortex is smaller than vertically/perpendicular. ECoG therefore runs the risk of oversampling at scales larger than intracortical electrodes, and this is made even more important by the reduced coverage caused by increasing the density of an array design.

We set out to answer these questions regarding the spatial properties of surface potentials at sub-millimeter scales. Would the arrays be straightforwardly oversampling, especially in human cortex? The arrays allow us to quantify and visualize the potentials at much smaller scale than most ECoG recordings. The smaller contacts may be sensitive to different phenomena such as spiking activity, or the more closely spaced contacts may



detect spatiotemporal dynamics not seen on typical ECoG grids.

# Chapter 2

## Recording System and Initial Testing

### 2.1 Introduction

Both the electrode arrays and the recording hardware were new and needed to be developed in parallel. There are many requirements of the components to record high quality signals in vivo. From the ability of the electrodes to be placed and remain in good contact with the brain to the system's robustness to interference, damage, and ease of use during surgery, each component plays a role in the quality of the recording.

Open source electrophysiology hardware has made the cost of the equipment necessary for recording significantly cheaper. Commercial electrophysiology systems can cost several thousand, or even tens of thousands of dollars while the reduction in price for open source systems can be about tenfold. This allows researchers much easier access to high quality recording (Siegle et al., 2015), and a notable example is Open Ephys ([open-ephys.com](http://open-ephys.com)) which has been taken up by many labs across the world.

In order to record from human patients the system has to have additional protection in the case of malfunction which is not typically part of open source systems given their bare bones and modular nature. In this work we modified the system and developed procedures to allow it to be brought into the clinic to allow recording of 256 channels at up to 20 KHz with 16 bit resolution in human subjects in the operating room.

Electrocorticography (ECoG) is commonly used clinically and experimentally because it has drastically better resolution than EEG, MEG, or fMRI (Schalk et al., 2008). It is used for more precise localization, for example of the seizure onset zone in epilepsy or to map eloquent cortex prior to tissue resection. Improving ECoG can help improve patient outcomes for over 100,000 neurosurgical cases per year (Taplin et al., 2016), and in driving brain-computer interfaces (BCI) (Schalk et al., 2008; Sahin et al., 2009; Canolty et al., 2006; Mesgarani et al., 2014; Vansteensel et al., 2016; Wang et al., 2013; Chestek et al., 2013).

There is a lot of room for improvement of ECoG electrodes in terms of channel counts and sizes, spatial resolution, mechanical and electrical properties, and biocompatibility (Horton and Adams, 2005; Rubehn et al., 2009). Some of these can be achieved by altering the materials at the interface with the tissue (Vetter et al., 2004; Buzsáki, 2004; House et al., 2006; Hatsopoulos and Donoghue, 2009; Lagoa et al., 2006), by embedding the electrodes in conformable substrates (Green et al., 2012; Abidian and Martin, 2009; Cogan et al., 2016). We aim for our electrode arrays to improve on all these areas by the use of micro-fabricated arrays with surface-modified metallic electrodes (Cogan, 2008; Merrill et al., 2005; Polikov et al., 2005; Kim et al., 2010b; Heim et al., 2012; Park et al., 2010) or metallic electrodes with conductive polymer coatings (Rivnay et al., 2016; ?; Abidian et al., 2009; Ludwig et al., 2006) embedded in a biocompatible and extremely flexible parylene C substrate. The conductive polymer used is PEDOT:PSS for its low electrochemical impedance (Rivnay et al., 2016; Abidian and Martin, 2008), its chemical stability (Groenendaal et al., 2000), and its biocompatibility (Asplund et al., 2009; Kim et al., 2010a).

Our goal is to validate the ability of the micro-ECoG arrays and recording system to record neural activity with high fidelity, and to further investigate the properties and potential advantages of high density ECoG. We show the use of the the system

for recording intraoperatively from human subjects and that we see benefits in various features of the neural signal at this scale including modulation of high gamma activity at the scale of the arrays' sub-millimeter electrode pitch.

## **2.2 System Design**

The system of built around hardware made by Intan Technologies (Los Angeles, CA). The Intan system is low cost while still having hundreds of channels and custom designed circuitry for recording small biopotentials. Their hardware is the basis for the open source systems Open Ephys and Willow and is used in commercial systems as well.

### **2.2.1 Hardware**

For the recording system to be clinic compatible it has to be electrically and mechanical isolated from the patient to prevent and in the case of malfunction. The board was electrically isolated (Figure 2.1c) using inductive iCoupler technology (ADUM6000 & 4401 series) from Analog Devices (Norwood, MA) to comply with the standard for safety and effectiveness of electrical medical equipment IEC-60601 and the UL-1577 isolation standard.

Noise is also a greater concern in the clinical environment due to the presence of other various and necessary electrical equipment which can introduce noise into the electrophysiology system. The Intan system is designed with these kind of interference in mind by having small amplifiers (RHD2164 headstage Figure 2.1b) that can be placed as close as possible to the subject and digitize the signals as early as possible in the chain of wires leading between the brain and the acquisition system (Figure 2.4).

An added benefit of amplifying and digitizing the signals close to the brain is that there are fewer wires for the clinicians to handle as the digitized signals leave each headstage through one cable. Figure 3 shows our clinical setup using a 6 foot digital

cable (Figure 2.1b) to between the headstage and acquisition board. The size of the acquisition hardware (25 x 18 cm) allows it to be placed on a small movable table such as the Mayo. The data acquisition hardware includes of an enclosure that houses the power isolator and the Intan RHD2000 acquisition board (Figure 2.1d) and a laptop to monitor and store the signals. All of the electronic components are housed in plastic enclosures to avoid short circuits caused by saline solution or bodily fluids coming in contact with any components of the system.

**Table 2.1.** List of variously used common ephys systems, (Siegle et al., 2015; Newman et al., 2013; Kinney et al., 2015)

System	Ch	F <sub>s</sub> , Bit Depth	Isolated
Blackrock Cerebus	128	30 KHz, 16 b	Y
TDT PZ2	256	50 KHz, 18 b	Y
Open Ephys	256	30 KHz, 16 b	N
NeuroRighter	64	1 MHz, 16 b	N
Nspike	127	30 KHz, 16 b	N
UCSD	256	20 KHz, 16 b	Y
Willow	1024	30 KHz, 16 b	N

## 2.2.2 Software

To interface with this system, we use a slightly modified version of Intans compiled software or Open Ephys GUI. Without the modification, the software will not recognize the hardware due to additional time delay in the SPI signal path caused by the isolator and cabling. This also limits the sampling rate to up 20 kHz as opposed to 30 kHz, which is the highest sampling rate for RHD2164 and RHD2132. Compatible software along with design files, schematics and documentation for this system are available for download at [github.com/tne1-tbd.com](https://github.com/tne1-tbd.com).

### **2.2.3 Device Fabrication**

The devices were fabricated by the Integrated Electronics and Biointerfaces Laboratory ([iebl.ucsd.edu](http://iebl.ucsd.edu)) headed by Professor Shadi Dayeh at UC San Diego. The substrate for the devices is parylene C which was deposited by chemical vapor deposition. The metal leads were made of a 10 nm Ti adhesion layer and 100 nm Au contact layer deposited with an electron beam evaporator and the contacts were coated with PEDOT-PSS. Full methods are available in Ganji et al. (2017b)

## **2.3 Experiment**

### **2.3.1 Pre-Operative Methods**

Prior to surgery, the recording electrode and parts of our recording system that are in or close to the sterile field must be sterilized - a process which attempts to eliminate all microorganisms (Figure 2.4). The recording electrode was sterilized with steam sterilization at 132° C for 10 minutes and the electrode adapter, headstages, and cables were sterilized using a low temperature process called Sterrad at 50° C for 45 minutes, which is compatible with electronic components. Sterrad uses a combination of hydrogen peroxide vapor and low temperature gas plasma to eliminate toxic residue. We packaged the adapter and headstages in 3D printed cases made of PLA plastic to reduce the risk of damage during handling and sterilization. After multiple iterations, we found no visible deficits in the electronics and they remain fully functionally. On the other hand, thin film devices have been damaged, necessitating extra care during packaging. We found that damage typically occurs near the bonding interface where the device substrate (4 um parylene C) and the anisotropic conductive film (ACF) & flat flexible cable (FFC) mate. By fixing the more rigid ACF / FFC cable with Kapton tape and allowing the parylene C substrate to freely move, damage of risk is reduced.

To validate the performance of our ephys system we recorded from a patient undergoing neurosurgery, both during heavy anesthesia and while performing an auditory lexical decision task. The task consists of monitoring a stream of spoken and noise-vocoded bi-phoneme phrases (taw, koo). During the surgery, the patient is woken up from heavy anesthesia to perform clinical mapping of language abilities.

### **2.3.2 Intra-Operative Methods**

The intra-operative methods consist of three major steps: testing electrodes, implanting electrodes and performing task with the patient. The sterile equipment and electrodes are unpacked and connected to data acquisition hardware, while carefully ensuring sterility is not broken. A small bucket of saline is prepared where the devices and a handheld signal generator (HPG1 Velleman) are placed. A differential signal between the small sites and large sites (reference) is measured with ground connected via a separate needle electrode. The electrode adapter has switches to connect any combination of the large sites to reference, which is done to maximize signal to noise. We found that connecting two neighboring large sites to reference provided the best signal by visual inspection. After reference selection, we perform an impedance test using this built-in capability of the RHD2164. The thin film device used in this case yielded 77% (46/60 electrodes) less than 30 k $\Omega$ . The electrode device was placed on top of arachnoid mater. The location of the implant was posterior superior temporal gyrus. Approximately 20 minutes total of baseline activity, task activity and anesthetized activity were recorded.

### **2.3.3 Electrophysiology**

Patients S1-S3 undergoing clinical mapping of eloquent cortex provided informed consent to have the microarray placed on their pial surface and to participate in a 10 min task. The PEDOT microarray was placed on the STG: anterior STG for S2 and posterior

STG for S1 and S3. UC San Diego Health Institutional Review Board (IRB) reviewed and approved study protocol.

Patient S4 provided informed consent to have microarray placed on their pial while unconscious. The electrode was implanted on the lateral surface of the temporal lobe across the superior and middle temporal gyrus. The Partners Human Research Committee reviewed and approved the IRB protocol at Brigham and Women's Hospital.

S2 read visual words, repeated auditory words, and named visual pictures. S3 saw a three-letter string (GUH, SEE) and then heard an auditory two-phoneme combination, making a decision whether the visual and auditory stimuli matched. Interspersed were visual control trials in which a false font was followed by a real auditory stimulus and auditory control trials in which a real letter string was followed by a six-band noise-vocoded two-phoneme combination.

The clinic compatible, open source electrophysiology (ephys) system was used based on Intan technology (Los Angeles, CA) to record acutely during neurosurgery. The details of the system have been published<sup>32</sup> and the design files and software are freely available on <https://github.com/TNEL-UCSD/nacq> and are briefly discussed below.

The system was capable of recording 256 channels at 20 kHz and featured 5 kV RMS power isolation. The purpose of an isolator was to protect the patient from hardware malfunctions and/or power surges. The system consisted of an adapter, amplifier and digitizer (Intan RHD2164), power isolator, and USB buffering board (RHD2000). The adapter had switches, which could connect a subset of electrodes to reference (REF) or ground (GND). Typically, two macrodots were connected to REF while GND was connected to an external needle probe (The Electrode Store, Buckley, WA) that was inserted in the scalp near the craniotomy. The signals were then amplified and digitized by the RHD2164, passed through the power isolator, then buffered and sent via USB to a laptop.



Since ephys components were within several feet of the surgical site, these components were sterilized via standard methods at each of the participating hospitals. The adapter and RHD2164 were sterilized using an electronics friendly process called Sterrad. Sterrad was a low-temperature sterilization method that uses hydrogen peroxide plasma to eliminate microbes. It was found that there were no obvious effects to the hardware in the first three to five sterilization runs.

The clinical recording system was an Xltek with 128 channels (Natus Neurology, Pleasanton, CA). For patients S1-S3, the sampling frequency was 500 Hz (70 Hz cutoff) and for S4, it was 250 Hz (83.33 Hz cutoff). Clinical signals were referenced using a bi-polar configuration, which enhanced signal differences between recording channels. On the other hand, research electrodes were measured with a unipolar configuration which resulted in measuring signals with less differences.

### **2.3.4 Analysis and Statistical Methods**

The following software and toolboxes were used: MATLAB, EEGLAB, and the Fieldtrip, Chronux toolboxes.

Time series, power spectral densities under various conditions and spectral features before and after auditory stimuli were examined. Recorded data was sampled at 20kHz and filtered with lower and upper cutoff frequencies at 0.1 and 7500 Hz respectively. Data was analyzed by writing custom Matlab software and using EEGLAB (Delorme and Makeig, 2004).

In Figure 2.8, power spectral densities were estimated using Welch's method (pwelch) using a Kaiser Window of length 0.75 s with  $\beta = 4$ . An entire time period of 10 s was used with 50% between windows. Pointwise c.i.s were computed using the Matlab pwelch function and the expression for c.i. was equation 5.3.64 on page 280 in Manolakis et al. Power in the 10-50 Hz band was obtained by forward and reverse filtering the

signal with a third-order IIR Butterworth filter and then the resultant was squared. To determine statistical significance, the two epochs were windows into 0.5 s nonoverlapping segments. Power was estimated for all windows across the two conditions and then run through Wilcoxon signed rank sum test to determine significance. The absolute median difference of the PSD estimate was computed over the 10-50 Hz to gauge separability across frequencies. The time-frequency plot was generated using short-time Fourier transform method with Slepian tapers (mtspecgramc from the Chronux toolbox). The moving window was of length 400 ms and step 40 ms. A time-bandwidth product of 5 and 5 tapers were used. The power was converted to units of dB then z-scored across to highlight temporal dynamics.

Figure 2.9 uses the same method to compute PSDs as Figure 2.8. The only difference was that a time period of 20 s was used.

For the analysis in Figure 2.10, the data were low-pass filtered at 400 Hz and then downsampled to 1000 Hz (Oostenveld et al., 2011). To remove noise, the average signal of the microdot electrodes was subtracted from each channel (average re-reference) and each channel was then bandstopped around line noise and its harmonics. Next, the data were epoched to the onset of stimulus presentation (visual word/picture/auditory word onset for S2, visual word onset for S3) and for each trial the baseline from 300 to 0 ms was subtracted. Trials judged to have artifactually high amplitude or variances were removed from the data set. To investigate differences between stimulus classes in the high-frequency band, amplitude was obtained using a fourth-order Butterworth bandpass filter from 70 to 170 Hz and then taking the analytic amplitude from the Hilbert transform and smoothed with a moving window. ANOVAs were run between stimuli classes and corrected for multiple comparisons with false-discovery rate (Benjamini and Hochberg, 1995). S2 had 60 trials for each condition (visual word, auditory word, visual picture). S3 had 157 trials for the human voice and 80 trials for noise-vocoded

stimulus. For the time-frequency plots, epochs were transformed from the time domain to the time-frequency domain using the complex Morlet wavelet transform. For the HFB frequencies, constant temporal and frequency resolution across target frequencies were obtained by adjusting the wavelet widths according to the target frequency. The wavelet widths increased linearly from 14 to 38 resulting in a constant temporal resolution of 16 ms.

## **2.4 Results**

### **2.4.1 Initial Testing Results**

A sample of the downsampled time series shows delta, theta and alpha oscillations (Figure 2.5c). Power spectral densities on a 16 s time window shows a clear distinction for two different states: performing task and heavily anesthetized. In the anesthetized state, there is a shift upwards in power between 0-50 Hz, with a bump around 15 Hz due to spindling, which is consistent with previous work with Propofol anesthesia (Murphy et al., 2011; Breshears et al., 2010). Plotted in Figure 2.6 is an exemplary channel.

ECoG signals from auditory stimulus trials were bandpassed at 15-30Hz ( $\beta$ ), and at 70-110 Hz (high- $\gamma$ ). Channels with obvious noise and high impedance were removed from this analysis leaving 46 channels. Additionally, we aggregated all stimuli types and both large and small electrodes together for this analysis. The root mean square (RMS) of the signals in 400 ms windows before and after a stimulus presentation was computed. The pre-stimulus and peri-stimulus windows begin 400 ms before the stimulus onset and 250ms after onset, respectively. 4 out of 46 channels showed a significant decrease after onset in  $\beta$ , and 33 out of 46 showed a significant increase in high- $\gamma$  ( $p < 0.05$  Bonferroni corrected) as expected (Edwards et al., 2009). Data from the channels with the most significant differences in  $\beta$  and high- $\gamma$  are plotted in Figure 2.7. Future studies

will explore these site-specific differences in more detail.

## **2.4.2 Human Electrocorticography**

Having shown the favorable characteristics of our PEDOT:PSS electrodes compared to Pt electrodes, next we assessed our electrodes' ability to measure human electrophysiological activity. We performed intraoperative recordings in both anesthetized patients and patients undergoing clinical mapping of eloquent cortex during epilepsy and tumor resection surgery. The recordings reported consist of testing with four individuals: three at UC San Diego (UCSD) Thornton Hospital (La Jolla, CA) and one at Brigham and Women's (BW) Hospital (Boston, MA). At UCSD, we performed recordings using PEDOT:PSS from Subject 1 (S1) both while awake and while unconscious, and from Subjects 2 and 3 (S2 and S3) while performing a cognitive task. At BW, Subject 4 (S4) was unconscious during the recordings.

As an initial analysis, we demonstrate that PEDOT records comparable activity to current clinical electrodes (Figure 2.8). Here we compare electrophysiology from the macrodot Pt (clinical electrodes), versus the macrodot and microdot PEDOT:PSS electrodes during two different states for S1 when the electrodes were implanted on the anterior superior temporal gyrus (STG). The first state is awake and is engaged in an audio-visual task (see the Experimental Section for details) versus the second state of anesthesia with Propofol and Dexmedetomidine. As expected there were readily observable differences in electrophysiological recordings between the two states as illustrated in power spectral densities (PSD) (Figure 2.8a-c), time-frequency plots and time series (Figure 3d-g). There is markedly higher power in the anesthetized condition and in particular in the 12-17 Hz range, indicative of spindle-like activity (Figure 2.8a-c). Spindling has been reported in deeply anesthetized patients under the drug Dexmedetomidine (Huupponen et al., 2008). Time-frequency plots also appear to show spindling and other dynamic

neural activity (Figure 2.8d,e). Clinical ECoG using standard of care electrodes (3 mm Pt) were recorded alongside PEDOT ECoG. A PSD of a clinical electrode shows comparable effects to those measured by the PEDOT electrodes: (1) increased power during the anesthetized condition and (2) a prominent peak around the alpha range for the task condition. Each electrode showed a significant difference in power in the 10-50 Hz band (Figure 2.8a-c). However, there is variation in the PSD difference magnitude between the clinical and PEDOT for these measurements. The absolute median difference across 10-50 Hz frequencies is 2.4, 6.2, and 7.8 dB for clinical-, macro-, and microelectrode, respectively. Furthermore, the 95% pointwise confidence intervals (c.i.s) for the two PSD conditions begin to overlap at successively high frequencies: 30, 42, and 44 Hz, for a clinical, macro, and microelectrode, respectively (Figure 2.8a-c); it is important to note that these simultaneous recordings were made from different cortical sites, centimeters apart, which is likely a source of variation in the measured physiological response across electrode types. The critical observation is that the expected physiological modulation observed in the clinical ECoG is also seen in micro PEDOT electrode.

Another example of consistent physiological effects observed across electrode types is shown in Figure 2.9. S4 was undergoing a standard nondominant temporal lobe resection. Prior to removal, clinical and PEDOT electrodes were placed on the lateral surface of the temporal lobe across the superior and middle temporal gyrus. After recording under usual anesthetic conditions, a dose of Methohexital (Brevital) was administrated with the intention of increasing epileptiform activity Kofke et al. (1997); Wyler et al. (1987). As expected, this caused a noticeable increase in epileptiform activity after several minutes as illustrated in the time traces across the electrode types (Figure 2.9a,b). The time traces are taken over two windows: T1 which was shortly after the Methohexital dose and T2 which occurred 200 s after T1. PSDs for T1 and T2 are plotted for clinical, PEDOT macro, and micro (Figure 2.9c-e, respectively) showing the same

trend: more activity in T2. However, when computing the difference in power for the 10-50 Hz band, only the PEDOT electrodes showed a significant difference. Again, the measured variation can also be explained by differences in neural activity across several centimeters of cortex. As with the previous subject, the PEDOT microelectrode shows a significant difference between baseline and increased epileptiform activity demonstrating their potential clinical utility.

To further examine spatial specificity, we analyzed stimulus-locked cognitive activity in two patients. Recordings were made from the anterior STG for S2 (Figure 2.10a) and from the posterior STG for S3 (Figure 2.10d) while each was awake for the clinical mapping of eloquent cortex. While awake, each also performed a short task (see the Experimental Section). S2 verbally responded on >95% of naming trials and S3 made a correct match/mismatch decision on 98% of trials.

Spectrograms demonstrated increases in high-frequency power specific to certain stimuli classes: auditory words for S2 (Figure 2.10c) and noise-vocoded stimuli for S3 (Figure 2.10f) Souza and Rosen (2009). The most consistent difference across electrodes was in the frequency ranges commonly referred to as high-gamma, here defined as 70-170 Hz (Figure 2.10c,f shows the responses for three neighboring example channels from each subject). This high-frequency band amplitude (HFB) is highly correlated with population neuronal firing rates Ray et al. (2008). To better assess this HFB response, we looked at the response averages across electrodes.

Of the 56 microcontacts, 42 in S2 and 34 in S3 were functional, as determined by impedance <60,000 ohms. While reference autoclave experiments here and Uguz et al. (2016) showed negligible influence on the microarray impedances (Figure ??), some of the microarray dots displayed higher impedances after transportation and autoclave by hospital personal as determined by impedance measurements just prior to the recordings and is attributed to issues in handling the arrays rather than the autoclave process itself.

In S2, 16 of 42 good electrodes demonstrated a significant ( $p < 0.05$  false-discovery rate corrected) increase to auditory words relative to visual words and pictures (38% of electrodes). In S3, 31 of 34 electrodes demonstrated a significant increase ( $p < 0.05$  false-discovery rate corrected) to auditory noise-vocoded trials relative to human voice trials (91% of electrodes). S3 also saw a visual bigram prior to the auditory stimulus, but showed no significant response across electrodes to visual stimuli. Figure 2.10b,e shows the HFB of the six example electrodes chosen from a 3 x 2 portion of the grid, demonstrating that the presence of an effect and the variability of the effect size can vary across distances as small as 400  $\mu\text{m}$

## 2.5 Discussion

Electrophysiology in the operating room imposes additional constraints, but we have demonstrated the ability of a modified affordable open source electrophysiology system to be used in the clinic. It meets the standards of safety required in the clinic while being able to record hundreds of channels with high enough quality for detection of action potentials and other high frequency, small amplitude biopotentials. The system is modular, built on Intan Technology components and custom ones to allow it to be changed for different needs or purposes.

The system was brought into the clinic and we were able to validate the signals using basic spectral features. This important step will allow the system to begin being used for more complex studies that will more fully take advantage of the microelectrode arrays and better understand their capabilities.

In parallel with testing the system we were able to demonstrate the use of the PEDOT:PSS microarrays for recording baseline and stimulus-related human neural activity. We show there are spatial variations at sub-millimeter scale of the signal including relevant features such as high gamma activity. It is important to understand

the spatial aspects due to the use of ECoG in localization and the relatively high spatial specificity of signals used in brain-computer interfaces. Improving resolution will allow ECoG to further improve patient outcomes by better mapping important cortical regions prior to resection (Kim et al., 2010b; Heim et al., 2012; Park et al., 2010; Green et al., 2008; Abidian et al., 2010; Cui et al., 2001) and BCI performance due to the small cortical regions critical to high-performance BCI. Our work shows the advantage high density grids have over typical clinical grids. Although in our device this benefit is at the cost of cortical coverage due to the similar channel counts, as hardware enables an increasing number of channels to be recorded simultaneously the tradeoff will be less severe and ECoG can maintain reasonable coverage while also having higher than the current standard electrode density. Nonetheless future high channel arrays will have to be designed with this tradeoff in mind and understand how much benefit there is to using electrodes arrays at micro scales.

Chapter 2, in part, is a reprint of the material as it appears in A Clinic Compatible, Open Source Electrophysiology System in Engineering in Medicine and Biology Society (EMBC), 2016. Hermiz, John; Rogers, Nick; Kaestner, Erik; Ganji, Mehran; Cleary, Dan; Snider, Joseph; Barba, David; Dayeh, Shadi; Halgren, Eric; Gilja, Vikash. The dissertation author was a co-investigator and co-author of this paper.

Chapter 2, in part, is a reprint of the material as it appears in Development and Translation of PEDOT: PSS Microelectrodes for Intraoperative Monitoring in Advanced Functional Materials, 2017. Ganji, Mehran; Kaestner, Erik; Hermiz, John; Rogers, Nicholas; Tanaka, Atsunori; Cleary, Daniel; Lee, Sang Heon; Snider, Joseph; Halgren, Milan; Cosgrove, Garth Rees; Carter, Bob S.; Barba, David; Uguz, Ilke; Malliaras, George G.; Cash, Sydney S.; Gilja, Vikash; Halgren, Eric; Dayeh, Shadi A. The dissertation author was a co-investigator and co-author of this paper.



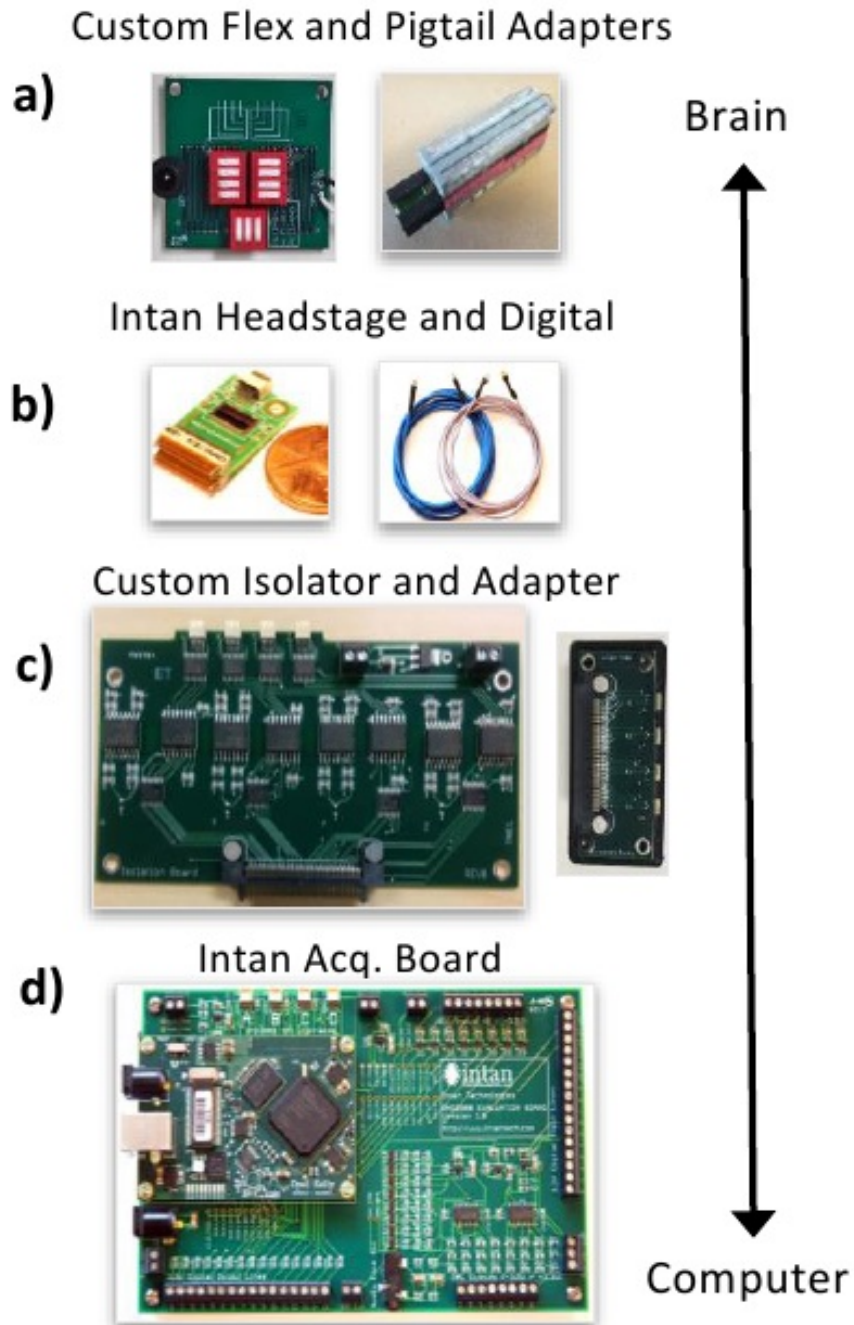


**Figure 2.1.** a) Electrode adapters: (left) connects to flat flexible cables (FFC) of 32 or 64 channels with 0.5 mm pitch and features switches that allows the user to short various electrodes to reference; (right) can connect up to four 16 channel standard pig tail connectors. Both adapters mate to Intan RHD2164 or RHD 2132 headstages using an Omnetics connector (part : A79032-001). B) (left) Intan RHD2164 headstage and (right) Intan SPI cable C) (left) Custom power isolator that can handle 4 RHD2164 headstages or up to 256 channels and (right) accompanying adapter. (D) Intan RHD2000 acquisition board. Reproduced from Hermiz et al. (2016).



**Figure 2.2.** The power isolator and RHD2000 Board are housed in grey enclosure. Two RHD2164 headstages are connected to the system to the electrode adapter housed in 3D printed cases. Reproduced from Hermiz et al. (2016).

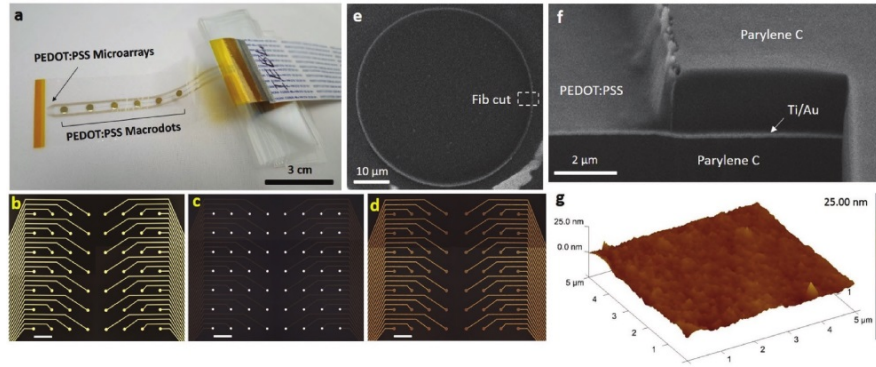


**Figure 2.3.** a) A picture of the fabricated electrophysiology PEDOT:PSS device on thin film parylene C layer showing the location of microarrays with 56 microdots at the top of the probe and above the 6 macro REF electrodes. Optical microscope image of the microelectrodes after b) Ti/Au deposition and lift-off process, c) selective parylene C oxygen plasma etching to expose the gold electrodes, and d) definition of PEDOT:PSS layer on top of only the metal microelectrode sites (scale bars  $400\ \mu\text{m}$ ). e) Top view SEM image of the circular PEDOT:PSS microelectrode with  $50\ \mu\text{m}$  diameter. The white contrast in the lower right of the image is the result of electron charging on parylene C and does not signify a morphological detail. The dashed white box highlights the location of FIB cut. f) Slanted view SEM image showing the cross-section of the device and the stacked layers highlighting conformal and intimate contact between the different layers of the device and exposure of PEDOT:PSS as the only electrochemical interface. g) 3D AFM topography image of a  $5 \times 5\ \mu\text{m}$  scan area of PEDOT:PSS film after autoclave sterilization showing smooth and uniform morphology (compared to before sterilization, not shown) and the absence of voids in the film. Reproduced from Ganji et al. (2017b).

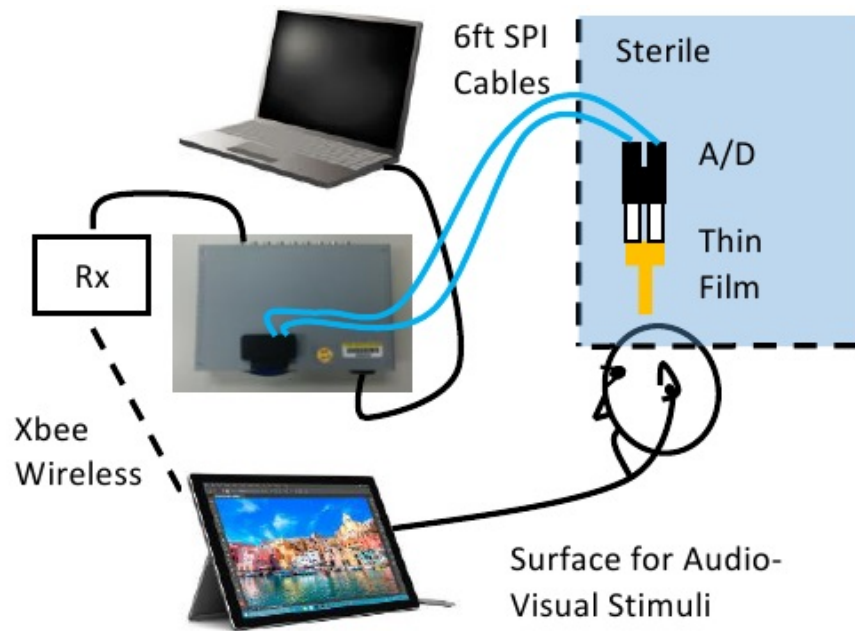


**Figure 2.4.** Electrode device, adapter, headstage and part of the SPI cable are in the sterile field. Audio and visual stimuli are presented through a Microsoft Pro Surface 3. Stimuli trigger is sent wirelessly to a receiver that connects to an analog to digital channel of the acquisition system. Reproduced from Hermiz et al. (2016)

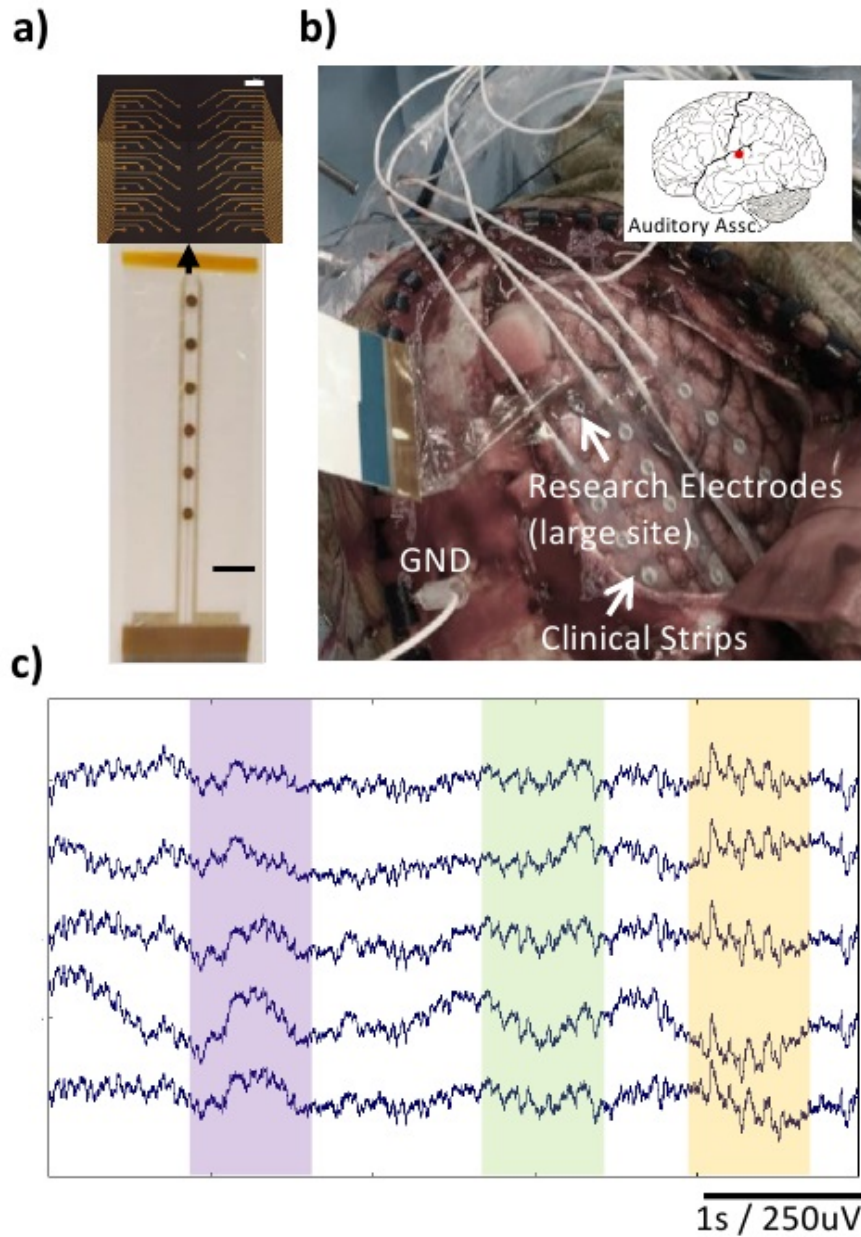


**Figure 2.5.** a) Thin film electrode device with 6 large sites ( $D = 3 \text{ mm}$ ) and 56 small sites ( $D = 40 \text{ μm}$ ) - black scale bar is 1cm. The device substrate is parylene C and the electrodes are coated with PEDOT:PSS. A zoomed in microscopic image of the small sites is also shown - white scale bar is 400 μm b) Electrode device was implanted in auditory association cortex. Also shown are clinical strip electrodes. c) Raw time series downsampled to 2kHz showing delta (purple), theta (green) and alpha (orange) oscillations - scale bars are 1 s and 250 uV. Reproduced from Hermiz et al. (2016)

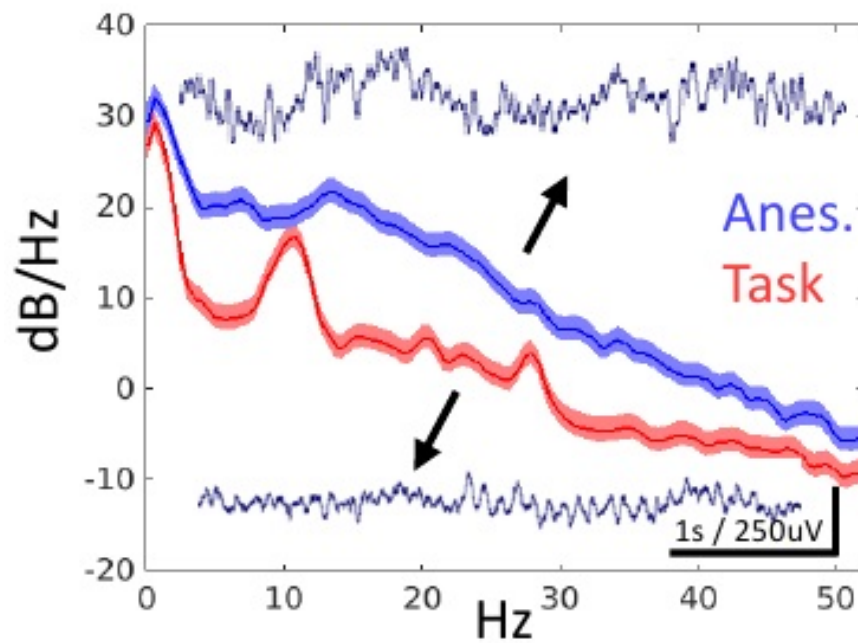


**Figure 2.6.** a) Power spectral density on 16-sec time series while patient was anesthetized (blue) and awake and performing an audio task (red). Shown as insets are snippets of the raw time series with scale bar 1 s and 250  $\mu$ V. Reproduced from Hermiz et al. (2016).



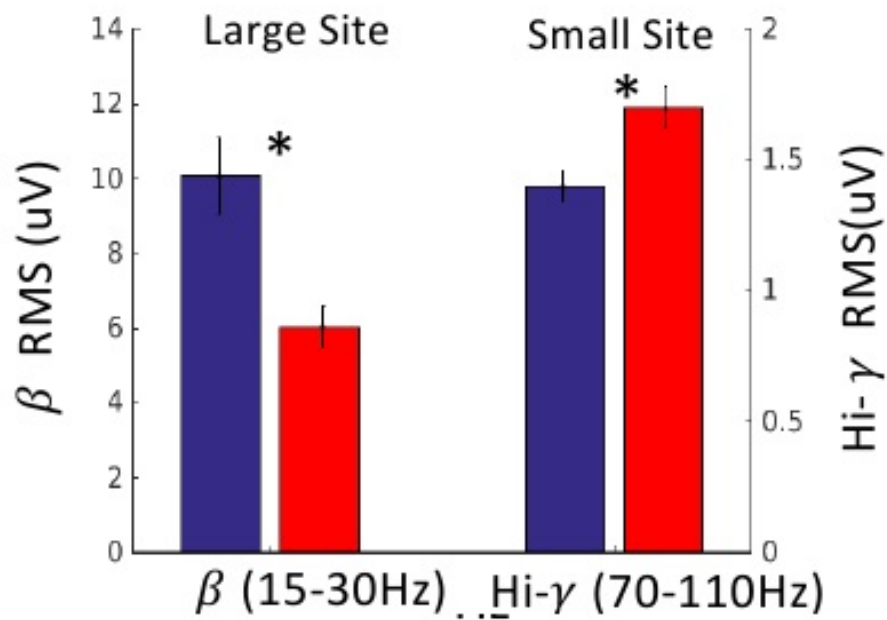


**Figure 2.7.** Mean  $\beta$  and high- $\gamma$  RMS before (blue) and after (red) stimuli onset are plotted along two y-axes. The most significant differences are shown. Error bars represent S.E.M with  $n = 59$ . Asterisk denote significant decrease and increase ( $p < 0.05$  paired t-test, one tail, Bonferroni correction). Reproduced from Hermiz et al. (2016).

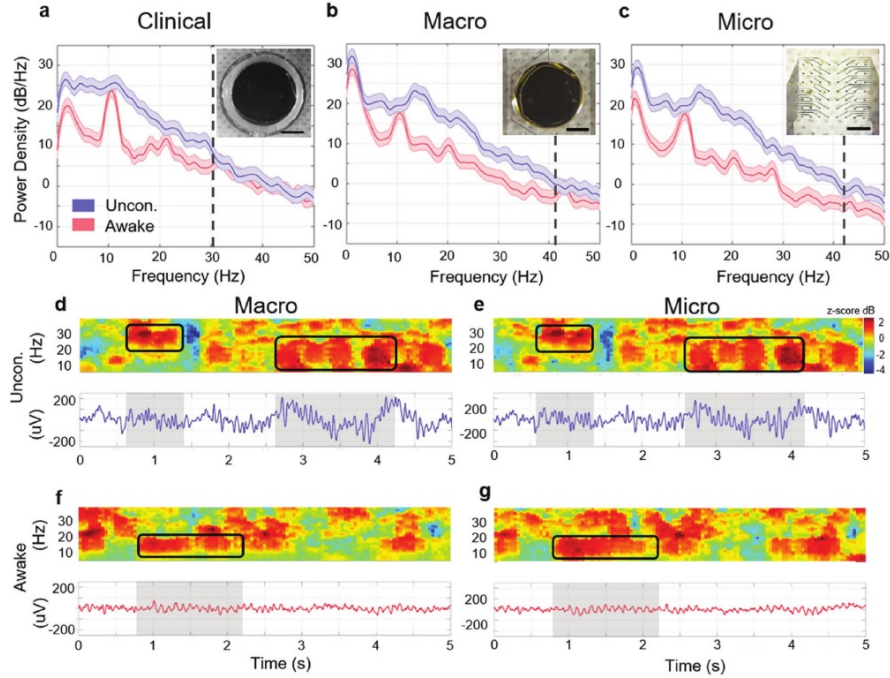


**Figure 2.8.** Power spectral densities (PSDs) between the two conditions (awake vs unconscious) for a) clinical electrode, b) PEDOT macro, and c) microdot. Inset of (a) shows optical image of clinical Pt macrodot and panels (b) and (c) show optical image of PEDOT:PSS macrodot and an array of 56 microdots (scale bars 1 mm). The dark blue and red lines are average PSD estimates from overlapping time windows and the lightly colored shaded regions are the 95% pointwise c.i. (see the Experimental Section). Power over the 10-50 Hz band shows significant differences between the two conditions for all electrodes:  $8.9 \times 10^5$  (clinical),  $1 \times 10^4$  (macro), and  $8.9 \times 10^5$  (micro) (Wilcoxon signed rank test). The absolute median difference between 10-50 Hz of the estimate power density is 2.4, 6.2, and 7.8 dB for clinical-, macro-, and microelectrode, respectively. The dashed black line at 30, 42, and 44 Hz for (a)-(c) mark the frequency at which the c.i.s start to overlap for frequencies  $>15$  Hz. Time-frequency and corresponding time series are shown for a sample 5 s window for the unconscious (d and e) and awake condition (f and g). The rectangles highlight increases in beta (20-30 Hz) and spindling activity (12-17 Hz). Color axis represents standard deviations away from the mean for each frequency. The time window per condition for macro and micro are nearly identical. Reproduced from Ganji et al. (2017b).



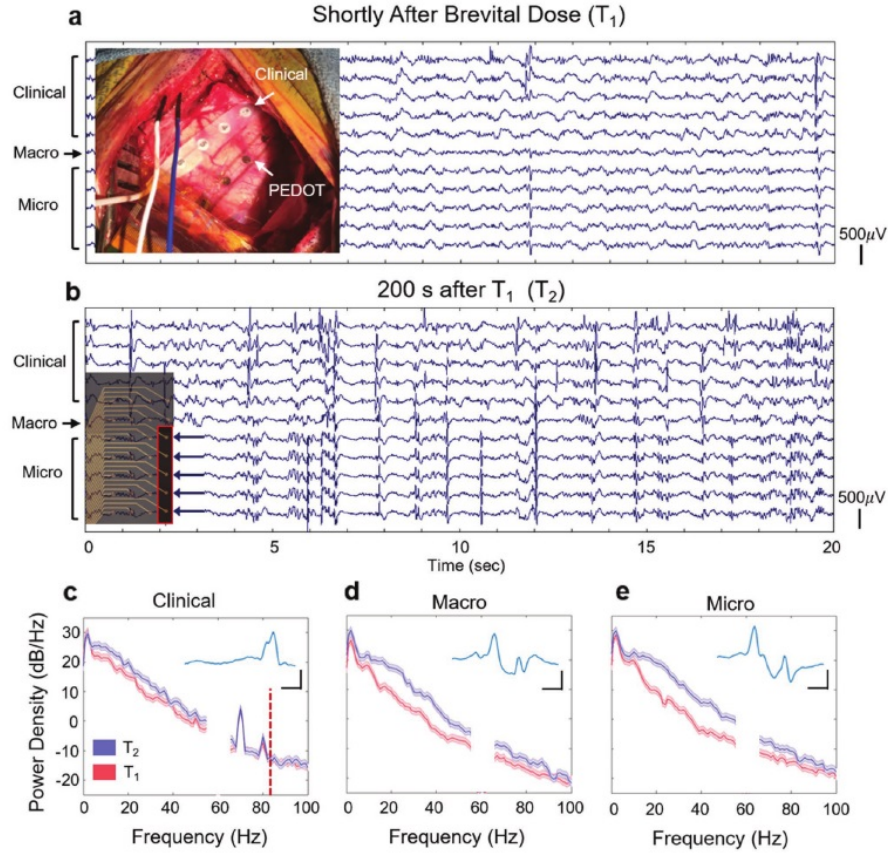


**Figure 2.9.** a) Simultaneously captured ECoG traces from clinical, PEDOT macro, and micro electrodes shortly after Methohexital dose ( $T_1$ ) and b) 200 s after  $T_1$ , ( $T_2$ ). Inset in (a) shows the clinical and PEDOT ECoG probes implanted over the superior and middle temporal gyrus. Inset in (b) shows which microelectrodes are plotted for (a) and (b). Power spectral densities of a c) clinical, d) macro, and e) micro electrode taken from  $T_1$  (red) and  $T_2$  (blue). The dark blue and red lines are average PSD estimates from overlapping time windows and the lightly colored shaded regions are the 95% pointwise c.i. (see the Experimental Section). Power in the 10-50 Hz band show significant differences only for PEDOT electrodes: 0.010 (clinical),  $5.5 \times 10^6$  (macro), and  $4.3 \times 10^6$  (micro) (Wilcoxon signed rank test). The noise spectra around 60 Hz frequency was filtered out with a notch filter for all devices. The dashed red vertical line in (c) indicates the upper passband cutoff frequency for the clinical system. Insets from (c)-(e) show an interictal epileptic discharge (IED) captured concurrently across the three electrode types. Scale bars are 200  $\mu V$  (vertical) and 50 ms (horizontal). Reproduced from Ganji et al. (2017b).

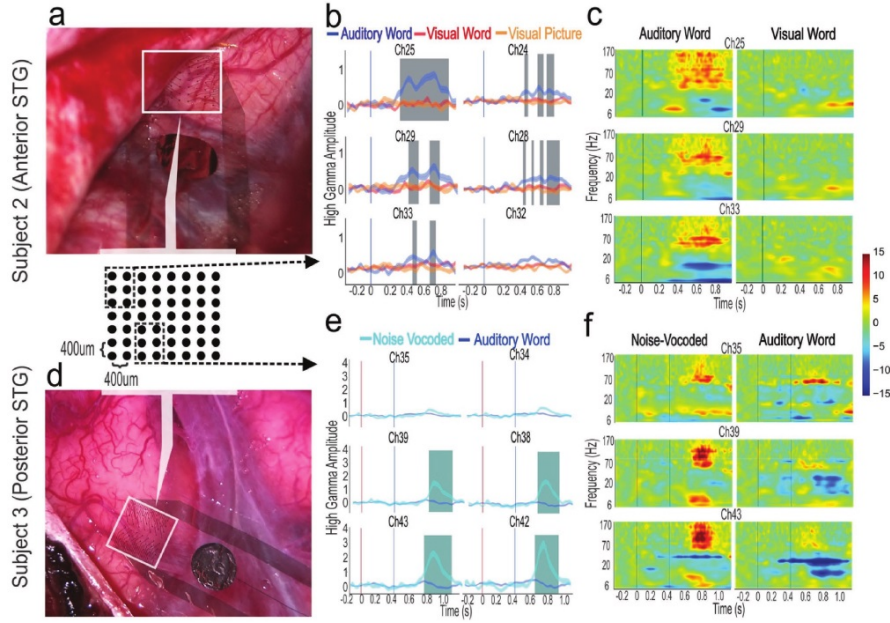


**Figure 2.10.** a,d) Electrode placement from the two subjects who performed cognitive tasks. Activity from six neighboring electrodes (3 x 2 electrodes) from the 8 x 7 electrode array is displayed to illustrate high-frequency amplitude variation. The white box highlights device placement (device partially obscured in subject 1 by the dural flap). b,e) High-frequency amplitude for the 3 x 2 channels confirming significant differences in Hilbert analytic amplitude from 70-170 Hz between stimuli classes (shaded regions are anova fdr-corrected significant differences). For subject 2, the blue vertical line indicates stimulus onset. For subject 3, the red vertical line indicates visual stimuli onset (to which no response was found across the electrodes) and blue line indicates auditory stimulus onset. c,f) Time-frequency plots from three of the example channels (3 x 1) in response to different stimuli classes demonstrating strong differences in higher frequencies. Displayed is trial-averaged power determined by wavelets. Reproduced from Ganji et al. (2017b).

## **Chapter 3**

# **Spatial Characterization of Surface Potentials at the Sub-Millimeter Scale**

### **3.1 Introduction**

Electrical recording from the brain surface, known as electrocorticography (ECoG), is becoming more common due to technological advances that enable recording from large cortical surface area with high temporal resolution and far better spatial resolution than non-invasive EEG (Nakasato et al., 1994; Ramon and Holmes, 2014). ECoG has also been used as an alternative to penetrating intracortical recording electrodes in brain-computer-interface (BCI) applications (Chao et al., 2010; Schalk and Leuthardt, 2011; Krusienski et al., 2011; Wang et al., 2013; Thakor, 2013; Rouse et al., 2016; Slutzky et al., 2010) due to its less invasive nature and long-term stability that are important features for driving drive BCIs (Chao et al., 2010). Electrodes designed for BCI will typically have more closely spaced electrodes to target specific cortical regions compared to clinical ECoG, in which large cortical coverage is important. Recently, high density ECoG grids have become more common, and many questions on the properties, uses, and design of these grids, e.g., what is the optimal spacing for the electrodes (Rouse et al., 2016; Slutzky et al., 2010; Wang et al., 2017; Hermiz et al., 2018), remain to be answered.

Recording hardware sets an upper limit on the number of channels that can be simultaneously recorded. This creates a tradeoff in designing ECoG electrode grids between coverage and resolution. Clinical grids are typically on the larger coverage side, with 1 centimeter being a typical pitch between electrodes. BCI and research applications have pushed for more resolution in order to place more electrodes near cortical regions of interest (Chao et al., 2010; Wang et al., 2013; Rouse et al., 2016; Slutzky et al., 2010; Wang et al., 2017; Menon et al., 1996; Leopold et al., 2003; Kellis et al., 2016; Muller et al., 2016; O'Neill et al., 2016; Takaura et al., 2016). A challenge of scaling down the size of ECoG grids is that low impedance electrodes improve signal quality, but electrode impedances increase as the contact area decreases (Ganji et al., 2017a). Combining fabrication techniques that allow for smaller, more closely spaced ECoG contacts with novel materials that can significantly reduce impedance makes very small contact sizes feasible. In the present study, we used electrodes coated with PEDOT:PSS on gold traces embedded in a parylene-C substrate (Ganji et al., 2017b,c) with contact diameter as small as 20 microns and pitches as low as 200 microns. Hereafter, we will refer to these ECoG electrode grids as micro-ECoG. Previous work has shown that recordings with micro-ECoG electrodes are more similar to intracortical recordings than to the recordings from larger clinical ECoG electrode grids (Kellis et al., 2016).

The primary signal of interest in ECoG recordings is the lower frequency component (less than 200-500 Hz) called the local field potential or LFP. LFP is an uncertain signal in that its precise physiological and spatial origins are poorly understood (Obien et al., 2015; Herreras, 2016). Much of the difficulty both in studying and using LFP is due to its lack of spatial specificity, that is, the potentials are an aggregate of nearby activity – in contrast to single- or multi-unit electrophysiological signals which are indicative of action potentials very near the recording site (?). The spatial extent of LFP is itself an area of study (Kajikawa and Schroeder, 2011; Lindén et al., 2011; Łeski et al., 2013)

with a dependence on the geometry and activity of the region generating the signal. The spread of the potentials manifests itself in ECoG as similar signals being recorded on different electrodes. This feature of the potentials at different electrodes can be used to interpret the signals (Stam et al., 2007; Casimo et al., 2016) or guide the design of electrode grids to optimally sample the cortical surface.

To quantify the similarity between electrodes, previous studies examined the correlation or coherence of EEG, ECoG, and intracortical electrodes as a function of inter-electrode distance by averaging the correlation or coherence across many pairs separated by the same distance (Rouse et al., 2016; Leopold et al., 2003; Kellis et al., 2016; Muller et al., 2016; Casimo et al., 2016; Bullock and McClune, 1989; Bullock et al., 1995; Nunez et al., 1997). Most of these studies are in human or nonhuman primate, with some early investigations on smaller mammals, reptiles, and invertebrates. In ECoG recordings these studies have shown a consistent nearly monotonic decrease in the correlation as the electrode separation increases that exhibits a roughly exponential shape. Also consistent across the studies is a dependence of the correlation/coherence on the frequency band examined.

It is expected that the correlation/coherence would tend to zero (or bias level) at large distances, and this can be seen in EEG and clinical ECoG Kellis et al. (2016); Bullock et al. (1995); Nunez et al. (1997). On the other hand, the correlation should approach 1 as the separation approaches 0. This is the case because the brain is a conductive medium, and for finite sources distant from the electrode in a volume conductor the potential will be the sum of all of the sources with amplitudes attenuated with distance. The distance at which the similarity will effectively approach 1 will depend on both the geometry of the sources and the properties of the medium. An example of this is discussed in (Bullock and McClune, 1989; Maier et al., 2010), where ECoG correlation between submillimeter-spaced electrodes is mostly close to 1 while correlation between

even more closely spaced intracortical electrode pairs is frequently much lower than 1. This sub-millimeter regime in ECoG is largely unexplored, and at the smallest distances in most previous studies the correlation or coherence is significantly below 1, meaning there is still room to explore smaller electrode spacing.

On the other hand, for practical purposes recording ECoG at the scale in which the neighboring pairs measure very close to the same signal is not optimal because this would mean a large amount of redundancy between channels. The spacing should be guided by the spatial extent of features of interest. It has been suggested that contacts should be less than 5 mm apart for adequate sampling of gamma band in human ECoG (Menon et al., 1996), that for BMI applications subdural electrodes in humans be spaced 1.7 mm apart and in rat 0.6 mm apart Slutzky et al. (2010), and that by halving the spacing of electrodes from 3.5 to 1.68 mm implanted in minipig, more and separate response peaks could reliably be identified in Wang et al. (2017). The optimal separation will depend on factors such as species, location, and the nature of the activity of interest, but in general it will be difficult experimentally to recognize the optimal spatial resolution for a specific application until it is exceeded. However, we expect there may be an approximate resolution to use as a rule of thumb for each species.

We analyze the similarity of micro-ECoG with inter-electrode spacings down to 0.4 mm in human recordings and 0.2 mm in mouse. In agreement with past studies, we found that on average the signals were more similar for more closely spaced electrodes. With exceptions, higher frequency components of the signal showed a larger decrease in similarity with distance.

We also investigated the nature of the pairwise correlation between electrodes across the electrode grid. For a group of closely spaced electrodes to be correlated to each other there must be parts of their signals that are common between each channel pair, and parts that are independent to each electrode. The relative size, distribution, and

properties of these signals determines the correlation between each pair of electrodes across the whole array. There are several analyses that are tailored to finding common signals across multiple channels commonly used on electrophysiological data such as principal component analysis (PCA), factor analysis, or independent component analysis (ICA). We modeled the effect of the properties of the components on the correlation structure, and then used ICA on the data to identify and separate common signals and find how they are distributed across the grid. We found that there are smoothly distributed sources present in the data, and due to the linearity of the ICA decomposition, show that the spatially coherent ICA components account for much of the correlation structure in the data.

## **3.2 Methods**

### **3.2.1 Human Intra-Operative Recording**

The details of the electrodes, their preparation, their implantation, and the recording setup are given in Ganji et al. (2017a,b,c); Uguz et al. (2016). Subjects who were undergoing awake craniotomy surgeries were chosen for recording. The entire section of hardware up to the amplifiers had to be sterilized due to its proximity to the surgical field. The electronics underwent STERRAD sterilization, and it was important to ensure that the devices would remain intact after autoclave sterilization (Uguz et al., 2016). The electrode grid was placed over STG, with larger electrodes within a few centimeters of the grid used as reference electrodes. The ground electrode was placed in the scalp. Recording was sampled at 20 kS/s, with a built-in high pass filter at 0.1 Hz and low pass filter at 7500 Hz. The UC San Diego Health Institutional Review Board (IRB) reviewed and approved the study protocol.

### **3.2.2 Mouse Acute Recording**

ICR mice weighing 25-35 g were used in the experiments. All procedures were in accordance with a protocol approved by the Institutional Animal Care and Use Committees of UC San Diego (protocol S07360). The mice were placed on a heating pad and anesthetized with isoflurane. A femoral artery was catheterized for monitoring and injection, and a tracheotomy was performed for ventilation of the mice. After fixing the skull to a holder using dental acrylic, a craniotomy and durotomy were performed over the right whisker barrel and surrounding cortex. A well was formed around the craniotomy using dental acrylic, and the exposure was kept filled with artificial CSF until the electrode array was placed. Prior to recording the mice were administered pancuronium and artificially ventilated, and prior to stimulus trials the mice were switched to alpha-chloralose anesthesia. The exposure was dried prior to the electrode placement, and then covered with 0.7% agarose made with artificial CSF. The electrodes arrays used were arranged in square grids with either 0.2 or 0.25 mm spacing, and either 50 micron or variable diameter contact sizes. The reference electrode was silver-chloride ball placed between muscle tissue exposed for the craniotomy. Whisker flick stimuli were presented every 2 seconds, and recordings included both spontaneous epochs as well as periods with stimulation.

### **3.2.3 Recording and Pre-processing**

All data was recorded with an Intan RHD2000 system, and the recordings were sampled at 20 kS/s with a high pass filter at 0.1 Hz and low pass filter at 7500 Hz. Channels that by visual inspection were highly contaminated with noise were assumed to be from damaged electrodes removed from further analysis.

Data was then downsampled to 4 kS/s, and 6 FIR bandpass filters were applied, chosen such that they span about 0.6 octaves, have no overlap, not include 60 Hz, and



roughly correspond to physiological bands (theta, alpha, beta, gamma, high gamma): 6-9 Hz, 10-15 Hz, 20-30 Hz, 35-50 Hz, 70-110 Hz, and 130-200 Hz.

Windows of time where the reference signal was more than 35 uV from zero, any one channel was outside +/- 4 mV, or the signal in the highest band was more than 20 times the RMS in that band were marked as potential artifacts and excluded along with 750 ms prior and 1.25 s after. Regions that were not removed in this way but were shorter than 6 seconds were also excluded.

### **3.2.4 Distance-Averaged Correlation**

The data was segmented into continuous 2 s windows. For each window correlation was calculated using Pearsons correlation coefficient for every possible pair of electrodes on the grid. Each channel pair also has an associated inter-electrode distance, and the correlation vs. distance plots are the result of averaging the pairwise correlations with all equally spaced pairs. For a subject the average correlation is calculated by pooling all correlations across time and averaging the values by distance.

### **3.2.5 Component Analysis and Modeling**

PCA and ICA decompose the data matrix,  $s$ , into linear combinations of components,  $z$ , with the transformation, mixing, or weight matrix,  $W$ ,

$$s = Wz \quad (3.1)$$

The components are all uncorrelated with every other component. Therefore, the mixing matrix obtained from either ICA or PCA can be used to whiten the data – which is to linearly transform the data such that the covariance matrix of the transformed data is the identity matrix. PCA is commonly used as for whitening data, and for our purpose ICA can be defined such that it is a whitening transform due to the ambiguity in the scaling

of the components. The components can be arbitrarily scaled so long as the weights are scaled inversely such that the original data is unchanged. We make use of this choice to conveniently express the covariance of the data as a function of the weights

$$\text{cov}(s) = \text{cov}Wz = W\text{cov}(z)WT = WIW^T = WW^T \quad (3.2)$$

Using this result, the correlation matrix can be computed directly from the mixing matrix. For the model we can start with mixing matrices with each components weights being drawn from a two-dimensional Gaussian

$$W_{i,j} = A_j e^{\frac{-(x_j - x_i)^2 + (y_j - y_i)^2}{2\sigma_j^2}} \quad (3.3)$$

where  $i$  is the channel with position  $(x_i, y_i)$ , and  $j$  is the component with location  $(x_j, y_j)$  and standard deviation  $\sigma$ . For our model we sample the components on a 10x15 square grid with 150 components, one per channel, whose center positions are drawn from a uniform random distribution on the 2D space covered by the grid plus one fifth of the standard deviation of the component for which the center is being determined on either side. The amplitudes of each component are drawn from a uniform random distribution between 0.5 and 1.5, sorted in descending order and then scaled by  $e^{-0.1 k}$ , where  $k$  is 1,2,3 corresponding to the first, second, third, etc. amplitude. This is to mimic the trend of decreasing variance for components typically obtained from PCA and ICA. Once the mixing matrix is determined the covariance,  $\Sigma$ , is given as before by

$$\Sigma = WW^T \quad (3.4)$$

The properties of products of Gaussians allows the covariance elements to be rewritten as

$$\begin{aligned}\Sigma_{i,j} &= \sum_{k=1}^N W_{i,k} W_{j,k} = \sum_{k=1}^N e^{-\frac{(x_k-x_i)^2 + (x_k-x_j)^2 + (y_k-y_i)^2 + (y_k-y_j)^2}{2\sigma^2}} \\ &= \sum_{k=1}^N e^{-\frac{2(x_k - \frac{1}{2}(x_i+x_j))^2}{2\sigma^2}} e^{-\frac{2(y_k - \frac{1}{2}(y_i+y_j))^2}{2\sigma^2}} e^{-\frac{\frac{1}{2}(x_i-x_j)^2 + \frac{1}{2}(y_i-y_j)^2}{2\sigma^2}}\end{aligned}\quad (3.5)$$

Separating the terms that involve the distance between channels i and j gives

$$\Sigma_{i,j} = e^{-\frac{d_{ij}^2}{2(\sqrt{2}\sigma)^2}} \sum_{k=1}^N e^{-\frac{2(x_k - \frac{1}{2}(x_i+x_j))^2}{2\sigma^2}} e^{-\frac{2(y_k - \frac{1}{2}(y_i+y_j))^2}{2\sigma^2}} = F_{i,j} e^{-\frac{d_{ij}^2}{2(\sqrt{2}\sigma)^2}} \quad (3.6)$$

Each element is the product of a Gaussian function of the distance between channels and  $F_{i,j}$ , a sum over 2D Gaussian functions of the component positions centered at the average location of two electrode positions, which given a fixed set of component locations, is a function of the two electrodes positions. For uniformly distributed component positions  $x_k$ ,  $F_{i,j}$  looks like a discrete approximation of the integral over  $x_k$  of the 2D Gaussian. In the limit of an infinite number of components uniformly distributed across a sufficiently large area it becomes proportional to the integral

$$F_{i,j} \propto \int_{-\infty}^{\infty} \int_{-\infty}^{\infty} e^{-\frac{2(x_k - \frac{1}{2}(x_i+x_j))^2}{2\sigma^2}} e^{-\frac{2(y_k - \frac{1}{2}(y_i+y_j))^2}{2\sigma^2}} dx_k dy_k = F_0 \quad (3.7)$$

and given that this integral is not a function of the center position of the Gaussian, in this limit  $F$  is a constant regardless of the positions of channels i and j. In this limit the correlation matrix is exactly a Gaussian function of the distance between the channel pairs with a standard deviation square-root of 2 larger than the standard deviation of the

components that generated it:

$$r_{i,j} = \frac{F_0 e^{-\frac{d_{ij}^2}{2(\sqrt{2}\sigma)^2}}}{\sqrt{(F_0)(F_0)}} = e^{-\frac{d_{ij}^2}{2(\sqrt{2}\sigma)^2}} \quad (3.8)$$

For the above form of the correlation to be valid doesn't require that  $F$  is near the limit of infinite components, rather that  $F$  is not a function of the electrode pair  $i$  and  $j$ . For the correlation to take the form above on average is an even weaker condition that  $F$  can be a weak function of the electrode pair in relation to the distance term so that the small factors multiplying the distance term will tend to cancel when averaged over equidistant pairs and multiple DACs.

To include the effect of noise specific to each channel, and uncorrelated from the activity or noise on the other channels, a new component has to be created for each noise element because every component is required to be uncorrelated to all other components. This results in a diagonal matrix of weights which we model as each having the same amplitude,  $\epsilon$ , across channels

$$W_{noisei,j} = \epsilon \delta_{ij} \quad (3.9)$$

Where  $\delta_{ij}$  is the Kronecker delta, not the distance used previously. The effect of a reference electrode which is added to all channels can be modeled as a single component with a constant weight vector across all channels

$$W_{ref} = \rho \quad (3.10)$$

so that the modified mixing matrix is the original mixing matrix with additional columns

for the noise and reference

$$W' = \begin{pmatrix} & & \\ W & W_{noise} & W_{ref} \end{pmatrix} = \begin{pmatrix} \varepsilon & 0 & \rho \\ W & 0 & \varepsilon & \rho \\ & & \ddots & \vdots \end{pmatrix} \quad (3.11)$$

The modified covariance matrix is now given by

$$\Sigma'_{i,j} = \Sigma_{i,j} + \varepsilon \delta_{ij} + \rho \quad (3.12)$$

and its modified correlation matrix  $r$  is given by

$$r'_{i,j} = \frac{\Sigma_{i,j} + \varepsilon \delta_{ij} + \rho}{\sqrt{(\Sigma_{i,i} + \varepsilon + \rho)(\Sigma_{j,j} + \varepsilon + \rho)}} \quad (3.13)$$

### 3.2.6 Independent Component Analysis

ICA was applied using the `runica()` function from EEGLab (Delorme and Makeig, 2004) to the same filtered and segmented 2 second windows that were used to compute the DAC. The built-in PCA option was used to apply PCA prior to ICA as a dimensionality reduction technique, and the extended-ICA option was used. For human data with 56 channel grids the first 30 components were kept, and for mice with 32 channel grids the first 20 components were kept. In both cases the excluded components accounted for less than 5% of the variance in the data, and usually were close to 1

Component mixing matrices were fit using least squares fitting function `lsqcurve-fit()` in MATLAB to a two-dimensional circular Gaussian function with 5 parameters

$$Ae^{\frac{(x-B)^2 + (y-C)^2}{2D^2}} + E \quad (3.14)$$

with lower and upper bounds such that A be positive, B and C to force the center to lie within 40 grid pitches on either side, D to fit to Gaussians that have standard deviations larger than a single grid pitch.

The median width parameter D was chosen instead of the mean due to the distribution of values being skewed towards zero. In order to calculate the 95% confidence interval of the median a bootstrap with 5,000 resamples was used. Only widths corresponding to components with  $R^2$  over 0.7 to exclude components for which a Gaussian is not a good representation and the value of D may not be meaningful.

The individual contribution of each component to the overall covariance matrix can be found by re-calculating the covariance using only the desired component. Any entry in the covariance matrix is a sum over weights corresponding to all components.

$$\Sigma_{i,j} = \sum_{c=1}^N W_{i,c} W_{j,c} \quad (3.15)$$

Therefore, we define the reduced covariance corresponding to a single component, c, as just the terms involving that component. The sum of all of the reduced covariance matrices is therefore the full covariance matrix.

$$\Sigma_{i,j}^c = W_{i,c} W_{j,c} \quad (3.16)$$

The corresponding reduced correlation matrix cannot be calculated as usual

$$r_{i,j} = \frac{\Sigma_{i,j}}{\sqrt{\Sigma_{i,i} \Sigma_{j,j}}} \quad (3.17)$$

because all of the reduced correlation matrices would be identity matrices. Rather the reduced correlation is calculated using the reduced covariance in the numerator, and the

full covariance in the denominator,

$$r_{i,j}^c = \frac{\Sigma_{i,j}^c}{\sqrt{\Sigma_{i,i}\Sigma_{j,j}}} \quad (3.18)$$

so that the sum of all components of the reduced correlation matrices is equal to the full correlation matrix.

The reduced correlations can be averaged by distance in the same manner as the full one. The contribution of each component to the variance, correlation, and drop in the correlation can be calculated using the reduced covariance and correlation. The variances of the channels are the diagonal entries of the covariance matrix, and we will define the overall variance (across channels) as the trace of the covariance matrix. The variance across channels for a given component is then given by

$$Var^c = \sum_{i=1}^N W_{i,c} W_{i,c} \quad (3.19)$$

such that the overall variance is the sum over components, and the percentage of the variance explained by each component is the component variance divided by the overall variance.

We also want to know the contribution of each component to the DAC. The contribution to the DAC is a similar measure to the contribution to the variance, but the contribution to the drop in the DAC is more relevant for explaining the shape of the correlation vs. distance curve. To calculate these, the DAC curve for each reduced correlation matrix is calculated in the same manner as for correlation matrices. The drop in the DAC due to each component is calculated by subtracting the zero-distance value of the DAC from all the values, and it retains the desired property that the sum over all components is equal to the drop in the full DAC.

To summarize the amount each component contributes to the drop in the DAC into a single quantity, the percentage explained is calculated at each distance, and then averaged over all distances. With this, each component can be assigned a percentage of the total variance, total DAC, and total drop in the DAC.

### 3.2.7 Common Average Reference

The common average reference can be computed with the matrix

$$\frac{1}{N}J \quad (3.20)$$

Where  $N$  is the number of electrodes and  $J$  is  $N \times N$  matrix of ones. The product of this matrix with  $s$  computes the average signal and is subtracted from the original signal to yield the CAR version of the signal

$$s_{CAR} = s - \bar{s} = s - \frac{1}{N}Js = \left[ I - \frac{1}{N}J \right] s = Cs \quad (3.21)$$

The covariance of the signals after CAR is then

$$\text{cov}(s_{CAR}) = C \text{cov}(s) C^T \quad (3.22)$$

The effect on the component-based representation is

$$s_{CAR} = Cs = CWz \quad (3.23)$$

It is important to note that this modification of the weight matrix applies to the weight matrix obtained without the change of reference. When CAR is applied to the data the temporal components identified by a whitening algorithm such as PCA are not necessarily



the same.

### **3.3 Results**

#### **3.3.1 Distance-Averaged Correlation**

Human subjects ( $n=2$ ) were implanted with a grid of 56 electrodes with 0.4 mm center-to-center distance referenced to another larger (3 mm diameter) ECoG electrode a few centimeters away, and mice ( $n=2$ ) were implanted with 32-electrode square grids with 0.2 mm or 0.25 mm spacing with a subcutaneous reference near the skull. After removing poor channels and potential artifacts, the signals were bandpass filtered into 6 different bands, and separated into non-overlapping 2.0 second windows (527 windows for subject 1, 326 for subject 2, 1,486 for mouse 1, and 893 for mouse 2). The Pearson correlation coefficient (referred to as simply correlation) was calculated for each window between all pairs of channels on the ECoG grids for each filter. After averaging correlations across equidistant electrode pairs as in Leski et al. (2013) which we will call distance-averaged correlation (DAC), we see that the correlation between pairs of channels decreases on average as the distance between the electrodes increases (Figure 3.1). The values of correlation in Figure 3.1 are averages of correlation calculated in 2 second segments of the data across all segments and channel pairs that share the same spacing. We find similar values to previous studies of the correlation as a function of electrode distance (Kellis et al., 2016; Muller et al., 2016; Bullock et al., 1995). Correlation was analyzed separately for different frequency bands due to the  $1/f$  nature of the signal power, and that the presence of distinct processes present in different bands are common in electrophysiology studies. Also, it is a well-known feature of ECoG that common activity in lower frequencies tends to appear over larger regions than high frequency activity. We find a similar trend in the correlation plots with some exceptions between adjacent

frequency bands, and that between the two commonly used bands in electrophysiology studies, beta (15-30 Hz), and high gamma (70-110+ Hz), the difference is quite large as expected.

The differences between the results in human and mouse is also large (Figure 3.1B inset). In mouse the correlations fall below 0.5 within 1.5 mm while in human even the highest frequencies are correlated above 0.5 up to around 2 mm. The low frequencies in human are noticeably more correlated across distances of a few millimeters. The values within the 2.0 second time windows vary considerably but are concentrated near the mean values (Figure 3.1C,D).

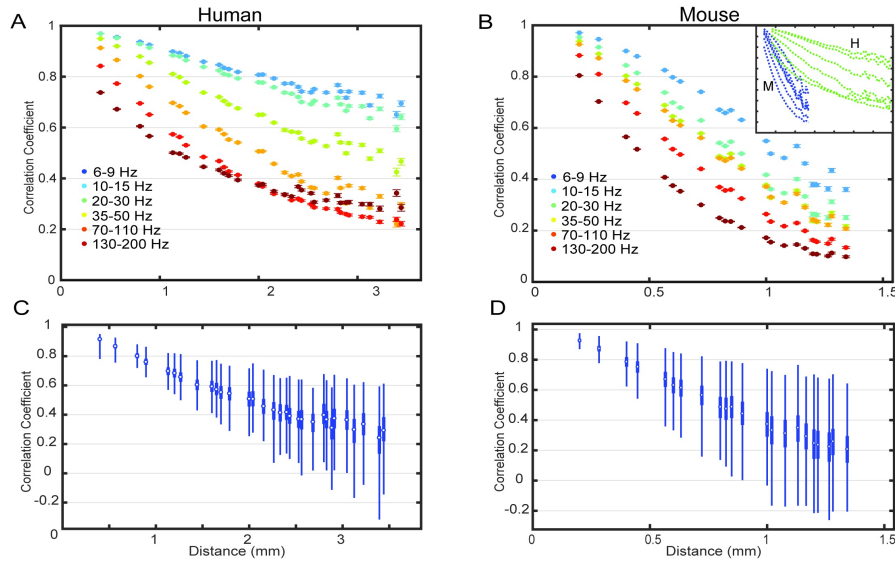


**Figure 3.1.** (A) Results for a human subject 1. Each color represents a frequency band. Error bars are 95% confidence interval of the mean across all time windows and equidistant electrode pairs. (B) DAC for mouse 1. Inset shows (A) and (B) plotted on the same scale for comparison between human (green) and mouse (blue) DAC. (C-D) The distribution across time obtained by averaging only within each window. Boxplot of the distributions of the correlation values over time for one human and one mouse subject in the 35-50 Hz band. The distributions are across all 2.0 s windows with each value the average at each distance of the correlation. Reproduced from Rogers et al. (2019).

### 3.3.2 Component Modeling

Correlation is a measure of to what degree two signals are similar, but an alternative approach to view the similarity is to look for commonality among all the signals simultaneously rather than an aggregate of pair-wise comparisons. There are a few methods which are commonly used in electrophysiology for identifying common signals that are present on multiple channels: principal component analysis (PCA), factor analysis, and independent component analysis (ICA). All are built around the assumption that there exists a set of signals that are present in the data with various amplitudes across all of the channels. ICA and factor analysis were developed to find underlying signals while PCA was not. Factor analysis assumes the components are drawn from a Gaussian distribution (across time samples, not channels), which does not describe the data, especially the sinusoidal signals obtained after bandpass filtering. We used ICA because we expect it to best find the underlying signals, and it is commonly used for this purpose. An important point in using ICA (as well as PCA and FA) is that the geometry of the recordings is not an input to the algorithm. The inputs are a set of time series (in this case) with no particular ordering, arrangement, or any other information relating the channels to one another. Therefore, an orderly spatial arrangement of the ICA results has been taken as an indication of the efficacy of ICA in separating sources, and is compelling in many cases.

To explore the connection between the ICA/PCA decomposition of the data into components and the correlation we start with a model how the spatial extent of the components affects the DAC. Component weights are modeled as two-dimensional Gaussian distributions sampled on a square grid of electrodes. The resulting correlation vs. distance curves are well-approximated by Gaussians, and we find a direct correlation between the width of the component Gaussians and the standard deviation parameter

of the fit of the correlation vs. distance curve as shown in Figure 3.2. The relationship between the two is linear in the limit that there are many components that are sufficiently sampled by the grid of electrodes. The addition of uncorrelated noise to all channels decreases all correlation values by a factor, and the effect of having a reference signal added to every channel is to increase all correlation values. The effect of the noise is more apparent at small distances where even with the Gaussian components, the apparent y-intercept of the DAC drops as noise is added. On the other hand, the reference has the effect of raising the asymptotic value of the DAC for large distances.

We also directly connected the components to the DAC through the weight matrices (mixing matrices in ICA). Applying the ICA unmixing matrix (the inverse of the mixing matrix) to the data will decorrelate the data, and the unmixing matrix can be arbitrarily rescaled, therefore it is always possible for all of the components to have unit variance. This makes the ICA unmixing matrix a whitening, or sphering, matrix which is straightforwardly connected to the covariance matrix of the data because when multiplied by its transpose it must equal the covariance matrix. This allows a reduced, single-component covariance matrix to be calculated for each component of the mixing matrix separately, and the contribution of each component to the DAC can then be calculated.

### **3.3.3 ICA Decomposition of the Recordings**

ICA is applied (using the EEGLab implementation, see Methods) to the same filtered 2 second windows as were used in the DAC calculation. The mixing matrices, when plotted in the arrangement of the electrodes, show readily apparent spatial patterns throughout the recordings as shown in Figure 3.3. As a way to quantify the spatial patterns in the component weights in the mixing matrices, we fit the weights as they are laid out on the brain to a circular two-dimensional Gaussian function. The goodness-of-fit

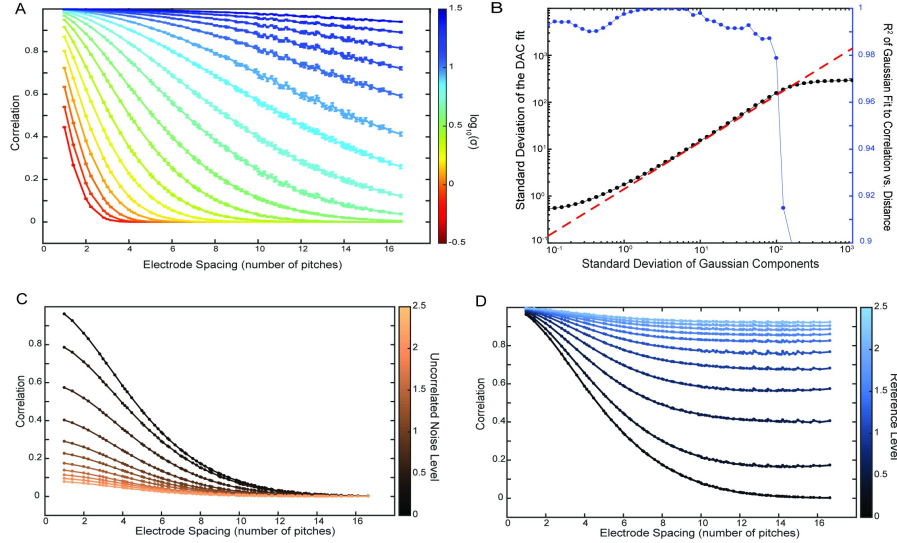


**Figure 3.2.** (A) The DAC curves for different Gaussian standard deviations averaged over 200 iterations of randomly generated components (in arbitrary units) (B) The results of Gaussian fits to the DAC from (A). The black dots are the standard deviation of the fit, and the red dashed line is the theoretical value of square root of 2 larger than the component standard deviation. The R2 values are plotted in blue to indicate where the fit is no longer appropriate. (C,D) The effect on the DAC of adding uncorrelated noise and a reference signal, respectively, to the Gaussian components. Reproduced from Rogers et al. (2019).

gives a rough assessment of the smoothness of the mapped weights and their spatial gradients (see Figure 3.4). Of the parameters of the fit, the one with we expect to have the most relevance to the correlation is the standard deviation, or width, of the Gaussian. Larger widths would correspond to larger correlated areas, and as a result, a higher correlation at larger distances. This effect can be seen when comparing the median width values for each frequency band independently. As shown In Figure 3.5, the median Gaussian width decreases with frequency in agreement with the frequency dependence of the DAC, and that the components tend to be more Gaussian for lower frequencies. At the highest frequencies there is a marked decrease in the goodness of fit that may be due to lower signal-to-noise ratios expected as the  $1/f$  decrease in the signal approaches the noise floor of the hardware.

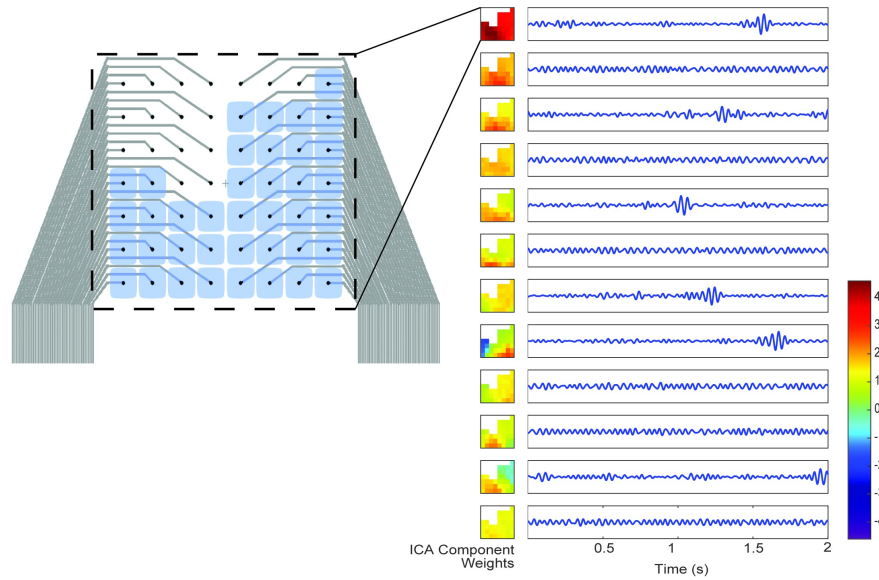


**Figure 3.3.** On the left is an image of the electrode grid with the channels included in the analysis highlighted. An example of the output of ICA for a two second window from a human subject after a bandpass filter between 20 and 30 Hz. The left column is the weights associated with each component for the first 12 of 30 components plotted in the arrangement of the electrodes on the device. The right column are the components, or time series identified by ICA after normalizing to have variance of 1. The maps must be scaled inversely, and the overall amplitude of the component can be seen in the magnitude of the weights. Reproduced from Rogers et al. (2019).

By comparing the contributions of each ICA component to its Gaussian fit we find if and how the DAC curves are influenced by the spatial distribution of the component weights. The spatial distribution of the weights must explain the DAC curves, but to determine whether the Gaussian fits have any significance for the DAC in real data, the contribution of the components is plotted as a function of the  $R^2$  values of their fits in Figure 3.6. The higher  $R^2$  components account for a disproportionately large amount of the drop in the DAC with distance, and therefore the particular shape of the DAC is mostly attributable to the more Gaussian components. The correlation and variance are concentrated in more Gaussian components which shows that the larger, more significant components are generally roughly Gaussian (Supplement Fig 1).

As a control, PCA is substituted for ICA, and because it can also be rescaled into

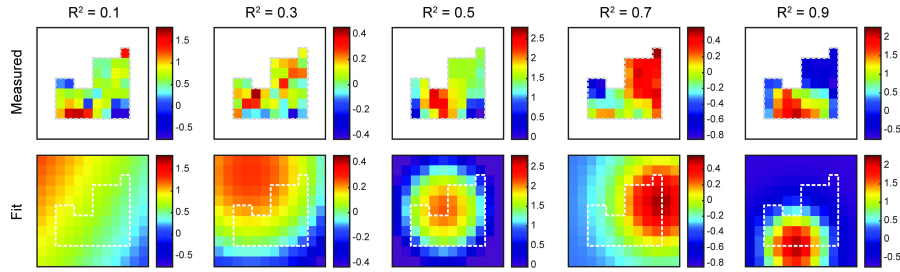


**Figure 3.4.** Examples of components with various  $R^2$  values (top), and their corresponding least-squares circular Gaussian fits (bottom). Reproduced from Rogers et al. (2019).

a whitening matrix, all of the analyses can be carried out in the same manner for PCA as for ICA. PCA is not a source separation algorithm like ICA, but in the case where there are sources that account for most of the variation these sources will show up in the first principal components. This can be seen in the  $R^2$  histograms in where the components are concentrated near 0, but there is also a smaller number of components very near 1.0 that account for much of the variance. These are the first few PCA components which are larger and more Gaussian. These more spatially Gaussian principal components account for much of the drop in correlation, so using PCA for comparison both shows the effectiveness of ICA in finding local sources, and that again, the more Gaussian components are more strongly tied to the drop in the DAC with distance.

The location of the reference electrode can have a large impact on the correlation values as shown in Fig 2D (Nunez et al., 1997; Fein et al., 1988; Zaveri et al., 2000; Hu et al., 2010). The reference electrode subtracts the same signal from all of the recording channels and this will act to increase the correlation between any two channels if the reference is sufficiently uncorrelated with the signals. In mouse the reference electrode was placed subcutaneously and not on the skull, while in human the reference was multiple contacts within 10 cm of the of the micro-ECOG grid on the cortical surface. The latter are more likely to be active at the frequencies of interest, and even correlated

with the unipolar signals measured at the grid. The reference electrode placement should always be taken into account when interpreting correlation or other measures of signal similarity, and that the relatively close reference used in the human subjects is not an ideal placement for studying DAC. Consequently, the DAC curves we obtained in Figure 3.1 should not be interpreted as the DAC corresponding to unipolar potentials (potentials measured against a theoretical reference potential of zero) which would be the ideal for studying spatial correlation across the brain. Using the methods in Hu et al. (2007) we attempted to identify the reference signal in the human recordings, but a signal that matched the criteria was not found. Additionally, the reference will ideally be identified by ICA as a component with the same weight on every channel across the grid. In practice this is unlikely, but it may be identified in part and represented by components with relatively flat weights. In fact, this method was used in Whitmore and Lin (2016). In our case it may be correlated with the unipolar surface potentials at the grid and could be mixed in with components of those.

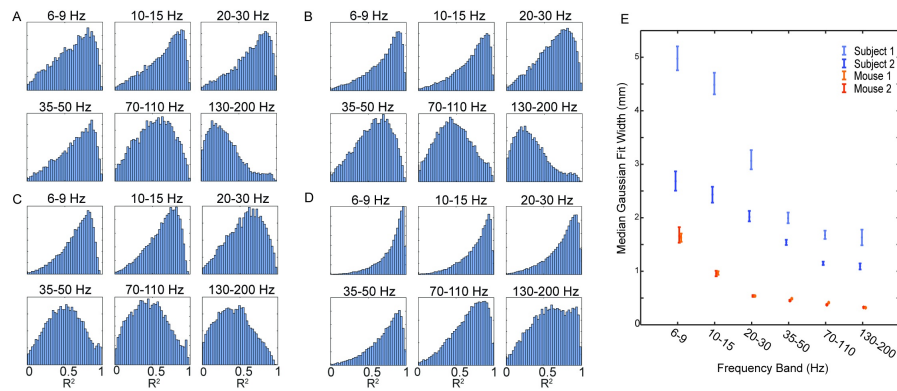


**Figure 3.5.** The histograms are calculated separately for each subject and each frequency band across all 2.0 s windows. (A-B)  $R^2$  for two human subjects. (C-D)  $R^2$  for two mice. (E) The median width parameter of the Gaussian function for fits with  $R^2$  greater than 0.7 for all 4 subjects as a function of frequency band. The error bars are 95% confidence intervals obtained by a bootstrap analysis. Reproduced from Rogers et al. (2019).

A common method in ECoG to remove the true reference is to use the common



average reference (CAR), at the expense of introducing a virtual reference which is also unknown. When ICA is applied after CAR, and fits are recalculated the distribution of  $R^2$  values is nearly unchanged. While the mean Gaussian widths are significantly different after CAR (two-sample Kolmogorov-Smirnov test  $p > 0.05$ ), they follow the unreferenced values closely but are slightly larger (19 +/- 9 %). This shows that the references that were used did not have a large effect on the components and their spatial properties. The large difference between the original and CAR correlations can be understood through the effect of the CAR matrix discussed in the Methods. The amount subtracted from each component is uniform across all the channels and is equal to the average weight. Therefore, the shapes of the components are unchanged, but they are shifted such that they mean weight of each component across channels is zero. Reference effects are removed in this way due to their representation as a uniform component across all channels. This shifting of the weights can be seen in the data through the offset term of the Gaussian fit becoming strictly negative after CAR.

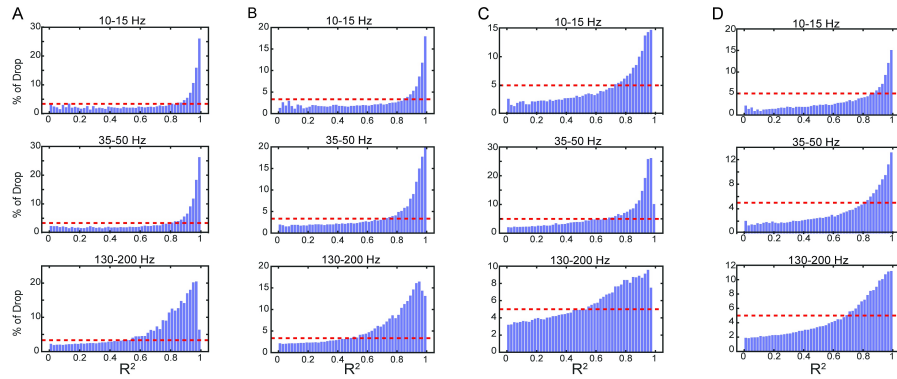


**Figure 3.6.** The percentage of the DAC drop explained by each component is averaged across components with similar (binned)  $R^2$  values. Therefore, each bar represents the average percentage of the DAC drop explained by components as a function of their values of  $R^2$ , and are shown for 3 different frequencies and for each subject (A-D) as in Figure 4. The dashed red line represents the percentage that would be explained by each component if all components contributed equally. Reproduced from Rogers et al. (2019).

### 3.3.4 Localized Response Modeling

In Hermiz et al. (2018) modeling and experimental analyses were performed to determine if and when higher density grids outperform lower density grids. An illustrative model was developed to determine under what conditions a higher density grid might outperform a lower density grid. Analytical results for the simple 2-channel case and numerical results for higher dimensional cases are presented (Fig 3.8).

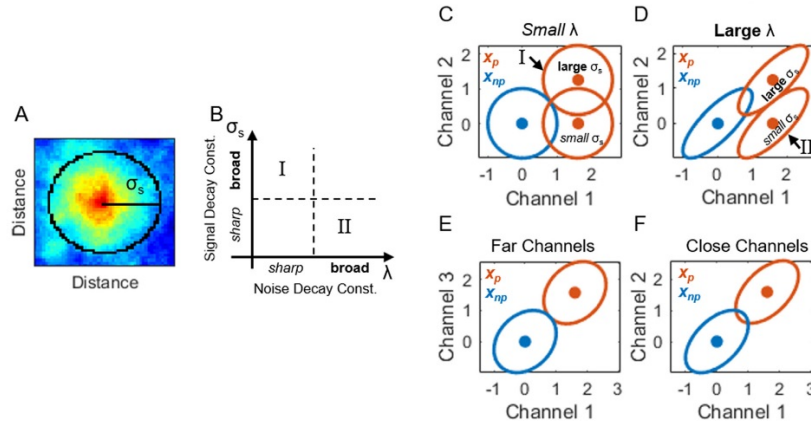


**Figure 3.7.** (A) Spatial representation of signal fall-off length  $s$  (arbitrary units) using generated data from the model. Note, that dark red maps to the maximum value and dark blue maps to the minimum value. For more visualizations of signal and noise fall-off length,  $\lambda$  see Fig S1 (B) Illustration of which regions in the parameter space  $\sigma_s$ - $\lambda$  where higher density grids outperform lower density grids. There are two regions: I,  $\sigma_s$  is large and  $\lambda$  is small or II,  $\sigma_s$  is small and  $\lambda$  is large. (C-F) 2-channel feature space where the MVN for various random variables are plotted - dots are means and the ellipses are 1 standard deviation. The distribution of channel measurements from the non-preferred stimulus,  $x_{np}$  are blue and the distribution from the preferred stimulus,  $x_p$  are red. (C) Illustrates effect I: given a small  $\lambda$ , a larger  $\sigma_s$  will increase separation between  $x_p$  and  $x_{np}$ . Note small  $\lambda$  corresponds to little correlation and thus a circular distribution. (D) Illustrates effect II: given a large  $\lambda$ , a smaller  $\sigma_s$  will increase separation. Note large  $\lambda$  corresponds to large correlation and thus a skewed distribution along the y axis. (E-F) Illustrates when 2 channels spaced far apart (low density) can be better than when spaced close together (high density). In this case,  $\sigma_s$  must be large and  $\lambda$  must be relatively small. Reproduced from Hermiz et al. (2018).

We developed a simple model that assumes measurements belong two types of stimuli, preferred,  $x_p$  and non-preferred,  $x_{np}$  and are generated from multivariate normal

(MVN) distributions:  $x_p = (s, \Sigma)$  and  $x_{np} = N(0, \Sigma)$ . The signal of interest,  $s$  is assumed to peak at a specific electrode,  $x_{ctr}$  and fall off exponentially with a characteristic length,  $\sigma_s$ . In all analyses, the electrode  $x_{ctr}$  is a member of all grids and is the center most electrode. When there is an even number of electrodes, then  $x_{ctr}$  is the left center most electrode. Please note that in these simulations, the peak location of the signal is not modeled as randomly related to electrode location, as would be the case in actual recordings. Had our model permitted response peaks between electrodes, then tight electrode spacing would be highly advantageous, inasmuch as it would make it more likely that the response peak would be directly measured. However, for our current purpose, we only focus on the case where the peak activation is centered on the grid. Noise correlation is also modeled as a decaying exponential with characteristic length,  $\lambda$ . That is, electrodes closer together will have more correlations whereas channels farther apart will have less. Here, noise can be interpreted as spontaneous neural activity that is independent of the stimulus.

We used the model to find parameters for which the higher density grids would outperform the lower density grids. Details can be found in Hermiz et al. (2018), but the results for 3x3 grids with different spacing which is the simplest case for testing the effect of density are shown in Fig 3.8.

### 3.4 Discussion

The results of our study indicate high degree of variability of the DAC, both within any set of data, as Figure 1 shows, and between datasets due to external factors such as where on the cortex the electrodes are placed. There is large variation across the 2.0 second windows as shown in Figure 3.1, that may reflect changes in ongoing activity. In fact, it has been shown that there are task-related changes in the DAC (Leopold et al., 2003; Muller et al., 2016; Manganotti et al., 1998), however we did not find there to be task- or state-related changes in the DAC in the human recordings.

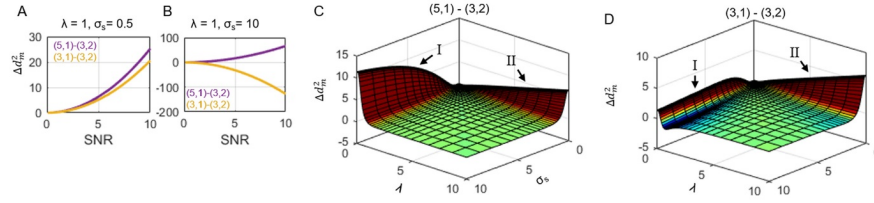


**Figure 3.8.** (A-D) Numerical results from (5,1) vs (3,2) and (3,1) vs (3,2). The notation (a,b) refers to a grid that has a by b channels and has a pitch of b. (A-B) As SNR increases, the difference of squared Mahalanobis distance ( $\Delta d_m^2$ ) increases or decreases, depending on  $\sigma_s$ ,  $\lambda$  and which grids are compared. (C-D) 3d plots showing  $\Delta d_m^2$  for a grid of sand  $\lambda$  values. (C) For (5,1) - (3,2), there are no values for which  $\Delta d_m^2 < 0$ , given the domain; and as expected,  $\Delta d_m^2 \gg 0$ , when  $\sigma_s$  is large and  $\lambda$  is small or vice versa. (D) For (3,1) - (3,2),  $\Delta d_m^2 < 0$ , when roughly,  $\sigma_s > 5$  and  $1 < \lambda < 2$ , which is expected. Again,  $\Delta d_m^2 \gg 0$  when  $\sigma_s$  is large and  $\lambda$  is small or vice versa. The color axis ranges from -1 (dark blue) to 1 (dark red) and is used to represent sign. Reproduced from Hermiz et al. (2018).

The particular curve of the DAC may change between time windows, recording epochs, subjects, and species, but a robust feature in our recordings and previous studies is the frequency dependence of the spatial correlation. This agrees with past studies that the responses in lower frequency bands are more spread out than in higher bands (Leopold et al., 2003; Takaura et al., 2016; Łeski et al., 2013; Maier et al., 2010; Miller et al., 2007) and is evident in similar studies that used coherence instead of correlation, which is an inherently frequency dependent similarity metric. The coherence is plotted as a function of frequency, and in for ECoG data almost completely monotonically decreases with frequency (Leopold et al., 2003; Kellis et al., 2016; Muller et al., 2016).

The geometry of the ICA component weights offers a possible explanation of this frequency dependence. Two ways by which neighboring electrodes can be correlated are by volume conduction and coactivation of populations close to each electrode which produce distinct, but correlated potentials (Dubey and Ray, 2016; Parabucki and Lampl, 2017). In many cases there is a degree of both which contributes to the correlation, but for large distances where volume conduction is assumed to be negligible the presence of

correlation is used as an indication of connectivity (Casimo et al., 2016). On the other hand, at the sub-millimeter scale we expect volume conduction may play a larger role. The presence of a single-peaked, radially symmetric, and smooth ICA weights map is consistent with volume conduction of the potentials, and the Gaussian fits show that many of the components fit this description. Coactivating regions could also be described by this shape but are not limited to it; there could be distinct, separated peaks, plateaus, or checkerboard-patterned regions.

The large and consistent difference in the DAC between human and mouse can also be explained by either larger coactivated areas of cortex or a larger effect of volume conduction in human cortex. The spread of a signal due to volume conduction in brain tissue would be the same in either species assuming they have similar conductivities, but human cortex has neurons with larger lateral spread of their dendritic and axonal trees and is roughly twice as thick as mouse cortex. The effect of volume conduction on deeper sources will spread the potentials they cause more widely across the cortical surface. Additionally, the size of functionally distinct cortical regions is larger in humans, and we are again left with the ambiguity between the two possible factors: the size of the correlated activity, and its spatial spread as in Łeski et al. (2013).

In our analysis the choice of ICA as the particular form of whitening and 2 dimensional Gaussians as the function used for fitting are not the only choices that could have been used, but they were chosen for simplicity and applicability to this analysis. As a fitting function, a 2-dimensional Gaussian was chosen for its simplicity and flexibility, and not due to any assumption that the components would take this particular form. The purpose of the fit is to identify smoothly varying component weights. The function is smooth on a small scale, with the only peak being the center, so that neighbor-to-neighbor oscillations in the weights will degrade the fit. It is also able to describe radially symmetric peaked distributions as well as flat linear gradients by being fit to a very

wide Gaussian with its center far from the electrode grid. Alternatives more tailored to quantify the smoothness could be used such as taking the second spatial derivative of the component weights and finding smooth gradients and peaks by taking first spatial derivatives. These are harder to implement and interpret, and the high  $R^2$  values when using ICA and low ones from PCA show the fitting approach is able to describe the components while not being so flexible that it can be fit to any component weights.

Another reason for using the Gaussian fits is that they provide a single parameter that characterizes the size of the regions that contain the components. The mean width of the fits of each frequency band decreases with increasing frequency, and this may be due to the effect that frequency has on the spatial spread of LFP. Additionally, the fits provide another method of removing distant volume conducted activity similar to the ICA approach used in Whitmore and Lin (2016) by using both the center location of the Gaussian along with the width to identify components of the signals that are far from the grid location. This kind of ICA-based method as an alternative to standard re-referencing schemes has been proposed in Michelmann et al. (2018).

On the other hand, the DAC curves are not fit to Gaussians for the data despite the modeling results that showed that Gaussian components have Gaussian DACs. We expect that using the same model, but with other peaked, but not necessarily radially symmetric distributions, will still result in monotonically decreasing DAC curves with a different shape. Additionally, the effect of noise and reference will add a predictable modification to the curve but adds additional unknown parameters. These may be estimated but this is confounded by the unknown effect of the actual non-Gaussian shape of the components, and the fit becomes more difficult to implement and interpret.

The component mixing matrix weights analysis requires any whitening matrix to separate the components, but ICA was chosen for this purpose. Commonly used whitening transformations are not intended to perform source separation, but ICA can be

both a whitening and a blind source separation algorithm. PCA and factor analysis have been used for finding common sources in the data, but the assumptions about the data of ICA are more well suited to finding sources in electrophysiology, hence its popularity. Factor analysis is designed to find similar localized sources but is not easily modified to be a whitening transformation and its assumption of normally distributed components is incompatible with the sinusoidal nature of narrow bandpass filtered signals.

There are drawbacks to calculating ICA in separate frequency bands, as any broadband processes or ones that span frequency ranges between or across multiple bands will not be as accurately identified or be recognized as part of the same component. Still, ICA was calculated by frequency band so as to be calculated on the exact same windows and signals as the correlation, and due to the  $1/f$  power spectrum typical of electrophysiology. The first consideration is necessary specifically for linking the correlation and the component mixing matrix through the covariance matrix, while the second is a general problem in applying ICA to LFP. ICA may less accurately separate sources whose power is concentrated in higher frequencies due to the much larger power present in lower frequencies biasing ICA towards identifying sources concentrated in those. In addition, if PCA is applied as a pre-processing step, the components that contain some high frequency sources may even be discarded.

ICA was applied only to small time windows in addition to narrow frequency bands. This has similar drawbacks in terms of the effectiveness of ICA because it limits the number of observations which ICA can use to identify source. For the same reason as before, consistency with the segments analyzed for correlation, the 2 second windows are needed. Also, this length of time may be appropriate because the components were found to vary even between adjacent windows. However, there is some consistency in the ICA mixing matrices across time – that is very similar components show up repeatedly, but not consistently. This suggests that the time scale of the duration of stable components may

be 2 seconds or less, and perhaps ICA would be better suited to even shorter windows for this data in future work to avoid temporal fluctuations in source strengths which does not fit the assumption in ICA of time-invariant mixing matrices.

The curve generated by averaging the correlation over many contacts offers some guidance as to how the signals will be related for a given electrode spacing, but it is more straightforward to choose a spacing when given a measure of the spatial extent of the activity. The two are linked, and as has been shown previously with the correlation, the frequency has a strong effect on the spread of potentials measured at the surface of the brain. Electrodes spaced less than a millimeter apart are more suited to higher frequencies or to smaller animals than humans, but even with very limited cortical coverage volume conduction still allows activity that is not directly under the grid to be recorded.

Chapter 3 is a reprint of the material as it appears in Correlation Structure in Micro-ECoG Recordings is Described by Spatially Coherent Components in PLoS Computational Biology, 2019. Rogers, Nicholas; Hermiz, John; Ganji, Mehran; Kaestner, Erik; Kılıç, Kivılcım ; Hossain, Lorraine; Thunemann, Martin; Cleary, Daniel R; Carter, Bob S; Barba, David; Devor, Anna; Halgren, Eric; Dayeh, Shadi A; Gilja, Vikash. The dissertation author was the primary investigator and author of this material.

Chapter 3, in part, is a reprint of the material as it appears in Sub-Millimeter ECoG Pitch In Human Enables Higher Fidelity Cognitive Neural State Estimation in NeuroImage, 2018. Hermiz, John; Rogers, Nicholas; Kaestner, Erik; Ganji, Mehran; Cleary, Daniel R; Carter, Bob S; Barba, David; Dayeh, Shadi A; Halgren, Eric; Gilja, Vikash. The dissertation author was a co-investigator and co-author of this paper.



## Chapter 4

# Volume Conduction in Electrophysiology

### 4.1 The Brain as a Volume Conductor

Potentials generated by the brain can be recorded without probes inside the cellular membrane due to brain and surrounding tissues being electrically conductive. Changes in membrane potentials are detected as extracellular potentials when ions flow across the membrane such as during an action potential.

#### 4.1.1 Static Conductivity and Permittivity

The properties considered in this section are macroscopic properties of the tissues. They are measured by directly by electrodes that are much larger than the cellular structures in the brain that contribute on the microscopic scale to the conductivity and permittivity. For the purposes of electrophysiology well above cellular scale these empirically determined bulk properties will be the relevant ones to consider.

The brain is assumed to be Ohmic, that is it has a linear relationship between the electric field and the current. In circuits this is represented by the familiar  $I = V/R$ . In the bulk of a conductive material the currents are instead current densities,  $\mathbf{J}$ , a vector quantity representing the flow of charges at a point in space. In a region the current

density is a vector field like the electric field. In this form Ohm's law is given by

$$\mathbf{J} = \sigma \mathbf{E}$$

In an anisotropic medium  $\sigma$  is represented by a tensor, but in an isotropic medium it is a scalar.

The conductivity in gray matter is around 0.2-0.4 S/m. In general the conductivity of a material is frequency-dependent, and becomes interrelated with the permittivity.

The polarization due to external electric fields in brain tissue can also be considered linear medium for fields generated by biological phenomena. For most biological tissue the magnetic permeability is effectively equal to the magnetic permeability of free space  $\mu_0$ . On the other hand, the permittivity can be several orders of magnitude larger than the permittivity of free space, and is estimated to be around  $10^7$  or  $10^8$  times larger than that of free space.

#### **4.1.2 Time/Frequency Dependence**

When a time-varying external field is applied to a material it will generate currents and cause polarization within the material. The polarization will cancel part of the external field, described by the susceptibility and permittivity, and in the case of sinusoidal fields will be the result of sinusoidal motion of charges within the material. This also describes the conductivity in the presence of sinusoidal fields. In the frequency domain these relationships are described by

$$\mathbf{D}(\omega) = \varepsilon(\omega) \mathbf{E}(\omega)$$

$$\mathbf{J}(\omega) = \sigma(\omega) \mathbf{E}(\omega)$$

These expressions may describe two separate phenomena: the polarization of charges that are confined and the motion (or resistance to motion) of mobile charge carriers. With both viewed as currents,

$$\mathbf{J}(\omega) = \mathbf{J}_m(\omega) + \mathbf{J}_p(\omega) = \sigma(\omega)\mathbf{E}(\omega) + i\omega\epsilon(\omega)\mathbf{E}(\omega)$$

where the total current is the sum of the motions of the mobile and polarized charges. In biological tissue, the distinction between the two classes of charges is not so clear, and in practice, measurement of the tissue may not distinguish between the two effects. They are often combined into one quantity

$$\mathbf{J} = (\sigma + i\omega\epsilon)\mathbf{E} = i\omega\epsilon^*\mathbf{E} = \sigma^*\mathbf{E}$$

that can either be described by the complex permittivity or complex conductivity, which are different representations of the same phenomenon, and are related by

$$\sigma^*(\omega) = i\omega\epsilon^*(\omega)$$

So long as they remain in the linear regime, either of these completely describe the response of the system to external charges and fields, but it must be remembered that  $\sigma^*$  represents any current flow including bound charges and  $\epsilon^*$  no longer represents only the polarization of those bound charges. It is customary that the terms "conductivity" and "permittivity" refer to the real part of the respective complex quantity.

The brain, like many biological tissues, has dielectric properties of a solution of ions as charge carriers surrounded by/surrounding many cells. The static conductivity of most kinds of tissue is relatively low, about an order of magnitude smaller than that of sea water ( $\sim 5$  S/m). The permittivity is characterized by very large values at low

frequencies that quickly decrease at higher frequencies.

Although there is not a strong consensus about the values of the complex dielectric constant in the brain, there is some understanding of the processes in biological tissue that generate the shape of the measured values. The permittivity (not complex) is the result of multiple relaxation processes, and these result in the characteristic shape of the permittivity. At the time scales of interest for electrophysiological recording the dominant effect is believed to be counterion polarization which is the diffusion of ions at the double layers formed at cell membranes or any other insulating boundary as the field changes back and forth.

It is common to describe the complex permittivity with an expression of the form

$$\epsilon^*(\omega) = \epsilon_\infty + \frac{\sigma_{dc}}{i\omega} + \sum_n \frac{A_n}{1 + (i\omega\tau_n)^{1-\alpha_n}}$$

where each term in the sum is a relaxation described by a time constant  $\tau_n$ , and the first two terms are the permittivity at frequencies above the fastest relaxation and the static conductivity. The form of the relaxation above is the Cole-Cole equation, and reduces to Debye relaxation when  $\alpha$  is zero.

Data for gray matter are shown in Figure 1, and the authors subsequently fit the data to the form above with their fit parameters given in Table 4.1 and plotted in Fig 4.1.

$\epsilon_\infty$	$\sigma_{dc}$	$A_1$	$\tau_1$ (ms)	$\alpha_1$	$A_2$	$\tau_2$ ( $\mu$ s)	$\alpha_2$
4.0	0.02	$4.5 \times 10^7$	5.3	0.0	$2 \times 10^5$	106	0.22
		$A_3$	$\tau_3$ (ns)	$\alpha_3$	$A_4$	$\tau_4$ (ps)	$\alpha_4$
		400	8	0.15	45	8	0.1

**Table 4.1.** Cole-Cole fit parameters from Gabriel et al. (1996)

The first term in the sum will account for most of the time-dependent effects observed in electrophysiological recordings. Based purely on the slowest time constant of 5 ms, it would be expected that events on time scales in the millisecond range begin

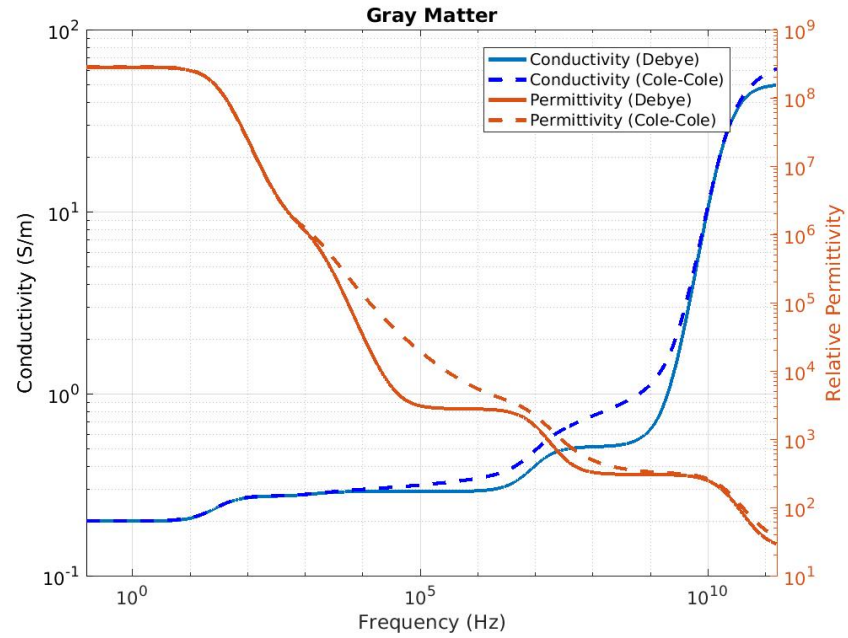


**Figure 4.1.** Conductivity and permittivity of excised gray matter. Parameters from from Gabriel et al. (1996).

to experience time delays, but slower signals will be effectively unchanged in time, and faster signals will experience significant distortion.

## 4.2 Current Sources and their Potentials

### 4.2.1 New

Current source density is based on the assumption of the brain as a volume conductor, a linear Ohmic medium with conductivity  $\sigma$

$$\mathbf{J}_f = \sigma \mathbf{E}$$

However, it is simpler to include the effect of the conductivity through the complex permittivity. In a linear isotropic medium we have Maxwell's equation in the Lorenz

gauge in the form

$$\begin{aligned} -\nabla^2 \phi + \mu \epsilon^* \frac{\partial^2 \phi}{\partial t^2} &= \frac{\rho_f}{\epsilon^*} \\ -\nabla^2 \mathbf{A} + \mu \epsilon^* \frac{\partial^2 \mathbf{A}}{\partial t^2} &= \mu \mathbf{J}_f \end{aligned}$$

It is important to note that by using the complex permittivity the free currents do not include the induced volume conduction currents as those are now considered bound charges/currents. With the tissue properties given in the last section and at the frequencies of interest (less than 10 kHz) the time derivatives become negligible. In electrophysiology we are interested in the potential with solution given by

$$-\epsilon^* \nabla^2 \phi = -\left(\epsilon + \frac{\sigma}{i\omega}\right) \nabla^2 \phi = \rho_f \quad (4.1)$$

which reproduces the standard form of the solution from CSD when the capacitive permittivity term can be neglected and the transmembrane currents are represented as sources and sinks of charge density.

$$-\sigma \nabla^2 \phi = i\omega \rho_f = \frac{\partial \rho_f}{\partial t} = I_t$$

For separable sources the solutions for the potential are also separable in Eq. 4.1. Therefore the Laplacian equation in space is unchanged and given the large permittivity values at low frequencies the permittivity term should not be neglected in all cases. Identical to Eq. 4.1 but in more familiar form then the general equation for the potential is

$$-\sigma^* \nabla^2 \phi = I_t \quad (4.2)$$

For the purpose of recording FP the frequencies of interest only range up to about 500 Hz. The frequency dependent effects of the complex conductivity can be summarized

in a Bode plot (Fig 4.2) of the transfer function  $1/\sigma^*$  applied to the temporal component of the transmembrane currents. So long as the the gain and phase do not vary significantly over the range of frequencies of interest the temporal effect will be negligible. There is some distortion that will be caused around 100 Hz shown by the dip in the phase, but this will result in a minor distortion of the wave form of the FP.

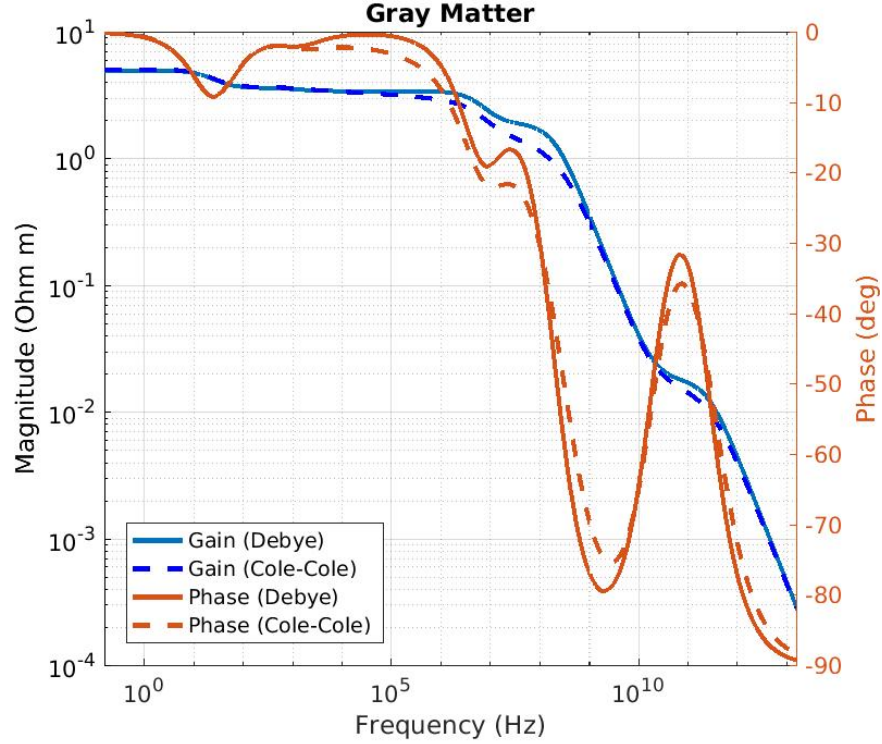


**Figure 4.2.** Bode plot of the transfer function of the complex conductivity of gray matter. Parameters from from Gabriel et al. (1996).

#### 4.2.2 Solutions near the Cortical Surface - ECoG Model

To simplify the geometry involved we will treat the cortical surface as having no curvature, and that the cortex is uniform, isotropic, and extends infinitely far down. We set  $z = 0$  at the cortical surface, and assume there is a conductive medium with uniform thickness above the cortical surface. We assume that above the 2nd medium is a perfect

insulator which approximates air in recordings where the cortex is exposed.

$$\sigma = \sigma_1, \quad z < 0$$

$$\sigma = \sigma_2, \quad 0 < z < T$$

$$\sigma = 0, \quad z > T$$

We wish to find the solution to a point source inside the cortex at a depth  $D$ . The potential in each region is a solution to

$$\nabla^2 V_1 = -\frac{1}{\sigma_1} \delta(x) \delta(y) \delta(z + D), \quad z < 0$$

$$\nabla^2 V_2 = 0, \quad 0 < z < T$$

$$V_3 = 0, \quad z > T$$

The horizontal extent of the medium is considered infinite, and at the potential should go to zero for locations distant from the origin. The potential must have no discontinuities, and therefore must match at the boundaries. Charge conservation relates the normal derivatives of the potentials at the boundaries.

$$V(r \rightarrow \infty) = 0$$

$$V_1(z = 0) = V_2(z = 0)$$

$$V_2(z = T) = V_3(z = T) = 0$$



$$\begin{aligned}\sigma_1 \frac{\partial V_1}{\partial z}(z=0) &= \sigma_2 \frac{\partial V_2}{\partial z}(z=0) \\ \frac{\partial V_2}{\partial z}(z=T) &= 0\end{aligned}$$

We choose to use cylindrical coordinates due to the radial symmetry present in the source distribution, and the planar boundary conditions along the  $z$  axis. Using separation of variables, the solutions to Laplace's equation in cylindrical coordinates are given by linear combinations of the products of Bessel functions of  $r$ , and exponential or sinusoid functions of  $z$ . Symmetry of the source restricts the solutions to having no angular dependence, and significantly simplifies the general form of the solution by only allowing Bessel functions of order 0. In both media the boundary conditions require that the potential is finite everywhere and approaches 0 for large distances. Therefore the radial component of the complementary solutions can only be Bessel functions of the first kind with order 0,  $J_0$ . The particular solution for  $V_1$  is the sum of the well-known solution to Laplace's equation for a delta function and the complementary solution.

$$V_1 = \frac{1}{4\pi\sigma_1\sqrt{r^2+(z+D)^2}} + \int_0^\infty \left[ A_1(k)e^{kz} + B_1(k)e^{-kz} \right] J_0(kr) dk$$

The general solution above will satisfy Laplace's equation everywhere except at the point source, where it will equal the delta function source. The boundary conditions can be satisfied by finding the appropriate  $A_1(k)$ , and  $B_2$  must be zero for the solution to remain finite as  $z \rightarrow -\infty$ . In the 2nd medium there are no sources, and the solutions are the homogeneous solutions, as above.

$$V_2 = \int_0^\infty \left[ A_2(k)e^{kz} + B_2(k)e^{-kz} \right] J_0(kr) dk$$

The condition at the top,  $z = T$ , that  $V_2 = 0$ , requires that  $B_2(k) = e^{2kT} A_2(k)$ . The

boundary conditions at  $z = 0$  combined with the identities

$$\begin{aligned}\int_0^\infty J_0(kr)J_0(k'r)rdr &= \frac{1}{k}\delta(k-k') \\ \int_0^\infty (r^2+x^2)^{-1/2}J_0(kr)rdr &= \frac{e^{-kx}}{k} \\ \int_0^\infty (r^2+x^2)^{-3/2}J_0(kr)rdr &= e^{-kx}\end{aligned}$$

determine the potentials, and results in solutions for the coefficients as

$$\begin{aligned}A_1(k) &= \frac{\sigma_1(1+e^{2kT}) + \sigma_2(1-e^{2kT})}{\sigma_1(1+e^{2kT}) - \sigma_2(1-e^{2kT})}e^{-kD} \\ A_2(k) &= \frac{2\sigma_1}{\sigma_1(1+e^{2kT}) - \sigma_2(1-e^{2kT})}e^{-kD} \\ B_2(k) &= \frac{2\sigma_1e^{2kT}}{\sigma_1(1+e^{2kT}) - \sigma_2(1-e^{2kT})}e^{-kD}\end{aligned}$$

The integrals that make up the solutions can be evaluated using

$$\int_0^\infty e^{-kx}e^{\pm kz}J_0(kr)dk = \frac{1}{\sqrt{r^2+(z\mp x)^2}}.$$

The coefficients can be written as sums using the series

$$\frac{1}{x+c} = \sum_{n=0}^{\infty} (-1)^n c^{1-n} x^n \quad \text{for } |x| < |c|.$$

By breaking the the integrals into sums and evaluating them we obtain a much simpler

form for the potentials.

$$V_1(r, z, \phi) = \frac{1}{4\pi\sigma_1} \left[ \frac{1}{\sqrt{r^2 + (z + D)^2}} + \frac{\alpha}{\sqrt{r^2 + (z - D)^2}} + \sum_{n=0}^{\infty} (-\alpha)^n \frac{1 - \alpha^2}{\sqrt{r^2 + (z - D - 2(n + 1)T)^2}} \right] \quad (4.3)$$

$$V_2(r, z, \phi) = \frac{1}{4\pi\sigma_1} \sum_{n=0}^{\infty} (-\alpha)^n (1 + \alpha) \left[ \frac{1}{\sqrt{r^2 + (z + D + 2nT)^2}} + \frac{1}{\sqrt{r^2 + (z - D - 2(n + 1)T)^2}} \right] \quad (4.4)$$

The constant  $\alpha$  reflects the relative conductivity difference between the two media.

$$\alpha = \frac{\sigma_1 - \sigma_2}{\sigma_1 + \sigma_2}$$

The form of the solution of that of using the method of images with an infinite number of images charge due to the presence of 3 layers.

## **Chapter 5**

# **Implications of Boundary Effects for ECoG Array Design**

### **5.1 Introduction**

Electrical activity of the brain is measured using various modalities such as electroencephalography (EEG), electrocorticography (ECoG), and penetrating electrodes all of which have characteristics determined largely by the relative location of the electrodes to the various tissues of the head. Electrodes inserted into the brain can record the activity of individual neurons, while the spatial resolution of EEG is severely reduced by the volume conduction of the potentials through the cerebrospinal fluid (CSF), skull, and scalp. Correspondingly, it is an often-used approximation in intracortical electrophysiology to ignore tissue boundaries and to assume the medium is of infinite extent and homogeneous (Mitzdorf, 1985; Tenke and Kayser, 2012). However, when modeling EEG, the CSF layer, skull, and scalp must be included and the way geometry of the tissue and electrodes has a large effect on the recordings or models (Vorwerk et al., 2014; Tenke and Kayser, 2012; Rice et al., 2013).

Despite the electric potentials measured by the electrodes not being conducted through the skull, intracranial electrophysiology is subject to the effects of many tissue boundaries and properties. This has motivated studies on the effect of electrical potentials

caused by tissue properties (Brodnick et al., 2019; Rice et al., 2013; Goto et al., 2010; Slutzky et al., 2010; Einevoll et al., 2007; Pettersen et al., 2006), the presence of the electrode and its effect on the surrounding tissue (Ollikainen et al., 2000; Blanche et al., 2005; Moffitt and McIntyre, 2005), or a combination of both effects (Hill et al., 2018; Ness et al., 2015; von Ellenrieder et al., 2012; Zhang et al., 2006). The scale of the effects ranges from changes local to the electrode that alter the amplitude of single action potentials to whole-head EEG models altered by the presence of an insulating, subdurally implanted ECoG grid, and often the geometry is complex enough to entail use of finite-element methods (FEM) in order to obtain solutions.

The modality of electrophysiology perhaps most able to both control and benefit from its own effect on the potentials is electrocorticography (ECoG). The materials and geometry of the ECoG device determine the boundary conditions at the brain surface and this allows the devices to be designed in such a way to modify the signals that are recorded. The effect of the design and placement of ECoG electrodes on recorded action potentials was characterized in (Hill et al., 2018). The effect on ECoG is also two-fold in that in addition to altering the boundary, the potentials are recorded on the boundary which is the location where they are most affected by its presence. This broader effect can be seen from predicted changes in EEG in Zhang et al. (2006) and ECoG Ness et al. (2015) as well as when the boundary conditions changes are caused by the presence of an ECoG array (Pettersen et al., 2006; Einevoll et al., 2007). We propose a planar model with three layers to allow for an intervening layer between the electrodes and the brain tissue with the goal of applying it to predict the effects of various intracranial electrode and experimental designs. The region of interest is small enough when using relatively shallow laminar electrodes or micro-ECoG arrays to allow us to create an analytically tractable model by assuming that the curvature of the brain surface can be neglected and that the lateral extent of the exposed cortex is large enough to avoid lateral edge effects.

In addition, we performed experiments to measure the predicted effect by implanting a laminar electrode array into the whisker barrel cortex of anesthetized mice. This experiment allows convenient control of the boundary by use of a saline bath as well as providing the depth profile of any measured difference between conditions, and the effect of boundary condition has been previously predicted (Nicholson and Freeman, 1975; Pettersen et al., 2006) and described (Einevoll et al., 2007). To quantify how the change at the brain surface impacts the potentials the averaged evoked response to whisker stimulation in the somatosensory cortex of mice was compared between conditions where the brain surface was dry (insulating) and when it was covered in artificial CSF (ACSF) which is roughly five times more conductive than brain tissue.

## **5.2 Methods**

### **5.2.1 Three-Layer Model**

We propose a planar three-layer model as an approximation of the geometry of intracranial electrophysiology near the brain surface. For sufficiently small electrode arrays we approximate the brain surface as flat and having no lower boundary as a lower half plane with homogenous isotropic conductivity  $0.4 \text{ S/m}$  (Goto et al., 2010). The brain is modeled as being covered by a uniformly thick layer of another material which is bounded from above by a completely insulating layer. In an acute experiment this represents the CSF ( $1.79 \text{ S/m}$  (Latikka and Eskola, 2019)) layer above the brain which is open to air, and for a chronic experiment this approximates an arbitrarily thick layer of fluid or tissue covered by the insulating electrode array or approximating the skull which is relatively insulating (between one and two orders of magnitude less conductive than brain tissue (Vorwerk et al., 2014)) (Fig 5.1).

The sources of electric potentials in the brain are transmembrane currents [Plon-

sey1964]. A small, localized transmembrane current,  $I$ , generates a potential throughout the volume of tissue with conductivity  $\sigma$  that has the familiar form a point charge in electrostatics,

$$V = \frac{I}{4\pi\sigma r} \quad (5.1)$$

where  $r$  is the distance from the source current and the conductivity replaces the permittivity. The effect of the boundaries can be described by the modified Greens function for the three-layer model (see Chapter 3 for derivation) which includes the usual source term as well as image sources whose magnitude and location are determined by the material properties and geometry.

$$V_1(r, z, \phi) = \frac{1}{4\pi\sigma_1} \left[ \frac{1}{\sqrt{r^2 + (z+D)^2}} + \frac{\alpha}{\sqrt{r^2 + (z-D)^2}} + \sum_{n=0}^{\infty} (-\alpha)^n \frac{1 - \alpha^2}{\sqrt{r^2 + (z - D - 2(n+1)T)^2}} \right] \quad (5.2)$$

$$V_2(r, z, \phi) = \frac{1}{4\pi\sigma_1} \sum_{n=0}^{\infty} (-\alpha)^n (1 + \alpha) \left[ \frac{1}{\sqrt{r^2 + (z + D + 2nT)^2}} + \frac{1}{\sqrt{r^2 + (z - D - 2(n+1)T)^2}} \right] \quad (5.3)$$

where  $D$  is the depth of the source,  $T$  is the thickness of the intervening layer,  $\sigma_1$  is the conductivity of the brain,  $\sigma_2$  is the conductivity of the intervening layer, and  $\alpha$  is the quantity

$$\alpha = \frac{\sigma_1 - \sigma_2}{\sigma_1 + \sigma_2} \quad (5.4)$$

The parameters can be altered to match a variety of conditions including no intervening

layer as  $T$  approaches 0, no boundary condition as  $T$  approaches infinity, arbitrarily thick layers of either more or less conducting layers above the brain. The two experimental conditions are both modeled as having ACSF with the same conductivity as CSF (1.79 S/m) as the covering layer, but with the dry condition having a depth,  $T$ , of 0.001 mm and the ACSF condition having a depth of 5 mm.

## 5.2.2 Experimental Procedure

All animal work procedures were in accordance with a protocol approved by the Institutional Animal Care and Use Committees of UC San Diego (protocol S07360).

Adult mice were anesthetized with isoflurane and placed on a heating pad. A femoral artery was catheterized, and a tracheotomy was performed. An incision was made in the scalp to expose the skull. A ball electrode (Ag/Cl) was inserted behind the skull under the scalp to be used as the reference electrode. The skull was fixed to the experimental frame with dental acrylic, and the acrylic was further used to build a well around and extending above the exposed skull. A craniotomy and durotomy are made above right whisker barrel cortex, roughly 3 mm in diameter. The well was filled with artificial CSF (ACSF) to prevent the exposed cortex from drying. The mice were put on artificial respiration prior to administration of pancuronium while blood pressure and CO<sub>2</sub> were monitored. Anesthesia was switched to alpha-chloralose prior to stimulation, and the electrode array was inserted with its location was determined either by single channel microelectrode (FHC, Inc., ME, USA) recording of evoked responses to whisker stimulation or based on stereotactic coordinates estimated from previous recordings. Single or multiple whiskers were stimulated using a wire loop deflected with a piezoelectric actuator by placing the loop around the intended whiskers and deflecting the piezoelectric crystal with a 3-4 A sinusoidal pulse.

A set of trials consisted of 30-80 repetitions of the stimulus evenly spaced at 2



s intervals. Sets were paired by condition; first with the well above the exposure filled with ACSF, then repeated after the exposure was dried by wicking away the ACSF with a Kimwipe (Kimberly-Clark, TX, USA). The precise depth of the ACSF was not controlled between or within experiments, but the well would be filled several millimeters above the cortical surface immediately after each dry set. The model suggests that the effect of increasing the depth of the saline layer is negligible once the depth is greater than around 1 mm.

The electrodes were laminar arrays with 22 contacts spaced 100  $\mu\text{m}$  apart were used to record MUA and LFP. The electrodes were inserted perpendicular to the cortical surface in or near whisker barrel cortex (Fig 5.1a).

Potentials were recorded using an Intan RHD2000 series amplifier and acquisition board (Intan Technologies, CA, USA) connected to the electrode array using a custom-built connector. The potentials were sampled at 20 kHz and were recorded simultaneously with the stimulus triggers.

### **5.2.3 Signal processing and Trial Selection**

Multi-unit activity (MUA) was calculated by applying a high pass filter to the raw signal at 350 Hz and computing the amplitude of the Hilbert transform of the signal. The local field potential (LFP) was obtained using the raw signal downsampled to 4 kHz and only filtered using a notch filter at 60 Hz for line noise removal.

The most superficial electrode was determined from the data by visual inspection of the correlation matrix across electrodes of each ACSF trial. The first channel that was not nearly perfectly correlated (Pearson correlation coefficient slightly less than 1.0) with all channels located above it was determined to be the first, most shallow electrode in contact with the brain.

Trial averages were computed for each set rather than averaged across sets with

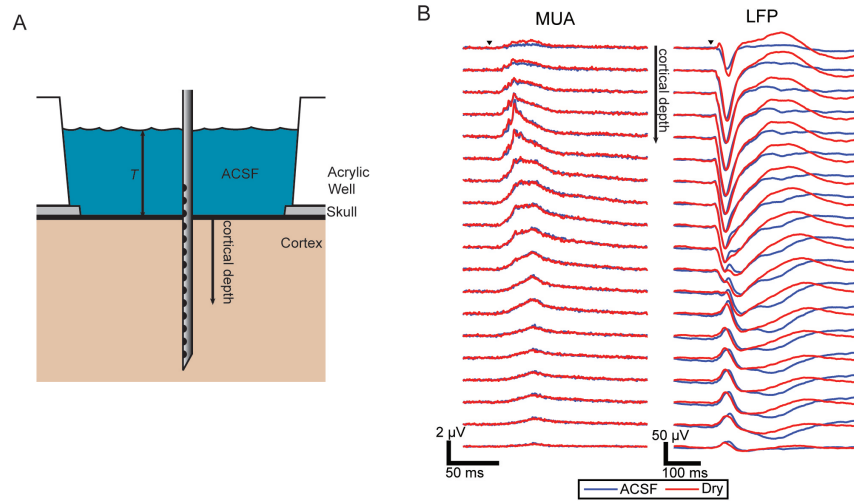


**Figure 5.1.** (A) Schematic of the experiment with the laminar electrode inserted perpendicular to the surface and with the well either filled with ACSF or dried to vary the boundary condition. (B) Grand averages ( $n=43$ , each condition) of the evoked responses of both MUA and LFP signals. Trials covered with ACSF (blue) and dry (red).

the same stimulus so that the comparison between the two boundary conditions was always made between an ACSF set and the successive dry set.

For each set a baseline MUA level was calculated by averaging the MUA signal from 0.09 to 0.01 s prior to the stimulus and subtracting this mean baseline level from the whole signal. The amplitude of a response was characterized by integrating the power of the signal over the duration of the response. For MUA this was calculated by taking the mean of the MUA signal after baseline removal from 0.01 to 0.09 s. For LFP the response amplitude was determined by taking the root-mean-square value of the signal between 0.01 and 0.4 s.

Many sets of trials were recorded in which the stimulation did not evoke an average response large enough to make a comparison between the two conditions. Sets were removed from further analysis if the MUA, after baseline subtraction, did not exceed 0.4 (a.u.) on any channel. After exclusion 43 pairs of ACSF/dry sets of trials

were included.

The comparison between the two conditions was computed as the ratio of the amplitude of the subsequent trials on a per trial, per electrode basis, and the effect as a function of depth was quantified by taking the median across trials for each contact depth. Significance of the median ratio being greater than or less than one was assessed by using two one-sided sign tests (above 1 and below 1) for the distribution of ratios on each contact.

The uncertainty in the depth of the first contact and the true locations of the current sources of the potentials prevents a direct quantitative comparison of the predicted and measured ratios.

#### **5.2.4 Model Predictions**

MUA was modeled by placing a source 50  $\mu\text{m}$  laterally displaced from the electrode location (Xing et al., 2009; Blanche et al., 2005; Moffitt and McIntyre, 2005). This was accomplished by moving the sources for each electrode such that the relative location between the source and electrode is always the same. Sources are modeled as uniform 30  $\mu\text{m}$  spherical current sources or sinks to keep the potential bounded near the source, but to retain the potential of a point source outside of the 30  $\mu\text{m}$  sphere.

A simple model to account for unknown and distributed sources of the LFP is that they are produced by a line of vertical line of sources. This was approximated by 50 sources along the z axis spanning between 0.05 and 3 mm deep and 200  $\mu\text{m}$  laterally displaced from the shank of the electrode. Due to the simplicity of the source geometry relative to real LFP, noise is added before taking the ratio which crudely includes the noise which would be due to all other sources not included the modeled source.

A more realistic model is a current dipole with a sink and source pair. Their locations were chosen using an approximation of the actual sources based on current

source density (CSD) analysis applied to the LFP. The actual current sources and sinks are expected to be spatially distributed and time-varying, but we chose to model only the largest sources and sinks visible as the only source/sink pair which were at depths 0.25 and 1.4 mm. The pair was modeled as being laterally displaced 0.4 mm from the shank of the electrodes to represent the average effective distance to the various responsive whisker barrels as the whisker being stimulated was varied. As with the line source, additive noise is added prior to calculating the ratio between conditions.

The sensitivity of the electrodes was chosen as the metric which summarizes the effect of the boundaries and source locations and configurations (von Ellenrieder et al., 2012). It is a measure of the amplitude of the potential measured at fixed electrode location as a function of the position of a unit source, and accordingly it is measured in units V/A. The construction of sensitivity profiles is common in electrophysiology as the first step of many source localization algorithms that is carried out by modeling the magnitude of potentials induced at an electrode from locations of interest within the brain (Jonmohamadi et al., 2014). In our simple geometry this map is provided by the Greens functions for this boundary value problem.

The sensitivity calculated this way is not true sensitivity of the electrodes which would include electrode effects such as electrode-tissue interface and the size and shape of that interface, and it is important to emphasize that this model represents effects of volume conduction given the geometry and properties of the tissue and surrounding media. Two aspects of the sensitivity profiles of the electrodes that are important considerations for design and interpretation of the potentials are the signal-to-noise ratio (SNR) and spatial specificity of the profile. With an estimate of the noise level present in the recordings and the size of the current source of interest the sensitivity can be used to identify locations from which the response can be reliably measured. Narrow sensitivity profiles may be desirable if we are interested in identifying the locations from which the potential

originates, or broad profiles if detection is of more interest than localization.

To show the effect of altering the brain surface boundary conditions on the SNR we model a typical source for illustrative purposes. Based on our recordings and previous current density estimates (Riera et al., 2012; Higley and Contreras, 2007; Szymanski et al., 2011; Kajikawa and Schroeder, 2014) The source is assumed to be a current density of  $40 \mu\text{A}/\text{mm}^3$  over a region of volume  $0.0062 \text{ mm}^3$  (volume of a  $0.2 \text{ mm}$  cube) which results in a source strength of  $0.25 \mu\text{A}$ . We model the amplitude required to clearly detect this response strongly at an electrode as  $100 \mu\text{V}$ . This defines a threshold sensitivity of about  $400 \text{ V/A}$  from which we can identify the cortical locations with respect to an electrode that would be expected to produce a clear response given our criteria. It has been shown that an intervening saline layer can broaden laterally the sensitivity profile of surface electrodes (Hill et al., 2018; Ness et al., 2015). In the plane defined by a given depth the sensitivity has circular symmetry with a single peak directly under the electrode. To characterize this effect and the sensitivity profile, we compute the half width at half maximum (HWHM) of the sensitivity as a function of source depth.

## **5.3 Results**

### **5.3.1 Model Predictions**

In order to make use of the model for predicting the effect of the boundary condition on the laminar recordings we must have an estimate of both the location of the electrode and the location of the sources being measured. The MUA model was constructed by placing the only sources  $50 \mu\text{m}$  from the position of the virtual electrode. In an infinite medium this would mean uniform amplitudes at all depths due to the sources always being measured locally with no outside effects. With the presence of a boundary condition the effects are limited to the boundary region due to deeper electrodes only

measuring deeper sources which are less affected by the boundary (Fig 5.2).

The location of LFP generating sources is not as easy to generalize as MUA and will always depend on the neuroanatomy and type of activity. A general model of the sources of LFP is a uniform vertical line charge, parallel to the electrodes and offset by 200  $\mu\text{m}$ . This representation weights all cortical layers as contributing current sources to the potential equally and places the average effective distance to be near the electrode. As shown in Fig 5.2, the predicted effect of the boundary condition is also largest at the boundary, but decays much more slowly with depth than the more local MUA effect.

A more physically plausible model uses charge balanced sources (dipoles) which include an equal number of current sources and sinks, and we used a simplified model that includes just one source/sink pair placed based on an estimate from the experimentally measured responses. Fig 5.2 shows that the effect on the amplitude is much larger near the surface, but that due to the change of depth at which the potential is zero there is a jump in the ratio between conditions. Similar to the line source, the effect decays much more slowly with depth, but abruptly shifts to a small amplification near the depth of the deeper current.

### **5.3.2 Experimental Results**

The effect was determined by the ratio of the amplitude of the evoked responses in the ACSF-filled condition and the dry condition. To quantify the magnitude of the response for each condition pair, the trial averages were integrated over the duration of the evoked response. MUA signal is non-negative and the MUA responses are monophasic lending to a straightforward comparison of the magnitude of the average stimulus-evoked response. The evoked LFP has multiple positive and negative peaks and simply integrating the response allows for temporal cancellation to alter the measured ratio. Instead the RMS value over the window is used to estimate the overall magnitude

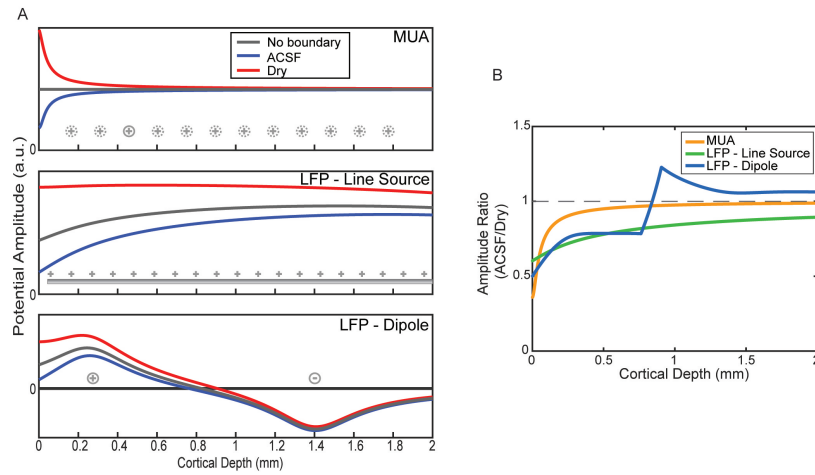


**Figure 5.2.** (A) Potentials as a function of depth are modeled by assuming a source configuration. Depth profiles are plotted for an infinite medium and one bounded by ACSF or an insulator. (B) The ratios between the ACSF and insulating (dry) condition predicted by the model as a function of electrode depth

of the LFP response to account for the relative amplitude of various oscillatory peaks but is still an imperfect measure due to spatial cancellation that may result from the configuration of current sources. Fig 5.1 shows the grand average of the responses across all sets of trials for both MUA and LFP which both show the most difference between conditions near the surface with LFP differences extended to all depths.

The ratio of the responses was calculated per matched set of trials for each electrode depth. The distribution of ratios of the response magnitudes for both MUA and LFP, shown in Fig 5.3, showed clear attenuation for the ACSF sets relative to dry ones at the surface. The median ratio of the MUA amplitude was significantly less than 1 (one-sided sign test  $p < 0.05$ ) for the first three most shallow contacts. The ratio of the LFP amplitude showed significant relative amplification of the dry condition for the first 7 contacts and attenuation at contacts 13 through 18 excluding contact 15.

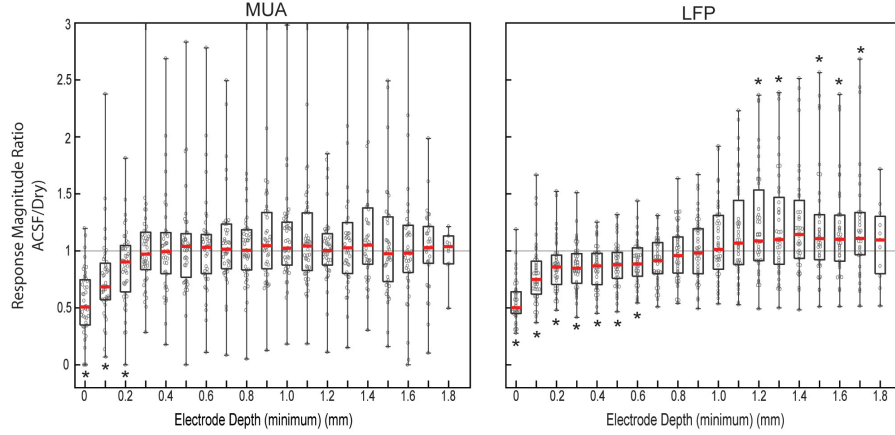


**Figure 5.3.** Distributions of response magnitude ratio of all condition-pair sets of trials. For each approximate electrode depth all of the pairs (gray) and the quartiles (black) and median (red) of the distribution were plotted. Location of \* denotes the median is significantly ( $p < 0.05$ ) above (top) or below (bottom) 1

### 5.3.3 Implications for Electrocorticography

We use the spatial map of the sensitivity of the electrodes a method to compare the effects of electrode array designs and locations. These maps provide the input/output relationship between the location of a given source and the measured potential at the electrode, or the gain of the electrode as a function of source location.

The counterintuitive amplification that occurs at deep electrodes which are measuring a dipole source can be understood by examining the sensitivity profile of a depth electrode as a complement to the method of modeling the sources first. Fig 5.4 shows that the boundary condition effect more strongly effects sources located closer to the boundary while the more distant side is mostly unaffected. The attenuation of the shallow source causes less cancellation of the potential caused by the deeper sink. The effect of the boundary condition on an intracortical electrode is not uniform, significantly impacts the sensitivity for sources in any direction relative to the electrode and is largest near the surface.

When recording from an ECoG array the boundary condition is changed by the



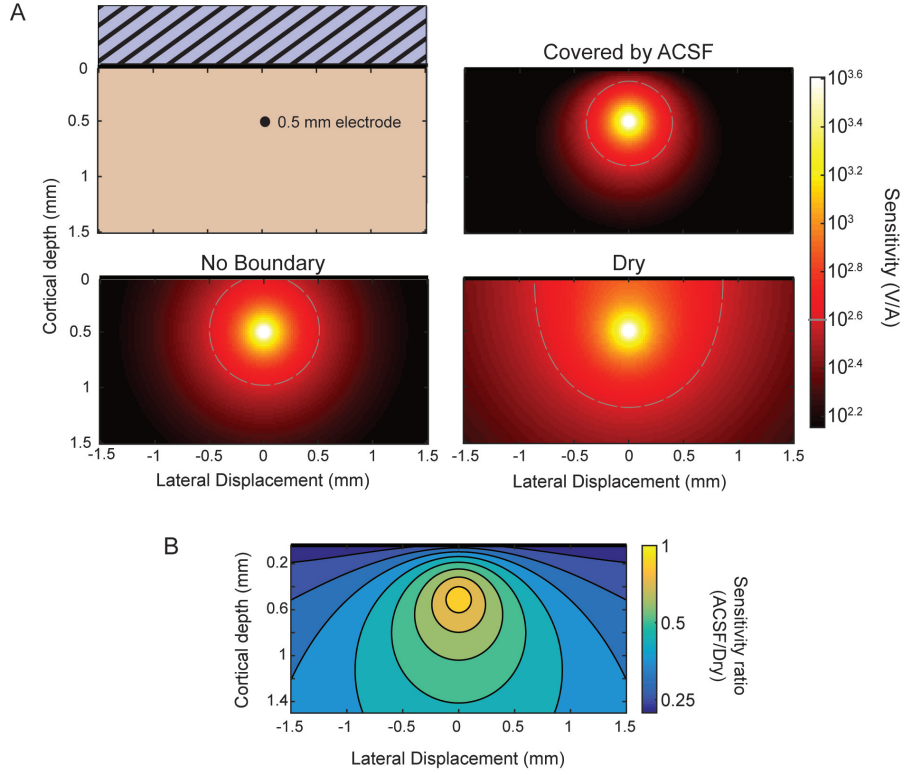


**Figure 5.4.** (A) Lateral cross-section of the sensitivity of an electrode 0.5 mm deep. Comparison between the sensitivity without the presence of a boundary, with a conducting (ACSF) boundary, or an insulating (dry) boundary at the cortical surface. The 400 V/A threshold shown in gray. (B) The ratio of the ACSF and dry sensitivities from (A).

presence or lack of an insulating backing. The ratio between the two types of array designs shown in Fig 5.5 is nearly uniform and is modified by the properties of the tissue that covers the array. Unlike a penetrating electrode, the contacts are always at or above the brain surface, so their sensitivity is always altered significantly by the boundary effects. The level of attenuation is determined mostly by the conductivity ratio term  $\alpha$  which determines the strength and relative sign of the image sources. The approximate sensitivity ratio is the ratio of the total source (real + image) between the two conditions

$$\text{Ratio} = \frac{1 + \alpha_c}{1 + \alpha_i} \quad (5.5)$$

For the insulating boundary  $\alpha$  is +1 representing an image source of the same sign, for tissue of similar conductivity to cortex  $\alpha$  is roughly 0, and for CSF  $\alpha$  is about -2/3. The resulting ratios of approximately 0.5 and 0.33 can be seen in Fig 5 as the attenuation that results from the model and is nearly uniform.

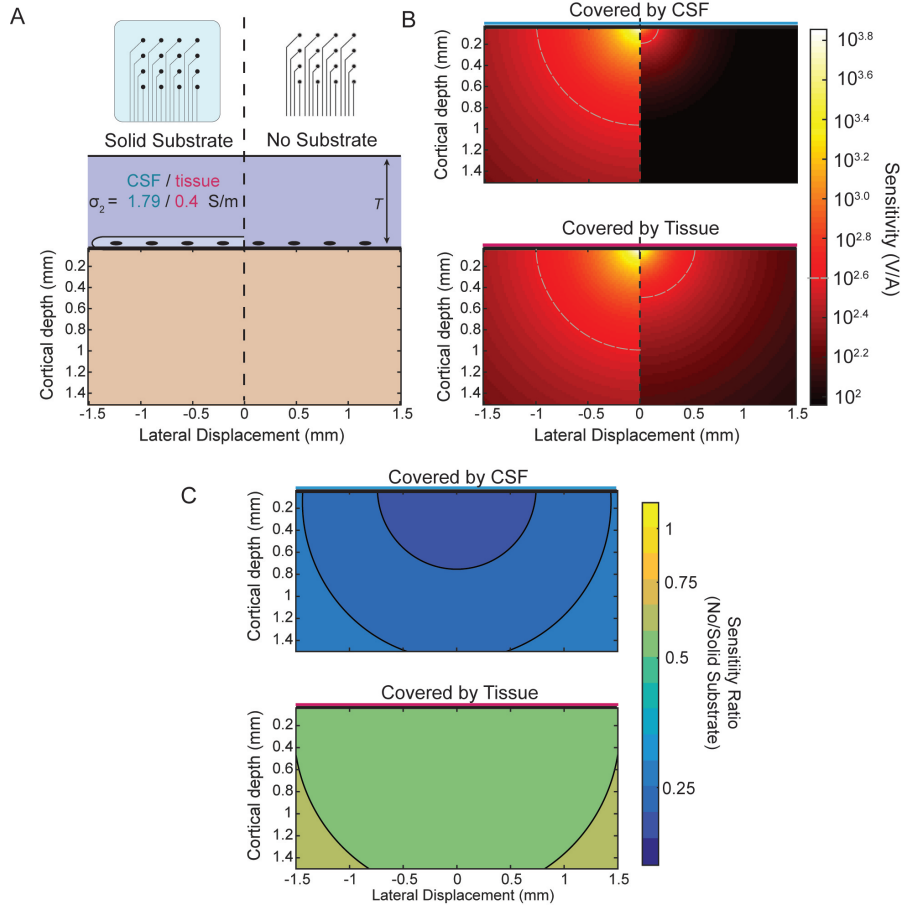


**Figure 5.5.** (A) The design of the array and tissue in which it is implanted affect the sensitivity. Solid (insulating) arrays shown on left and minimal (no insulation) arrays on the right which can be covered by tissue or relatively conductive CSF. (B) Side-by-side comparison of effect of array type on sensitivity for CSF (top) and tissue (bottom). (C) Sensitivity ratio between array types for CSF or tissue above array.

The array may not always lie directly on the pial surface. The array may be implanted above the dura or during chronic implantation scar tissue may grow under the array. When the array is not at the surface the ratio will no longer be uniform?. The effect

of the distance of separation,  $s$ , from the cortical surface and the boundary conditions is summarized in two ways: the size of the region above a threshold sensitivity which captures the effect on the magnitude of the sensitivity, and the HWHM as a function of depth that describes the shape of the sensitivity profile.

The amplification or attenuation caused by the boundary is described by the change in size or shape of the region in which the sensitivity is above some threshold value. Any threshold value is able to show changes in sensitivity, similar to choosing a single isopotential line to plot instead of the entire contour, and for comparison across conditions 400 V/A is chosen based on the threshold at which a typical source would have an amplitude of 100  $\mu\text{V}$  (Fig 5.6). The lack of an insulating layer at the ECoG array dramatically attenuates the signal for any thickness of intervening tissue, shrinking the responsive region. The effect is more pronounced when the material the array is implanted in is more conductive. The effect of increasing the separation of the array from the surface to also attenuate the signals, but the region shrinks less laterally than vertically indicating the effect is larger for deeper sources than lateral ones.

The horizontal broadening of the sensitivity profile is also an important characteristic of the potentials recorded by the electrode. Individually, with a broad sensitivity the electrodes may record larger responses from distant sources, but within an array it may be undesirable for the overlap in the sensitivities of neighboring electrodes to be large. The signals recorded by neighboring electrodes would record similar activity, whereas with an exceptionally narrow, even cylindrical, sensitivity each electrode records a more distinct region of sources. This broadening, caused either by the depth of the sources or by changes in the materials or array, was summarized using the half-width at half maximum (HWHM) of the sensitivity as the lateral displacement is varied at fixed depth. At every depth these lateral slices have a peak directly under the contact, and the HWHM defines the radius at which the sensitivity decreases by half. Volume conduction causes

the profile to inevitably broaden as the sources become deeper, and separation of the contacts from the surface further increases the volume of tissue between the electrode and cortex. The Fig 5.6 shows that increasing the source depth always leads to an increase in HWHM as expected, and that increasing the separation between the array the surface increases the HWHM by a nearly constant amount across all source depths.

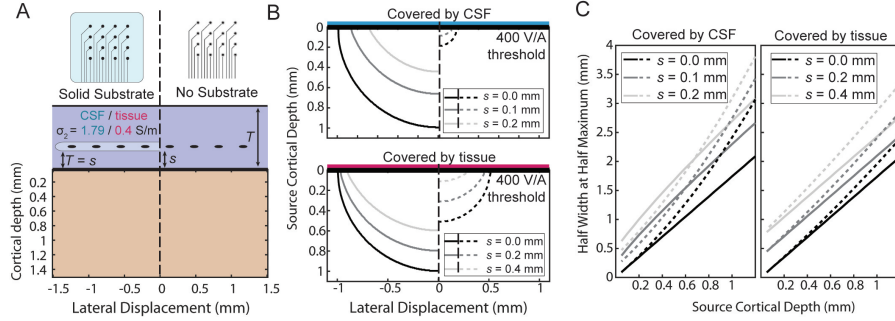


**Figure 5.6.** (A) The sensitivity with a separation,  $s$ , between the surface affects each condition differently. (B) Side-by-side comparison of the shape of the region with sensitivity greater than 400 V/A for various separation distances. (C) Half width at half maximum of the sensitivity as a function of source depth at the same separations as (B).

## 5.4 Discussion

### 5.4.1 Laminar Electrode Effects

The model and the experimental results suggest that the effect of CSF compared to an insulating layer above the cortical surface is limited to contacts near the surface. This agrees with the modeling of single units in Hill et al. (2018) which predicts smaller peak-to-peak amplitudes by about a factor of four when the electrode is small and has no insulating layer.

There are clear differences in the evoked LFP response to both conditions. In our LFP and in [Einevoll2007] the effect is not constrained to the surface but is most apparent in the appearance of an early positive deflection near the surface. The broad influence of boundary was realized in an early CSD study in which the experimental application

of insulating mineral oil to the surface was accounted for in the authors semi-infinite, 2-layer model by simply multiplying all the potentials uniformly by a factor of two (Nicholson and Freeman, 1975). When penetrating arrays are recorded immersed in saline simultaneously with insulating ECoG arrays in our experience there are noticeable differences between the surface recordings including the presence of an early positive potential similar to the change shown in Fig 5.1b.

When conductive media are above the surface the changes in LFP due to the boundary are more difficult to model or quantify. The current sources creating the potentials need to be mapped in order to predict the changes precisely. This could be accomplished from the recorded LFP, but accurate source localization in electrophysiology is itself the subject of study, and furthermore the effect of the boundary would itself need to be incorporated into the localization model. In the model this is accounted for either by use of a spatially neutral line source as an approximation of perhaps the average of many heterogeneous responses across trials, regions, or even species.

By choosing source locations that were motivated by the recorded potentials the model prediction is in better agreement with the experimental result that there is amplification rather than attenuation caused by the more conducting boundary. This is explained by the greater attenuation of the source or sink closer to the surface of a dipole pair which acts to mask its contribution to the potential at a deeper electrode thereby reducing its cancellation of the potential of the deeper source/sink. The qualitative difference between the two models of LFP highlight the importance of source configuration. Sensitivity provides an electrode-centric rather than source-centric view of volume conduction, but the importance of the source configuration should not be neglected. This can be seen in EEG sensitivity models in which the assumed sources are dipoles rather than monopoles and this results in a different, but complementary, profile despite describing the same phenomenon.

### 5.4.2 ECoG Model

It is conventional wisdom that electrode sensitivities are largest near the contact and that minimizing the separation of surface electrodes from the surface improves the recordings, but our model predicts that the type and relative positioning of the boundary influenced by an ECoG array has effects that are much broader than just edge effects. The modeled effect is large and predicts that there is a strong advantage in embedding the electrodes in large insulating substrates as predicted by [Hill2018] for spiking activity, but that this holds true for LFP recordings as well. The nearly spatially uniform attenuation is due to the electrodes always recording from the boundary where the edge effects apply. The factor of 2 attenuation caused by the ACSF well at the top contact of the laminar array for both MUA and LFP agrees with the model assuming the LFP is largely caused by deeper sources.

It is often the case that is undesirable or not possible for ECoG arrays to be implanted in contact with the pial surface, and our three-layer model allows for the effect of an intervening layer to be included. The conductivity and separation values as well as the use 400 V/A threshold and HWHM were chosen to demonstrate the main predictions for common scenarios, and the values can easily be modified to fit other experimental settings. The use of a threshold sensitivity has value in allowing a notion of signal-to-noise ratio (SNR) to be included in the sensitivity analysis. The sensitivity profile alone seems to suggest that every source will be recorded by an electrode, and it is only a matter of the amplitude of the potential. This may be true in principle, but in practice any constellation of sources of interest create potentials that exist in a background of other activity that is temporally and spatially interrelated and complex [Herreras2016] (neural or artifact) that can be categorized as noise. With an understanding of the level of this noise and the magnitude of the current sources of the desired activity, the sensitivity

threshold can be estimated to identify responsive regions in the brain.

The HWHM of the sensitivity also has practical application for array design because it defines the electrode spacing at which a source directly under one electrode will cause a potential with half the amplitude at a nearest neighbor electrode within an array. With an application in mind, this provides a heuristic approach to layout ECoG electrodes to perhaps minimize signal redundancy or, conversely, ensure a desired signal is recorded strongly by multiple electrodes.

As an example, in Schendel et al. (2014) ECoG arrays with different amounts of insulation are implanted chronically. Their results show the footprint of the array impacts the growth of scar tissue above and below the array. Using these measured thicknesses, we can model the relative sensitivity of the two designs (Fig 5.7). For these particular parameters the model favors the use of the mesh array due to the larger sensitivity near the surface and only modest attenuation at larger distances. The success of recording micro-ECoG through a thinned skull [Brodnick2019] also motivates extending the model to 4 layers to make predictions about the properties of thinned skull ECoG. Still, intuition gained from our model suggests the limitation of that method is not the very thin layer of bone, rather it is the much thicker layers of tissue and conductive CSF between the array and cortical surface (similar to the effect on EEG in Rice et al. (2013)).

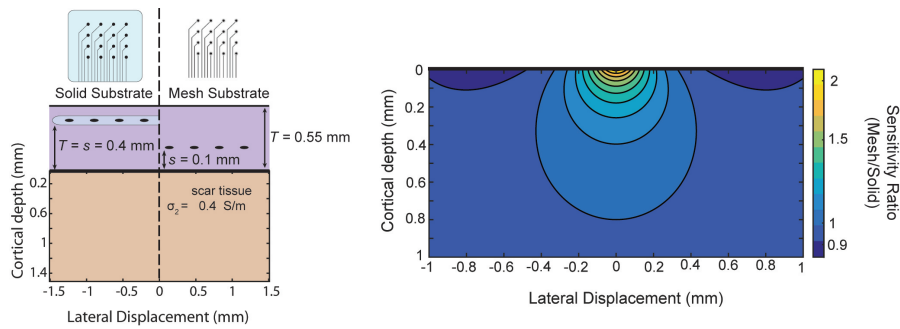


**Figure 5.7.** Comparison of two electrode array designs which impact scar tissue formation as shown in Schendel et al. (2014). Using scar tissue thickness reported by the authors the model predicts the sensitivity ratio between the two arrays after tissue growth

In our model the near uniformity is also a consequence of the simplifying assumptions of infinite depth and lateral extent of the grey matter. Even in our simple model the scale of the effect as a function of depth is limited by the thickness of the middle layer of CSF/tissue. For sources much deeper than this thickness the boundary begins to appear increasingly like a simple insulating boundary, and the ratio approaches 1.0. The thickness of the tissue/CSF layer is often much thicker than cortex, where the sources of interest are concentrated in micro-ECoG, but this does suggest that arrays lacking insulation may record LFPs that are largely unaffected if they are covered by a layer of material that is thinner than the depth of the sources of interest.

The approximations limit the application of our results to sources whose depth is much less than the extent of the insulation of the array, the size of the craniotomy, or the radius of curvature of the cortical surface. If limited to applications of micro-ECoG and measuring cortical activity, the latter approximations will generally be valid. We can apply scaling arguments to the results of Hill et al. (2018) to understand the effect of finite insulating area on deeper sources. Using FEM models to vary the size of the insulation area around the electrode and they predicted that for a  $20\text{ }\mu\text{m}$  deep source it takes  $30\text{ }\mu\text{m}$  of lateral insulation to maintain 95% of the fully insulated amplitude. Under the approximation that the array is covered by a very deep layer of CSF and in a very large craniotomy these results suggest that the size of the insulating layer has a small impact as long as the insulation extends in any direction more than 50% farther than the depth of the sources.

As ECoG arrays continue to be developed their design has been influenced largely by mechanical, physiological, and optical considerations. Electrode arrays affect the electrical conduction of the signals, and there is a complex interplay between all these factors in determining the qualities of the recordings. The impact of implanting the devices, which may be minor, of limited extent, and/or difficult to modify in other



modalities, is significant in ECoG and should be a major consideration in the design of the arrays.

Chapter 5, in full, is a reprint of the material as submitted in Theoretical and Experimental Analysis of the Impact of Brain Surface Boundary Conditions and Implications for Electrographicography to Frontiers in Neuroscience in 2019. Rogers, Nicholas; Thunemann, Martin; Devor, Anna; Gilja, Vikash. The dissertation author was the primary investigator and author of this material.

# Chapter 6

## Concluding Remarks

Building on custom electrodes and open source electrophysiology systems has allowed us to test novel arrays in a variety of settings. The small size of the electrodes make them well suited to use in rodent model, and an added benefit of their use in mouse is their transparency and low profile allows them to be combined with optical techniques. The trend in human ECoG applied to BCI is towards smaller electrodes, and we expect in the near future these arrays will begin to be applied to BCI research.

The recording system presented in this dissertation has been adapted and is being used by multiple labs across multiple universities in human, rodent, porcine, and primate models. The diverse uses owe to the flexibility (mechanical and in terms of design) of the IEBL-fabricated electrodes.

Chapter 3 provides a guideline to aid design of future ECoG arrays. Spatial variation of the potentials depends strongly on frequency and species as previously understood, but this variation can be understood intuitively in terms of regularly shaped regions of temporal patterns of the potential. These regions are also explanatory of the correlation or coherence that is usually used to describe the spatial variation present in ECoG. The results show there may even be room to further shrink arrays even with less than 100 channels for arrays that can be precisely located on small cortical targets. Especially so because higher frequencies such as beta around 20 Hz and gamma above

50 Hz tend to be especially informative and have more high spatial frequency variation.

The goal of chapter 5 is in addition to also provide design guidelines, to also explain the properties of ECoG recording in terms of volume conduction in a quantitative way. Researchers have good intuition for how volume conduction attenuates potentials in general, but it becomes more difficult take into account the effect of multiple boundaries and complicated geometry in our thinking. The relative amplitude of potentials recorded along a laminar electrode between boundary conditions is an example of simple, but not necessarily intuitive effects.

Successful array design will take into consideration an understanding of empirical studies, physical, and physiological knowledge. Combining empirical results about the signals and physical understanding of volume conduction and its effects on the signals with an understanding of the brain will better allow for array design to be best suited for the application. Knowledge of cortical regions of interest, their size, their connections, the type of signals they produce, or models of their activity is the missing piece from the general aspects considered in this work. Concretely, this is exemplified in the sensitivity profiles which on their own are instructive, but to truly guide electrode design need to be combined with at least a rough idea of the locations and interrelations between the sources of neural activity. More broadly, we have presented tools and guidelines, but design trade-offs remain the main aspect that must be balanced and optimized for each application. However, our work has shown that fractions of a millimeter is within the range of practical pitches to be considered in future designs, and it remains to be seen if future studies will show benefits to the use of even smaller arrays.

# Bibliography

- Abidian, M. R., Corey, J. M., Kipke, D. R., Martin, D. C., 2010. Conducting-polymer nanotubes improve electrical properties, mechanical adhesion, neural attachment, and neurite outgrowth of neural electrodes. *small* 6 (3), 421–429.
- Abidian, M. R., Ludwig, K. A., Marzullo, T. C., Martin, D. C., Kipke, D. R., 2009. Interfacing conducting polymer nanotubes with the central nervous system: chronic neural recording using poly (3, 4-ethylenedioxythiophene) nanotubes. *Advanced Materials* 21 (37), 3764–3770.
- Abidian, M. R., Martin, D. C., 2008. Experimental and theoretical characterization of implantable neural microelectrodes modified with conducting polymer nanotubes. *Biomaterials* 29 (9), 1273–1283.
- Abidian, M. R., Martin, D. C., 2009. Multifunctional nanobiomaterials for neural interfaces. *Advanced Functional Materials* 19 (4), 573–585.
- Asplund, M., Thaning, E., Lundberg, J., Sandberg-Nordqvist, A., Kostyszyn, B., Inganäs, O., von Holst, H., 2009. Toxicity evaluation of pedot/biomolecular composites intended for neural communication electrodes. *Biomedical Materials* 4 (4), 045009.
- Benjamini, Y., Hochberg, Y., 1995. Controlling the false discovery rate: a practical and powerful approach to multiple testing *jr stat soc b* 57: 289–300. Find this article online.
- Blanche, T. J., Spacek, M. A., Hetke, J. F., Swindale, N. V., 2005. Polytrodes: high-density silicon electrode arrays for large-scale multiunit recording. *Journal of neurophysiology* 93 (5), 2987–3000.
- Breshears, J. D., Roland, J. L., Sharma, M., Gaona, C. M., Freudenburg, Z. V., Tempelhoff, R., Avidan, M. S., Leuthardt, E. C., 2010. Stable and dynamic cortical electrophysiology of induction and emergence with propofol anesthesia. *Proceedings of the National Academy of Sciences* 107 (49), 21170–21175.
- Brodnick, S. K., Ness, J., Richner, T., Thongpang, S., Novello, J., Hayat, M., Cheng,

- K. P., Krugner-Higby, L., Suminski, A. J., Ludwig, K., et al., 2019.  $\mu$ ecog recordings through a thinned skull. *bioRxiv*, 564146.
- Bullock, T., McClune, M., Achimowicz, J., Iragui-Madoz, V., Duckrow, R., Spencer, S., 1995. Eeg coherence has structure in the millimeter domain: subdural and hippocampal recordings from epileptic patients. *Electroencephalography and clinical neurophysiology* 95 (3), 161–177.
- Bullock, T. H., McClune, M. C., 1989. Lateral coherence of the electrocorticogram: a new measure of brain synchrony. *Electroencephalography and clinical neurophysiology* 73 (6), 479–498.
- Buzsáki, G., 2004. Large-scale recording of neuronal ensembles. *Nature neuroscience* 7 (5), 446.
- Canolty, R. T., Edwards, E., Dalal, S. S., Soltani, M., Nagarajan, S. S., Kirsch, H. E., Berger, M. S., Barbaro, N. M., Knight, R. T., 2006. High gamma power is phase-locked to theta oscillations in human neocortex. *science* 313 (5793), 1626–1628.
- Casimo, K., Darvas, F., Wander, J., Ko, A., Grabowski, T. J., Novotny, E., Poliakov, A., Ojemann, J. G., Weaver, K. E., 2016. Regional patterns of cortical phase synchrony in the resting state. *Brain connectivity* 6 (6), 470–481.
- Chao, Z. C., Nagasaka, Y., Fujii, N., 2010. Long-term asynchronous decoding of arm motion using electrocorticographic signals in monkeys. *Frontiers in neuroengineering* 3.
- Chestek, C. A., Gilja, V., Blabe, C. H., Foster, B. L., Shenoy, K. V., Parvizi, J., Henderson, J. M., 2013. Hand posture classification using electrocorticography signals in the gamma band over human sensorimotor brain areas. *Journal of neural engineering* 10 (2), 026002.
- Cogan, S. F., 2008. Neural stimulation and recording electrodes. *Annu. Rev. Biomed. Eng.* 10, 275–309.
- Cogan, S. F., Ludwig, K. A., Welle, C. G., Takmakov, P., 2016. Tissue damage thresholds during therapeutic electrical stimulation. *Journal of neural engineering* 13 (2), 021001.
- Cui, X., Lee, V. A., Raphael, Y., Wiler, J. A., Hetke, J. F., Anderson, D. J., Martin, D. C., 2001. Surface modification of neural recording electrodes with conducting polymer/biomolecule blends. *Journal of Biomedical Materials Research: An Official Journal of The Society for Biomaterials, The Japanese Society for Biomaterials, and*

- The Australian Society for Biomaterials and the Korean Society for Biomaterials 56 (2), 261–272.
- Delorme, A., Makeig, S., Mar 2004. Eeglab: an open source toolbox for analysis of single-trial eeg dynamics including independent component analysis. *Journal of neuroscience methods* 134 (1), 9–21.
- Dubey, A., Ray, S., 2016. Spatial spread of local field potential is band-pass in the primary visual cortex. *Journal of neurophysiology* 116 (4), 1986–1999.
- Edwards, E., Soltani, M., Kim, W., Dalal, S. S., Nagarajan, S. S., Berger, M. S., Knight, R. T., 2009. Comparison of time–frequency responses and the event-related potential to auditory speech stimuli in human cortex. *Journal of neurophysiology* 102 (1), 377–386.
- Einevoll, G. T., Pettersen, K. H., Devor, A., Ulbert, I., Halgren, E., Dale, A. M., 2007. Laminar population analysis: estimating firing rates and evoked synaptic activity from multielectrode recordings in rat barrel cortex. *Journal of neurophysiology* 97 (3), 2174–2190.
- Fein, G., Raz, J., Brown, F. F., Merrin, E. L., 1988. Common reference coherence data are confounded by power and phase effects. *Electroencephalography and clinical neurophysiology* 69 (6), 581–584.
- Gabriel, S., Lau, R., Gabriel, C., 1996. The dielectric properties of biological tissues: Iii. parametric models for the dielectric spectrum of tissues. *Physics in Medicine & Biology* 41 (11), 2271.
- Ganji, M., Elthakeb, A. T., Tanaka, A., Gilja, V., Halgren, E., Dayeh, S. A., 2017a. Scaling effects on the electrochemical performance of poly (3, 4-ethylenedioxythiophene (pedot), au, and pt for electrocorticography recording. *Advanced Functional Materials* 27 (42).
- Ganji, M., Kaestner, E., Hermiz, J., Rogers, N., Tanaka, A., Cleary, D., Lee, S. H., Snider, J., Halgren, M., Cosgrove, G. R., et al., 2017b. Development and translation of pedot: Pss microelectrodes for intraoperative monitoring. *Advanced Functional Materials*.
- Ganji, M., Tanaka, A., Gilja, V., Halgren, E., Dayeh, S. A., 2017c. Scaling effects on the electrochemical stimulation performance of au, pt, and pedot: Pss electrocorticography arrays. *Advanced Functional Materials* 27 (42).
- Goto, T., Hatanaka, R., Ogawa, T., Sumiyoshi, A., Riera, J., Kawashima, R., 2010. An evaluation of the conductivity profile in the somatosensory barrel cortex of wistar rats.

- Journal of neurophysiology 104 (6), 3388–3412.
- Green, R. A., Hassarati, R. T., Goding, J. A., Baek, S., Lovell, N. H., Martens, P. J., Poole-Warren, L. A., 2012. Conductive hydrogels: mechanically robust hybrids for use as biomaterials. *Macromolecular bioscience* 12 (4), 494–501.
- Green, R. A., Lovell, N. H., Wallace, G. G., Poole-Warren, L. A., 2008. Conducting polymers for neural interfaces: challenges in developing an effective long-term implant. *Biomaterials* 29 (24-25), 3393–3399.
- Groenendaal, L., Jonas, F., Freitag, D., Pielartzik, H., Reynolds, J. R., 2000. Poly (3, 4-ethylenedioxythiophene) and its derivatives: past, present, and future. *Advanced materials* 12 (7), 481–494.
- Hatsopoulos, N. G., Donoghue, J. P., 2009. The science of neural interface systems. *Annual review of neuroscience* 32, 249–266.
- Heim, M., Yvert, B., Kuhn, A., 2012. Nanostructuration strategies to enhance micro-electrode array (mea) performance for neuronal recording and stimulation. *Journal of Physiology-Paris* 106 (3-4), 137–145.
- Hermiz, J., Rogers, N., Kaestner, E., Ganji, M., Cleary, D., Snider, J., Barba, D., Dayeh, S., Halgren, E., Gilja, V., 2016. A clinic compatible, open source electrophysiology system. In: *Engineering in Medicine and Biology Society (EMBC), 2016 IEEE 38th Annual International Conference of the. IEEE*, pp. 4511–4514.
- Hermiz, J., Rogers, N., Kaestner, E., Ganji, M., Cleary, D. R., Carter, B. S., Barba, D., Dayeh, S. A., Halgren, E., Gilja, V., 2018. Sub-millimeter ecog pitch in human enables higher fidelity cognitive neural state estimation. *NeuroImage* 176, 454–464.
- Herreras, O., 2016. Local field potentials: Myths and misunderstandings. *Frontiers in neural circuits* 10.
- Higley, M. J., Contreras, D., 2007. Cellular mechanisms of suppressive interactions between somatosensory responses in vivo. *Journal of neurophysiology* 97 (1), 647–658.
- Hill, M., Rios, E., Sudhakar, S. K., Roossien, D. H., Caldwell, C., Cai, D., Ahmed, O. J., Lempka, S. F., Chestek, C. A., 2018. Quantitative simulation of extracellular single unit recording from the surface of cortex. *Journal of neural engineering* 15 (5), 056007.
- Horton, J. C., Adams, D. L., 2005. The cortical column: a structure without a function.

- Philosophical Transactions of the Royal Society B: Biological Sciences 360 (1456), 837–862.
- House, P. A., MacDonald, J. D., Tresco, P. A., Normann, R. A., 2006. Acute microelectrode array implantation into human neocortex: preliminary technique and histological considerations. *Neurosurgical focus* 20 (5), 1–4.
- Hu, S., Stead, M., Dai, Q., Worrell, G. A., Oct 2010. On the recording reference contribution to eeg correlation, phase synchrony, and coherence. *IEEE transactions on systems, man, and cybernetics. Part B, Cybernetics : a publication of the IEEE Systems, Man, and Cybernetics Society* 40 (5), 1294–304.
- Hu, S., Stead, M., Worrell, G. A., Sep 2007. Automatic identification and removal of scalp reference signal for intracranial eegs based on independent component analysis. *IEEE transactions on bio-medical engineering* 54 (9), 1560–72.
- Huupponen, E., Maksimow, A., Lapinlampi, P., Särkelä, M., Saastamoinen, A., Snapir, A., Scheinin, H., Scheinin, M., Meriläinen, P., HIMANEN, S.-L., et al., 2008. Electroencephalogram spindle activity during dexmedetomidine sedation and physiological sleep. *Acta Anaesthesiologica Scandinavica* 52 (2), 289–294.
- Jonmohamadi, Y., Poudel, G., Innes, C., Weiss, D., Krueger, R., Jones, R., 2014. Comparison of beamformers for eeg source signal reconstruction. *Biomedical Signal Processing and Control* 14, 175–188.
- Kajikawa, Y., Schroeder, C. E., Dec 2011. How local is the local field potential? *Neuron* 72 (5), 847–58.
- Kajikawa, Y., Schroeder, C. E., 2014. Generation of field potentials and modulation of their dynamics through volume integration of cortical activity. *Journal of neurophysiology* 113 (1), 339–351.
- Kellis, S., Sorensen, L., Darvas, F., Sayres, C., ONeill, K., Brown, R. B., House, P., Ojemann, J., Greger, B., 2016. Multi-scale analysis of neural activity in humans: implications for micro-scale electrocorticography. *Clinical Neurophysiology* 127 (1), 591–601.
- Kim, D.-H., Wiler, J. A., Anderson, D. J., Kipke, D. R., Martin, D. C., 2010a. Conducting polymers on hydrogel-coated neural electrode provide sensitive neural recordings in auditory cortex. *Acta biomaterialia* 6 (1), 57–62.
- Kim, J.-H., Kang, G., Nam, Y., Choi, Y.-K., 2010b. Surface-modified microelectrode



- array with flake nanostructure for neural recording and stimulation. *Nanotechnology* 21 (8), 085303.
- Kinney, J. P., Bernstein, J. G., Meyer, A. J., Barber, J. B., Bolivar, M., Newbold, B., Scholvin, J., Moore-Kochlacs, C., Wentz, C. T., Kopell, N. J., et al., 2015. A direct-to-drive neural data acquisition system. *Frontiers in neural circuits* 9, 46.
- Kofke, W. A., Tempelhoff, R., Dasheiff, R. M., 1997. Anesthetic implications of epilepsy, status epilepticus, and epilepsy surgery. *Journal of neurosurgical anesthesiology* 9 (4), 349–372.
- Krusienski, D. J., Grosse-Wentrup, M., Galán, F., Coyle, D., Miller, K. J., Forney, E., Anderson, C. W., Apr 2011. Critical issues in state-of-the-art brain-computer interface signal processing. *Journal of neural engineering* 8 (2), 025002.
- Lagoa, C. E., Bartels, J., Baratt, A., Tseng, G., Clermont, G., Fink, M. P., Billiar, T. R., Vodovotz, Y., 2006. The role of initial trauma in the host's response to injury and hemorrhage: insights from a correlation of mathematical simulations and hepatic transcriptomic analysis. *Shock* 26 (6), 592–600.
- Latikka, J., Eskola, H., 2019. The resistivity of human brain tumours in vivo. *Annals of biomedical engineering* 47 (3), 706–713.
- Leopold, D. A., Murayama, Y., Logothetis, N. K., 2003. Very slow activity fluctuations in monkey visual cortex: implications for functional brain imaging. *Cerebral cortex* 13 (4), 422–433.
- Łeski, S., Lindén, H., Tetzlaff, T., Pettersen, K. H., Einevoll, G. T., 2013. Frequency dependence of signal power and spatial reach of the local field potential. *PLoS Comput Biol* 9 (7), e1003137.
- Lindén, H., Tetzlaff, T., Potjans, T. C., Pettersen, K. H., Grün, S., Diesmann, M., Einevoll, G. T., 2011. Modeling the spatial reach of the lfp. *Neuron* 72 (5), 859–872.
- Ludwig, K. A., Uram, J. D., Yang, J., Martin, D. C., Kipke, D. R., 2006. Chronic neural recordings using silicon microelectrode arrays electrochemically deposited with a poly (3, 4-ethylenedioxythiophene)(pedot) film. *Journal of neural engineering* 3 (1), 59.
- Maier, A., Adams, G. K., Aura, C., Leopold, D. A., 2010. Distinct superficial and deep laminar domains of activity in the visual cortex during rest and stimulation. *Frontiers in systems neuroscience* 4.

- Manganotti, P., Gerloff, C., Toro, C., Katsuta, H., Sadato, N., Zhuang, P., Leocani, L., Hallett, M., Feb 1998. Task-related coherence and task-related spectral power changes during sequential finger movements. *Electroencephalography and clinical neurophysiology* 109 (1), 50–62.
- Menon, V., Freeman, W. J., Cutillo, B. A., Desmond, J. E., Ward, M. F., Bressler, S. L., Laxer, K. D., Barbaro, N., Gevins, A. S., Feb 1996. Spatio-temporal correlations in human gamma band electrocorticograms. *Electroencephalography and clinical neurophysiology* 98 (2), 89–102.
- Merrill, D. R., Bikson, M., Jefferys, J. G., 2005. Electrical stimulation of excitable tissue: design of efficacious and safe protocols. *Journal of neuroscience methods* 141 (2), 171–198.
- Mesgarani, N., Cheung, C., Johnson, K., Chang, E. F., 2014. Phonetic feature encoding in human superior temporal gyrus. *Science* 343 (6174), 1006–1010.
- Michelmann, S., Treder, M. S., Griffiths, B., Kerrén, C., Roux, F., Wimber, M., Rollings, D., Sawlani, V., Chelvarajah, R., Gollwitzer, S., et al., 2018. Data-driven re-referencing of intracranial eeg based on independent component analysis (ica). *Journal of neuroscience methods* 307, 125–137.
- Miller, K. J., Leuthardt, E. C., Schalk, G., Rao, R. P., Anderson, N. R., Moran, D. W., Miller, J. W., Ojemann, J. G., 2007. Spectral changes in cortical surface potentials during motor movement. *Journal of Neuroscience* 27 (9), 2424–2432.
- Mitzdorf, U., 1985. Current source-density method and application in cat cerebral cortex: investigation of evoked potentials and eeg phenomena. *Physiological reviews* 65 (1), 37–100.
- Moffitt, M. A., McIntyre, C. C., 2005. Model-based analysis of cortical recording with silicon microelectrodes. *Clinical neurophysiology* 116 (9), 2240–2250.
- Muller, L., Hamilton, L. S., Edwards, E., Bouchard, K. E., Chang, E. F., 2016. Spatial resolution dependence on spectral frequency in human speech cortex electrocorticography. *Journal of Neural Engineering* 13 (5), 056013.
- Murphy, M., Bruno, M.-A., Riedner, B. A., Boveroux, P., Noirhomme, Q., Landsness, E. C., Brichant, J.-F., Phillips, C., Massimini, M., Laureys, S., et al., 2011. Propofol anesthesia and sleep: a high-density eeg study. *Sleep* 34 (3), 283–291.
- Nakasato, N., Levesque, M. F., Barth, D. S., Baumgartner, C., Rogers, R. L., Sutherling,

- W. W., 1994. Comparisons of meg, eeg, and ecog source localization in neocortical partial epilepsy in humans. *Electroencephalography and clinical neurophysiology* 91 (3), 171–178.
- Ness, T. V., Chintaluri, C., Potworowski, J., Łeski, S., Głabska, H., Wójcik, D. K., Einevoll, G. T., 2015. Modelling and analysis of electrical potentials recorded in microelectrode arrays (meas). *Neuroinformatics* 13 (4), 403–426.
- Newman, J. P., Zeller-Townson, R., Fong, M.-F., Arcot Desai, S., Gross, R. E., Potter, S. M., 2013. Closed-loop, multichannel experimentation using the open-source neuroright electrophysiology platform. *Frontiers in neural circuits* 6, 98.
- Nicholson, C., Freeman, J. A., 1975. Theory of current source-density analysis and determination of conductivity tensor for anuran cerebellum. *Journal of neurophysiology* 38 (2), 356–368.
- Nunez, P. L., Srinivasan, R., Westdorp, A. F., Wijesinghe, R. S., Tucker, D. M., Silberstein, R. B., Cadusch, P. J., 1997. Eeg coherency: I: statistics, reference electrode, volume conduction, laplacians, cortical imaging, and interpretation at multiple scales. *Electroencephalography and clinical neurophysiology* 103 (5), 499–515.
- Obien, M. E. J., Deligkaris, K., Bullmann, T., Bakkum, D. J., Frey, U., 2015. Revealing neuronal function through microelectrode array recordings. *Frontiers in neuroscience* 8, 423.
- Ollikainen, J. O., Vauhkonen, M., Karjalainen, P. A., Kaipio, J. P., 2000. Effects of electrode properties on eeg measurements and a related inverse problem. *Medical engineering & physics* 22 (8), 535–545.
- O'Neill, K., House, P. A., Greger, B., 2016. Analysis of signals recorded from human cerebral cortex using micro-scale electrode arrays during articulate movements. In: *Signals, Systems and Computers, 2016 50th Asilomar Conference on. IEEE*, pp. 841–845.
- Oostenveld, R., Fries, P., Maris, E., Schoffelen, J.-M., 2011. Fieldtrip: open source software for advanced analysis of meg, eeg, and invasive electrophysiological data. *Computational intelligence and neuroscience* 2011, 1.
- Parabucki, A., Lampl, I., 2017. Volume conduction coupling of whisker-evoked cortical lfp in the mouse olfactory bulb. *Cell reports* 21 (4), 919–925.
- Park, S., Song, Y. J., Boo, H., Chung, T. D., 2010. Nanoporous pt microelectrode for

- neural stimulation and recording: in vitro characterization. *The Journal of Physical Chemistry C* 114 (19), 8721–8726.
- Pettersen, K. H., Devor, A., Ulbert, I., Dale, A. M., Einevoll, G. T., 2006. Current-source density estimation based on inversion of electrostatic forward solution: effects of finite extent of neuronal activity and conductivity discontinuities. *Journal of neuroscience methods* 154 (1-2), 116–133.
- Polikov, V. S., Tresco, P. A., Reichert, W. M., 2005. Response of brain tissue to chronically implanted neural electrodes. *Journal of neuroscience methods* 148 (1), 1–18.
- Ramon, C., Holmes, M. D., oct 2014. Spatiotemporal phase clusters and phase synchronization patterns derived from high density eeg and ecog recordings. *Current opinion in neurobiology* 31C, 127–132.
- Ray, S., Crone, N. E., Niebur, E., Franaszczuk, P. J., Hsiao, S. S., 2008. Neural correlates of high-gamma oscillations (60–200 hz) in macaque local field potentials and their potential implications in electrocorticography. *Journal of Neuroscience* 28 (45), 11526–11536.
- Rice, J. K., Rorden, C., Little, J. S., Parra, L. C., 2013. Subject position affects eeg magnitudes. *NeuroImage* 64, 476–484.
- Riera, J. J., Ogawa, T., Goto, T., Sumiyoshi, A., Nonaka, H., Evans, A., Miyakawa, H., Kawashima, R., 2012. Pitfalls in the dipolar model for the neocortical eeg sources. *Journal of neurophysiology* 108 (4), 956–975.
- Rivnay, J., Inal, S., Collins, B. A., Sessolo, M., Stavrinidou, E., Strakosas, X., Tassone, C., Delongchamp, D. M., Malliaras, G. G., 2016. Structural control of mixed ionic and electronic transport in conducting polymers. *Nature communications* 7, 11287.
- Rogers, N., Hermiz, J., Ganji, M., Kaestner, E., Kılıç, K., Hossain, L., Thunemann, M., Cleary, D. R., Carter, B. S., Barba, D., et al., 2019. Correlation structure in micro-ecog recordings is described by spatially coherent components. *PLoS computational biology* 15 (2), e1006769.
- Rouse, A., Williams, J., Wheeler, J., Moran, D., 2016. Spatial co-adaptation of cortical control columns in a micro-ecog brain–computer interface. *Journal of neural engineering* 13 (5), 056018.
- Rubehn, B., Bosman, C., Oostenveld, R., Fries, P., Stieglitz, T., 2009. A mems-based flexible multichannel ecog-electrode array. *Journal of neural engineering* 6 (3), 036003.

- Sahin, N. T., Pinker, S., Cash, S. S., Schomer, D., Halgren, E., 2009. Sequential processing of lexical, grammatical, and phonological information within brocas area. *Science* 326 (5951), 445–449.
- Schalk, G., Leuthardt, E. C., 2011. Brain-computer interfaces using electrocorticographic signals. *IEEE reviews in biomedical engineering* 4, 140–154.
- Schalk, G., Miller, K. J., Anderson, N. R., Wilson, J. A., Smyth, M. D., Ojemann, J. G., Moran, D. W., Wolpaw, J. R., Leuthardt, E. C., 2008. Two-dimensional movement control using electrocorticographic signals in humans. *Journal of neural engineering* 5 (1), 75.
- Schendel, A. A., Nonte, M. W., Vokoun, C., Richner, T. J., Brodnick, S. K., Atry, F., Frye, S., Bostrom, P., Pashaie, R., Thongpang, S., et al., 2014. The effect of micro-ecog substrate footprint on the meningeal tissue response. *Journal of neural engineering* 11 (4), 046011.
- Siegle, J. H., Hale, G. J., Newman, J. P., Voigts, J., 2015. Neural ensemble communities: open-source approaches to hardware for large-scale electrophysiology. *Current opinion in neurobiology* 32, 53–59.
- Slutzky, M. W., Jordan, L. R., Krieg, T., Chen, M., Mogul, D. J., Miller, L. E., 2010. Optimal spacing of surface electrode arrays for brain–machine interface applications. *Journal of neural engineering* 7 (2), 026004.
- Souza, P., Rosen, S., 2009. Effects of envelope bandwidth on the intelligibility of sine- and noise-vocoded speech. *The Journal of the Acoustical Society of America* 126 (2), 792–805.
- Stam, C. J., Nolte, G., Daffertshofer, A., Nov 2007. Phase lag index: assessment of functional connectivity from multi channel eeg and meg with diminished bias from common sources. *Human brain mapping* 28 (11), 1178–93.
- Szymanski, F. D., Rabinowitz, N. C., Magri, C., Panzeri, S., Schnupp, J. W., 2011. The laminar and temporal structure of stimulus information in the phase of field potentials of auditory cortex. *Journal of Neuroscience* 31 (44), 15787–15801.
- Takaura, K., Tsuchiya, N., Fujii, N., 2016. Frequency-dependent spatiotemporal profiles of visual responses recorded with subdural ecog electrodes in awake monkeys: Differences between high- and low-frequency activity. *NeuroImage* 124, 557–572.
- Taplin, A. M., de Pestors, A., Brunner, P., Hermes, D., Dalfino, J. C., Adamo, M. A.,

- Ritaccio, A. L., Schalk, G., 2016. Intraoperative mapping of expressive language cortex using passive real-time electrocorticography. *Epilepsy & behavior case reports* 5, 46–51.
- Tenke, C. E., Kayser, J., 2012. Generator localization by current source density (csd): implications of volume conduction and field closure at intracranial and scalp resolutions. *Clinical neurophysiology* 123 (12), 2328–2345.
- Thakor, N. V., 2013. Translating the brain-machine interface. *Science translational medicine* 5 (210), 210ps17–210ps17.
- Uguz, I., Ganji, M., Hama, A., Tanaka, A., Inal, S., Youssef, A., Owens, R. M., Quilichini, P. P., Ghestem, A., Bernard, C., et al., 2016. Autoclave sterilization of pedot: Pss electrophysiology devices. *Advanced healthcare materials* 5 (24), 3094–3098.
- Vansteensel, M. J., Pels, E. G., Bleichner, M. G., Branco, M. P., Denison, T., Freudenburg, Z. V., Gosselaar, P., Leinders, S., Ottens, T. H., Van Den Boom, M. A., et al., 2016. Fully implanted brain–computer interface in a locked-in patient with als. *New England Journal of Medicine* 375 (21), 2060–2066.
- Vetter, R. J., Williams, J. C., Hetke, J. F., Nunamaker, E. A., Kipke, D. R., 2004. Chronic neural recording using silicon-substrate microelectrode arrays implanted in cerebral cortex. *IEEE transactions on biomedical engineering* 51 (6), 896–904.
- von Ellenrieder, N., Beltrachini, L., Muravchik, C. H., 2012. Electrode and brain modeling in stereo-eeg. *Clinical Neurophysiology* 123 (9), 1745–1754.
- Vorwerk, J., Cho, J.-H., Rampp, S., Hamer, H., Knösche, T. R., Wolters, C. H., 2014. A guideline for head volume conductor modeling in eeg and meg. *NeuroImage* 100, 590–607.
- Wang, W., Collinger, J. L., Degenhart, A. D., Tyler-Kabara, E. C., Schwartz, A. B., Moran, D. W., Weber, D. J., Wodlinger, B., Vinjamuri, R. K., Ashmore, R. C., et al., 2013. An electrocorticographic brain interface in an individual with tetraplegia. *PloS one* 8 (2), e55344.
- Wang, X., Gkogkidis, C. A., Iljina, O., Fiederer, L. D., Henle, C., Mader, I., Kaminsky, J., Stieglitz, T., Gierthmuehlen, M., Ball, T., 2017. Mapping the fine structure of cortical activity with different micro-ecog electrode array geometries. *Journal of Neural Engineering* 14 (5), 056004.
- Whitmore, N. W., Lin, S.-C., 2016. Unmasking local activity within local field potentials

- (lfps) by removing distal electrical signals using independent component analysis. *Neuroimage* 132, 79–92.
- Wyler, A. R., Richey, E., Atkinson, R. A., Hermann, B. P., 1987. Methohexital activation of epileptogenic foci during acute electrocorticography. *Epilepsia* 28 (5), 490–494.
- Xing, D., Yeh, C.-I., Shapley, R. M., 2009. Spatial spread of the local field potential and its laminar variation in visual cortex. *Journal of neuroscience* 29 (37), 11540–11549.
- Zaveri, H. P., Duckrow, R. B., Spencer, S. S., 2000. The effect of a scalp reference signal on coherence measurements of intracranial electroencephalograms. *Clinical Neurophysiology* 111 (7), 1293–1299.
- Zhang, Y., Ding, L., van Drongelen, W., Hecox, K., Frim, D. M., He, B., 2006. A cortical potential imaging study from simultaneous extra-and intracranial electrical recordings by means of the finite element method. *NeuroImage* 31 (4), 1513–1524.